The Dissertation Committee for Sarah Faye Swingle Certifies that this is the approved version of the following dissertation:

Main Group Semiconducting Materials: Boron Arsenide and an Ester-Functionalized Salophen Aluminum Polymer

Committee:

Alan H. Cowley, Supervisor

Bradley J. Holliday, Co-Supervisor

Allen J. Bard

Simon M. Humphrey

Richard A. Jones

Sheldon Landsberger

Main Group Semiconducting Materials: Boron Arsenide and an Ester-Functionalized Salophen Aluminum Polymer

by

Sarah Faye Swingle, B.S.

Dissertation

Presented to the Faculty of the Graduate School of

The University of Texas at Austin

in Partial Fulfillment

of the Requirements

for the Degree of

Doctor of Philosophy

The University of Texas at Austin

May 2013

Dedication

To my family-

For always believing in me.

I would not be where I am now without your constant encouragement and love.

To Rob-

For celebrating the good times and supporting me through the tough times.

I'm so looking forward to every part of our future.

Acknowledgements

It has been a privilege to work with Professor Alan Cowley throughout my graduate studies. His passion for chemistry is inspirational and contagious. If I can love what I do a fraction of the amount he loves his job, I'll be a happy chemist. He's forever an optimist and his wisdom and positivity can rejuvenate my spirits when I'm at my lowest with chemistry.

I'd also like to thank Professor Bradley Holliday for providing extra guidance at the end of my grad school career. He's taught me a lot of chemistry in a short amount of time. Most importantly, his mentorship through the job-searching and graduating process has been invaluable to me and has shaped my future in a big way.

It was an honor to collaborate with Professor Allen Bard and his lab, who have expanded my knowledge in a field of chemistry different from my own. I'd especially like to thank Shijun for his patience and friendship. And to the rest of my committee, Professors Richard Jones, Simon Humphrey, and Sheldon Landsberger, thank you for your advice, suggestions, and time.

Research aside, I'd like to thank Professor Alan Campion for setting an example for me of an outstanding teacher. The skills and philosophy I've learned from him are valuable to me both in a classroom environment and anywhere else I might find myself in a teaching role.

To the Cowley group, past and present- it's a good thing I like you, because we spend A LOT of time together. I know that you're always good for some chemistry suggestions and for some laughs. I couldn't tell you which is more important to me. You are the most determined, intelligent, and supportive group of individuals I know.

To the Holliday group- I've really enjoyed getting to know you and working in your lab recently. Thank you for being so generous with your time and instruments. I'd especially like to thank Lauren Lytwak for her friendship from start to finish. No denying there's been some ups and downs, but the ups were really fun and the downs were easier knowing someone was going through it with me. And I think everything's turned out pretty nicely.

So many people have played a part in my grad school experience. Dr. Vincent Lynch and Dr. Hugo Celio along with the NMR and Mass Spec facilities have really shed light on my research. And Michael Ronalter has made me a thousand quartz tubes. Without their expert knowledge and patience, my progress would not be possible.

Lastly, I want to thank my family, my best friends, and Rob. I've cut holidays short and I've let too much time go between visits. Late nights and stress have made me unavailable at times. But you always understand and never stop encouraging me. You're what's consistent in my life. I don't know how I got so lucky.

Main Group Semiconducting Materials: Boron Arsenide and an Ester-Functionalized Salophen Aluminum Polymer

Sarah Faye Swingle, Ph. D.

The University of Texas at Austin, 2013

Supervisors: Alan H. Cowley and Bradley J. Holliday

Boron arsenide is a compound main group semiconductor with a theoretical band gap in the range of 1.1 to 1.6 eV. Despite this ideal band gap, experimental studies of boron arsenide are very limited. In the present work, single source precursors with covalent bonds between boron and arsenic and labile ligands have been designed and synthesized. These precursors underwent thermal or chemical treatment to produce boron arsenide materials. Boron arsenide has also been prepared as a thin layer deposited on a boron substrate and a p-type photoelectrode was prepared from this material. The structure of the product was identified on the basis of X-ray diffraction and scanning electron microscopy, and the surface composition was determined by means of X-ray photoelectron spectroscopy. The electrode was found to be photoactive under both visible and UV-visible light irradiation and displayed a photocurrent of approximately 0.1 mA/cm^2 under UV-visible light irradiation at an applied potential of -0.25 V *vs*. Ag/AgCl. The valence band was estimated to be -5.1 eV. The indirect band gap, as determined from incident photo-to-electron conversion efficiency plots, is 1.46 eV.

An ester-fuctionalized salophen aluminum complex that features a polymerizable bithiophene as the ester R group has been designed and synthesized. Metallopolymers of this type offer the additional advantages of processability and uniformity of the resulting

films. The new salophen complex exhibited emission in the blue region at 491 nm with a quantum yield of 8.19%, which is significantly larger than that of the isolated ligand. Electropolymerization of this complex on a platinum button electrode resulted in the formation of an electrically conductive polymer that is also ionically conductive at low scan rates. In the polymeric form, the emission wavelength was found to be red-shifted to 505 nm.

Table of Contents

List of Tables

List of Figures

List of Schemes

BORON ARSENIDE, A NEGLECTED SEMICONDUCTOR

Although silicon dominates the microelectronics industry, compound main group semiconductors possess several electronic properties that are superior to those of silicon.[1] For example, in the case of gallium arsenide, the most common of the compound main group semiconductors, the charge carriers can attain a higher saturated electron velocity and have a higher electron mobility than the charge carriers in silicon. Moreover, devices made from gallium arsenide have higher breakdown voltages than devices made of silicon, thus allowing gallium arsenide devices to be operated at higher potentials. These properties make compound main group semiconductors suitable for a wide variety of novel applications, such as microwave integrated circuits, light-emitting diodes, and laser diodes. Among the compound main group semiconductors is the Group III-V family, to which both gallium arsenide and boron arsenide belong. Materials in this family are made of an element from Group III and an element from Group V and are isoelectronic with the elements from Group IV, such as silicon and germanium. Boron arsenide is of particular interest in this context because it is similar to silicon electronically.[2] Like silicon, boron arsenide features a *p*-like conduction band minimum and an indirect band gap. The electrons are shared almost equally between the boron and arsenic atoms, thus causing boron arsenide to be covalent like silicon. This feature also distinguishes it from the other members of the Group III-V family of compound semiconductors, which are more ionic in nature.[3] Normally, the Group III element would act as the cation in a III-V semiconductor. However, using the Phillips[4] and Van Vechten and Phillips[5] scales of ionicities, the electron density in boron arsenide actually favors boron slightly. Moreover, theoretical studies suggest that the roles of the cation and anion may be reversed in boron arsenide and that consequently boron may serve as the anion in this

nearly perfectly covalent compound.[6,7] This unique behavior is due to the absence of *p* electrons and the small size of the boron atom. Theoretical values for the indirect band gap span the approximate range of 1.1 to 1.6 eV[3,7,8] and average about 1.3 eV, which corresponds to the high energy end of the infrared region of the electromagnetic spectrum. With a theoretical band gap of roughly 1.3 eV, boron arsenide should be responsive to both visible and UV radiation. Since this is where the majority of solar energy is found, boron arsenide has good prospects for photovoltaic and photoelectrochemical applications. A further interesting feature is that boron arsenide and gallium arsenide theoretically represent an ideal alloying system.[2] The offset of the valence bands for these two materials is favorable for charge carrier flow. Furthermore, the bulk mixing enthalpy is low, meaning that a wide range of compositions is possible, which should be ideal for band gap tuning. However, despite the favorable properties of boron arsenide cited above, this material has long been neglected in the study of compound main group semiconductors and only a few experimental studies have been published.[3]

Chapter 1: Single Source Precursors and Other Synthetic Approaches to Boron Arsenide

As will be discussed in detail in Chapter 2, the synthesis of boron arsenide (BAs) was eventually achieved by the thermal reaction of the elements. However, prior to this, various other synthetic approaches had been taken, with a particular focus on the single source precursor approach, which has been used widely for the preparation of Group III-V materials. Accordingly, it is appropriate to provide some pertinent background on this method.

THE SINGLE SOURCE PRECURSOR METHOD

Compound main group semiconductors such as gallium arsenide, aluminum gallium arsenide, gallium nitride, indium phosphide, zinc selenide, cadmium telluride, and copper indium gallium selenide are useful in many applications. Examples include satellite TV receivers, optical fiber communications, compact disc players, barcode readers, full color advertising displays, and solar cells.[1] Most commonly they are used as thin films. However solids and nanoparticles are also important. One way to access these materials is by means of dual source methods. The conventional dual sources for the Group III-V family of semiconductors are Group III alkyls and Group V hydrides, such as phosphine and arsine. An example of a dual source reaction that results in the production of gallium arsenide (GaAs) is shown below.

$$GaMe_3 + AsH_3 \rightarrow GaAs + 3\ CH_4$$

The use of phosphine and arsine precursors results in films with very low levels of carbon contamination. This is most likely due to the fact that the carbon-containing fragments are cleanly removed by the large amount of atomic hydrogen that is released from the Group V hydride during pyrolysis.[9] From the standpoint of purity, there seems to be little

reason to look beyond dual sources of this type. However, due to concerns about safety, there is major motivation to seek alternative synthetic routes to the desired products. For example, the Group III alkyls are often pyrophoric. Moreover, the Group V hydrides are extremely toxic and typically stored in high-pressure cylinders. Furthermore, they are also highly reactive, thus making them difficult to handle and purify. Even when purified, these hydrides sometimes react with their storage containers, thereby reintroducing contaminants.[10] A further issue is that stoichiometries of the products are sometimes difficult to control, thus requiring fine-tuning of gas flow and temperature during the reaction. More recently, alternative liquid Group V sources have been developed, which are safer than Group V hydride gases in the event of accidental gas release.[11] The use of trialkylarsines is generally unsuccessful in terms of film formation and typically results in films that feature high carbon contamination. This outcome is due to the lack of active AsH species that are necessary for carbon removal from the surface of the film during film growth. The arsines that involve one or more hydrogens, such as the alkylarsines Et_2AsH, $EtAsH_2$, and $^tBuAsH_2$ are superior sources of arsenic. Furthermore, $^tBuAsH_2$ undergoes pyrolysis at a lower temperature than arsine, thus permitting film growth at lower V/III ratios.[9]

Generally speaking, Group III-V Lewis acid-base adducts such as $Me_3In{\bullet}PEt_3$ and $Me_3In{\bullet}NMe_3$ are easier to handle and purify because they are less air-sensitive than their individual components.[10] However, the adduct bond is often weaker than the bonding in the individual ligands. On the other hand, the adduct bond strength can be fine tuned by varying the electron donating nature of the alkyl ligands or by substitution by a halogen or psuedohalogen group. Overall, a clean decomposition is not easily achieved and it is often necessary to employ an excess of phosphine or arsine to produce a satisfactory film.

Overall, single source precursors, which are small organometallic complexes designed with a desired material in mind, offer a safer, more controllable alternative to dual source methods in terms of producing satisfactory semiconducting materials. Such precursors contain the elements of the desired material, usually bonded covalently, along with a set of ligands that are labile. The presence of robust two-electron sigma bonds between the elements of the desired material promotes stoichiometric control and enables the labile ligands to undergo facile elimination, either thermally or chemically. Clean ligand elimination from a single source precursor results in the production of the desired semiconducting material, as illustrated in Figure 1.1. A further advantage is that single source precursors are less toxic than many of the individual components and offer increased stability toward air and moisture. Furthermore, the strong bonding between the elements of the desired material in the precursor permits facile stoichiometric control and results in few defects in the desired material. Single source precursors offer a safer, more elegant way to produce a semiconductor material.

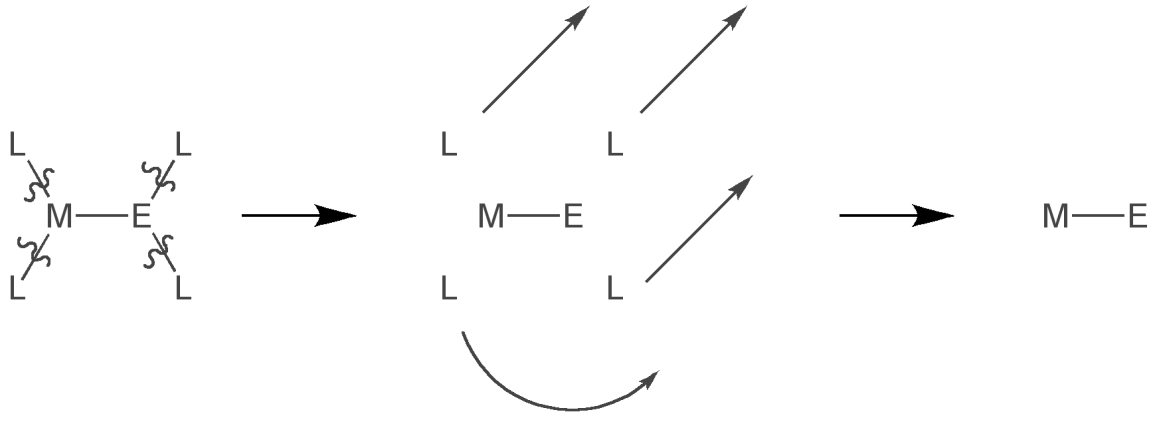

Figure 1.1: Ligand elimination from a single source precursor. M represents a Group III element, E represents a Group V element, and L represents a ligand.

The need for new precursors increases as electronic devices become increasingly complex.[1] As pointed out earlier, a satisfactory precursor should be stable and capable of undergoing a controllable decomposition. Furthermore, for industrial use the precursor should be readily synthesized on a large scale. Another requirement for chemical vapor deposition (CVD) is that the precursor should be volatile at a temperature substantially below the decomposition temperature. However, this requirement has become less stringent with the advent of techniques such as aerosol assisted CVD and liquid injection CVD. In the CVD method, the precursor is heated until volatile and subsequently transferred via a carrier gas to the substrates that are held at high temperatures. Under these conditions, the precursors undergo clean decomposition on the substrate. The use of aerosol assisted CVD and liquid injection CVD obviates the volatility requirement since the precursor is not transferred to the substrate in the gas phase. Moreover, volatility is not a prerequisite for the formation of nanoparticulate materials, since these can be prepared simply by thermolysis of the precursor in a high-boiling solvent. Overriding the above qualities is the purity of the precursor. A high purity precursor prevents contamination and other undesirable side reactions and is therefore the most important requirement affecting the properties and composition of the resulting material.

β-Hydride Elimination Precursors

In 1985 Cowley and Jones, et al. began work on a single source precursor approach to many III-V materials with a particular emphasis on GaAs.[12] This work was focused on compounds with sigma bonds between gallium and arsenic because of the relative strength of sigma bonds in comparison with those of other well-known adduct complexes. Most of these precursors featured the 1:1 stoichiometry of the desired material. However, a compound with a 1:3 Ga:As ratio was also synthesized and later

proved to be a very good precursor. Typically, hydrocarbon substituents that feature β-hydrogens are capable of facile elimination at relatively modest temperatures. The compounds featuring ethyl, *iso*-propyl, *n*-butyl, or *tert*-butyl groups were found to be the most useful.[12,13] Ligand loss by β-hydride elimination produces an olefin and a metal hydride.[14] The hydride then undergoes intramolecular coupling with another alkyl ligand on the metal center thereby producing a saturated hydrocarbon. Precursors of this design have the twofold advantage of being sufficiently volatile and hydrocarbon soluble. A further advantage of such compounds is that they are relatively nontoxic.[15] Secondary phosphines and arsines were found to be particularly useful since they undergo facile alkane elimination reactions with trialkylgallium and trialkylindium to afford compounds of the type $(R_2MER'_2)_n$ (M = Ga, In; E = P, As).[16,17] The foregoing method was used for the preparation of $[Me_2Ga(\mu\text{-}As^iPr_2)]_3$[18] and $[^tBu_2Ga(\mu\text{-}AsH_2)]_3$[19]. However, alkane elimination routes become less efficient as alkyl groups become increasingly bulky, hence a salt elimination method was employed for the syntheses of $[Me_2Ga(\mu\text{-}As^tBu_2)]_2$, $[^nBu_2Ga(\mu\text{-}As^tBu_2)]_2$, and $Ga(As^tBu_2)_3$.[20] On the other hand, $[Et_2Ga(\mu\text{-}As^tBu_2)]_2$ was synthesized via the comproportionation reaction of $Ga(As^tBu_2)_3$ with triethylgallium.[13] A summary of the foregoing reactions is presented in Scheme 1.1.

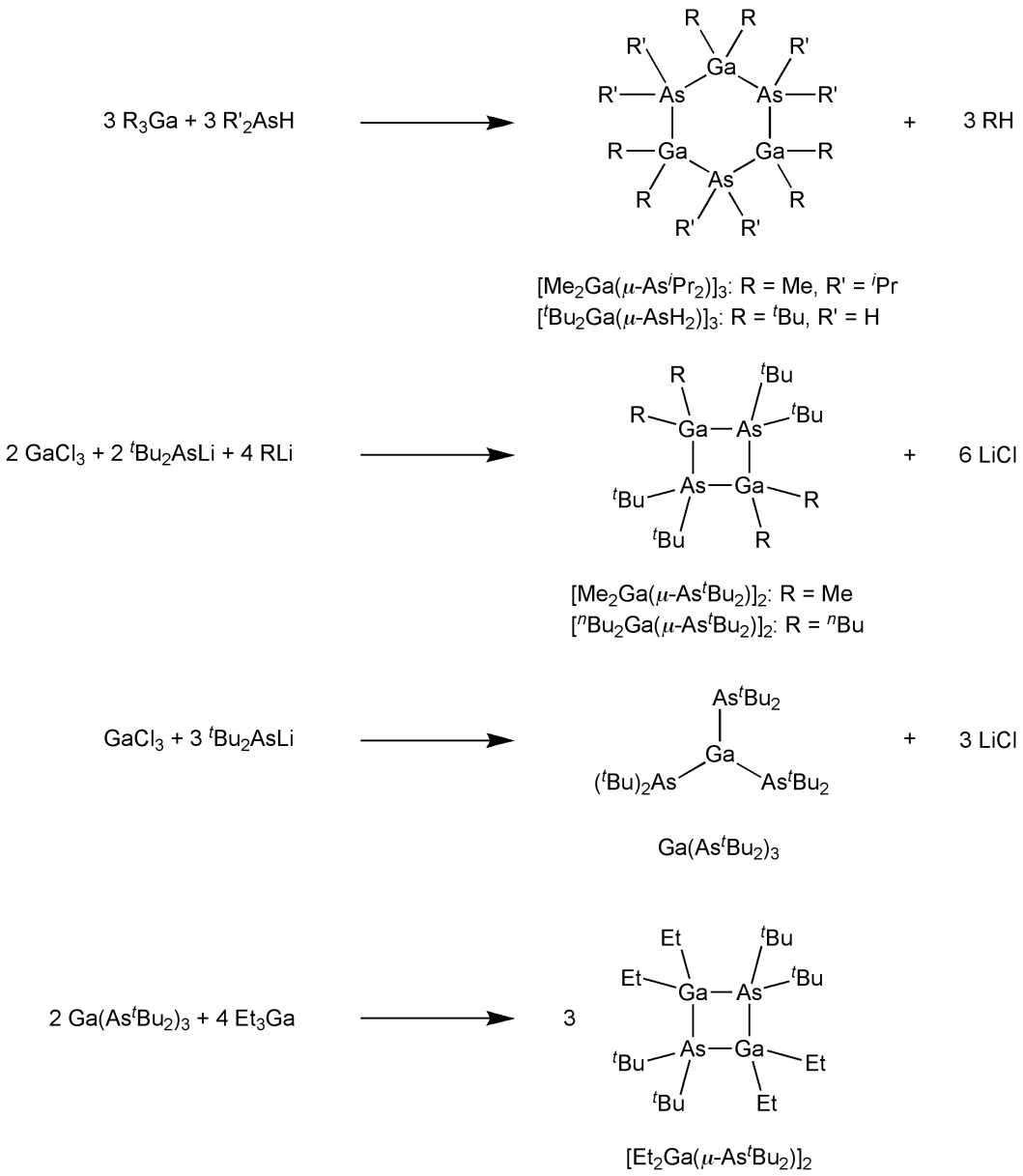

Scheme 1.1: Synthesis of GaAs single source precursors for β-hydride elimination. $[Me_2Ga(\mu\text{-}As^iPr_2)]_3$ was prepared neat at 130 °C while $[^tBu_2Ga(\mu\text{-}AsH_2)]_3$ was prepared neat or in benzene at a temperature of -196 °C followed by slow warming to room temperature. The compounds $[Me_2Ga(\mu\text{-}As^tBu_2)]_2$, $[^nBu_2Ga(\mu\text{-}As^tBu_2)]_2$, and $Ga(As^tBu_2)_3$ were prepared in toluene or THF solution at -78 °C and $[Et_2Ga(\mu\text{-}As^tBu_2)]_2$ was prepared in toluene solution at room temperature.

The use of trimeric complexes such as $[Me_2Ga(\mu\text{-}As^iPr_2)]_3$ resulted in the formation of nonstoichiometric species due to the preferential elimination of tetraalkyldiarsine and trialkylarsine.[14] Monitoring of the pyrolysis process by mass spectrometry revealed that the trialkylarsine signal increased with time while that of the tetraalkyldiarsine signal decreased, which suggests that the tetraalkyldiarsine may serve as a precursor to the trialkylarsine. It was also noted that slow tetraalkyldiarsine elimination occurred from $[Me_2Ga(\mu\text{-}As^iPr_2)]_3$ during sample storage of this compound at room temperature. This is perhaps not surprising since diarsines are known to be quite stable molecules.[21] The question as to whether a precursor will eliminate diarsines may be related to the stability of the residual product rather than to the diarsine itself. For example, in the case of $[Me_2Ga(\mu\text{-}As^iPr_2)]_3$, tetrakis-*iso*-propyldiarsine elimination may result in the formation of $(Me_2Ga)_3As$. The latter compound was not detected. However, it is similar to the known compound $[(thf)Br_2Ga]_3As$,[22] which suggests it may possess the necessary stability to facilitate diarsine elimination.

Precursors containing hydrogen, such as $[^tBu_2Ga(\mu\text{-}AsH_2)]_3$, were expected to decompose cleanly at temperatures lower than those featuring alkyl groups.[19] In the solid state, $[^tBu_2Ga(\mu\text{-}AsH_2)]_3$ decomposed slowly at 155 °C and more rapidly at 250 °C to produce amorphous GaAs accompanied by significant carbon contamination. Repetition of this reaction in a refluxing toluene solution resulted in the formation of amorphous GaAs along with trace quantities of impurities within 20 minutes. Annealing the reaction mixture at 350-400 °C under a nitrogen atmosphere resulted in the formation of small particles of polycrystalline GaAs.

Organometallic CVD studies of the deposition of GaAs from $[Me_2Ga(\mu\text{-}As^tBu_2)]_2$ have been reported using a reactor pressure of 1×10^{-4} Torr and a temperature of 525 °C.[23] The resulting films were grown on GaAs and $\alpha\text{-}Al_2O_3$ and were found to be free of

any carbon incorporated from the precursor. Photoluminescence spectra of these films recorded at 5 K revealed that the band gap of this material is 1.52 eV, which falls within the range anticipated for GaAs. However, it should be noted that these films were degeneratively doped. In the case of $[Me_2Ga(\mu\text{-}As^tBu_2)]_2$, the proposed deposition mechanism begins with the interaction of a gallium atom with a β-hydrogen of the *tert*-butyl group, thereby cleaving the bond between arsenic and the *tert*-butyl and eliminating isobutene. Subsequently methane elimination from the gallium atom took place as is shown in Scheme 1.2.[15] Support for this mechanism is provided by the online mass spectrometric detection of isobutene and methane as the major hydrocarbons produced during this deposition. Additional support was provided by the X-ray structure.[20] The hydrogen atoms were not located in this crystal structure. However, when they were placed in idealized positions, a close interaction between gallium and a hydrogen of the *tert*-butyl group was evident as illustrated in Scheme 1.2. Furthermore, isobutane was detected by mass spectrometric analysis thus implying the formation of *tert*-butyl radicals along with hydrogen abstraction in an additional, minor pathway.

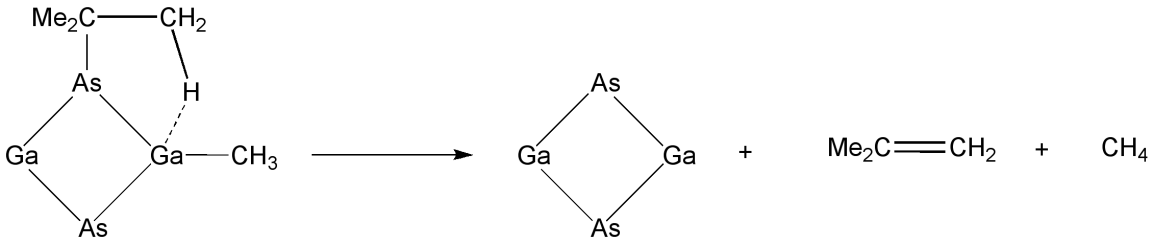

Scheme 1.2: Proposed mechanism for β-hydride elimination from $[Me_2Ga(\mu\text{-}As^tBu_2)]_2$.

The thermal decomposition of $[^nBu_2Ga(\mu\text{-}As^tBu_2)]_2$ at 350 °C resulted in the formation of polycrystalline GaAs along with a virtually quantitative hydrocarbon elimination thus suggesting that the thermal decomposition of $[^nBu_2Ga(\mu\text{-}As^tBu_2)]_2$ is

more facile than that of $[Me_2Ga(\mu\text{-}As^tBu_2)]_2$.[23] A mass spectrometric assay of the eliminated hydrocarbons revealed that they consisted primarily of *n*-butene and *iso*-butane along with trace amounts of *n*-butane and *iso*-butene. Given the foregoing results, it is likely that two competitive mechanisms are operative, the secondary one being analogous to the mechanism proposed in Scheme 1.2. Thus, the primary mechanism begins with β-hydrogen transfer from an *n*-butyl group to the gallium center, which results in the elimination of *n*-butene and this step is followed by the elimination of *iso*-butane from a *tert*-butyl group, as illustrated in Scheme 1.3.

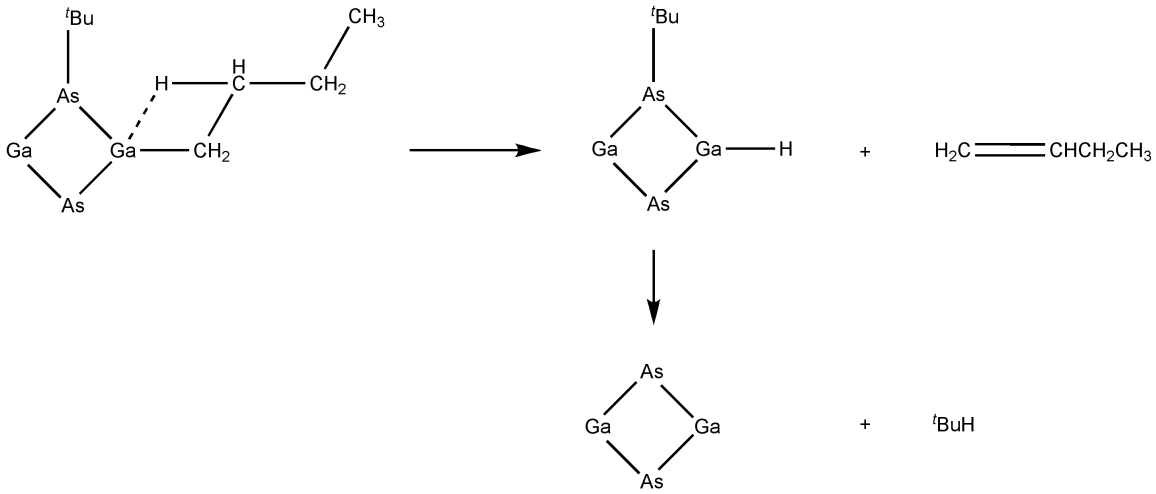

Scheme 1.3: Proposed mechanism for β-hydride elimination from $[^nBu_2Ga(\mu\text{-}As^tBu_2)]_2$.

Precursors $[Me_2Ga(\mu\text{-}As^iPr_2)]_3$, $[Me_2Ga(\mu\text{-}As^tBu_2)]_2$, $Ga(As^tBu_2)_3$, and $[Et_2Ga(\mu\text{-}As^tBu_2)]_2$ were subjected to extensive film growth studies using a chemical beam epitaxy reactor. This method has been shown to be suitable for less volatile precursors.[12] As mentioned previously, treatment of $[Me_2Ga(\mu\text{-}As^iPr_2)]_3$ in this fashion resulted in the formation of unsatisfactory thin films that were deficient in arsenic due to the preferential elimination of tetraalkyldiarsine and trialkylarsine. On the other hand, the thermal

treatment of compounds $[Me_2Ga(\mu\text{-}As^tBu_2)]_2$ and $[Et_2Ga(\mu\text{-}As^tBu_2)]_2$ resulted in the formation of epitaxial p-type films at temperatures greater than 500 °C and pressures of 10^{-5} Torr. Interestingly, both films had very similar carbon levels (10^{18}-10^{19} cm^{-3}) despite the previously observed trend that carbon contamination is lower when trimethylgallium is replaced by triethylgallium. The films that had been grown from $[Me_2Ga(\mu\text{-}As^tBu_2)]_2$ exhibited Hall mobilities of 54-94 $cm^2V^{-1}s^{-1}$. However, the films that had been grown from $[Et_2Ga(\mu\text{-}As^tBu_2)]_2$ had unusually low Hall mobilities, thus suggesting the existence of deep level defects. The corresponding pyrolysis studies indicated that the *tert*-butyl groups of both $[Me_2Ga(\mu\text{-}As^tBu_2)]_2$ and $[Et_2Ga(\mu\text{-}As^tBu_2)]_2$ begin to react at 330 °C. Methyl groups from $[Me_2Ga(\mu\text{-}As^tBu_2)]_2$ begin to react at 445 °C, whereas ethyl groups from $[Et_2Ga(\mu\text{-}As^tBu_2)]_2$ begin to react at 350 °C. It is necessary that ligand elimination occur from arsenic before it occurs at gallium to avoid gallium deposition on the surface of the film.[14] An excess of arsenic does not remain on the surface due to its relative volatility. In the case of $[Me_2Ga(\mu\text{-}As^tBu_2)]_2$, β-hydride elimination occurs at arsenic, followed by coupling of methyls and hydrides at gallium. Interestingly, temperature programmed desorption studies indicated that the methyl groups desorb from gallium in preference to reacting with the surface hydrides.[24] In the case of $[Et_2Ga(\mu\text{-}As^tBu_2)]_2$, the ethyl groups are eliminated from gallium at virtually the same temperature as that required for the elimination of *tert*-butyl groups from arsenic. As a consequence, the free gallium preferentially reacts with itself rather than reacting with arsenic, leading to formation of gallium islands in the film, causing the low Hall mobility. Detection of both ethane and ethene during deposition suggests that both β-hydride elimination and homolysis of ethyl groups occurs at the gallium center. Epitaxial films were produced from $Ga(As^tBu_2)_3$ at 480 °C and 10^{-5} Torr with a carbon contamination level of 4 x 10^{16} cm^{-3}. This carbon contamination level is significantly lower than the carbon

contamination levels of films produced from the 1:1 precursors, most likely due to the absence of carbon on gallium. These films were found to be n-type, which was anticipated on the basis of the excess of arsenic in the precursor. The Hall mobility was 300 $cm^2V^{-1}s^{-1}$.[24] The photoluminescense spectrum at 4.2 K displayed a peak at 819 nm, which is equivalent to 1.51 eV. No areas of nonstoichiometric gallium or arsenic were evident when the films were examined by energy-dispersive spectroscopy.[25]

Groshens and coworkers have explored the synthesis[26] and pyrolysis[27] of boron and phosphorus containing precursors that are capable of undergoing β-hydride elimination. For example, the reaction of Et_2BCl with $^tBu_2PLi$ in benzene solution resulted in the production of $Et_2BP^tBu_2$ in 20 minutes. A similar procedure was employed for the synthesis of $(Me_2BP^tBu_2)_2$ from Me_2BBr and $^tBu_2PLi$. The pyrolysis of $Et_2BP^tBu_2$ at 0.01-0.1 Torr and temperatures of 550 °C and 850 °C resulted in the formation of films that were deficient in phosphorus. High carbon contamination was evident in the Auger analysis. Moreover, hydrogen, ethene and isobutene were detected by mass spectrometry and proton NMR. It is likely that these products were formed via β-hydride elimination and homolytic bond fission. The pyrolysis of $(Me_2BP^tBu_2)_2$ at the same pressure and 650 °C also resulted in the formation of films that were deficient in phosphorus and high in carbon contamination. Both hydrogen and isobutene elimination were detected. The foregoing results indicate that under the conditions employed the preferential loss of phosphorus prevents the deposition of usable boron phosphide films from the precursors $Et_2BP^tBu_2$ and $(Me_2BP^tBu_2)_2$.

Dehalosilylation Precursors

Starting in 1986,[28] it was recognized that dehalosilylation represents an alternative synthetic route to the desired III-V products. Ligands of these precursors can easily

couple due to the strength of silicon-halogen bonds. Often, the use of the dehalosilylation route results in the production of nanocrystalline materials.

The preparation of GaAs and indium arsenide via the reaction of MX_3 (M = Ga, X = Cl, Br; M = In, X = Cl) with $As(SiMe_3)_3$ occurred at relatively low temperatures due to the facile elimination of $XSiMe_3$.[29]

$$MX_3 + As(SiMe_3)_3 \rightarrow MAs + 3\ XSiMe_3$$

$$M = Ga, X = Cl, Br; M = In, X = Cl$$

The reactants were allowed to mix in hydrocarbon solvents at room temperature, at which point a precipitate began to form. The reaction mixture was then stirred with little or no heating and after a few days, the solvent and other volatiles were removed under reduced pressure. In the cases of $GaCl_3$ and $InCl_3$, a higher-boiling hydrocarbon solvent was added and the reaction mixture was further heated, followed by the removal of solvent and volatiles under vacuum. The residual solid was then heated under vacuum, ramping the temperature with time. The elimination of $XSiMe_3$ was quantitative and the completion of the reaction was recognized by elimination of three equivalents of the silyl halide. The resulting black solids were then characterized by powder X-ray diffraction (XRD) and elemental analysis. GaAs and indium arsenide were produced in 88-96% and 98% purity, respectively. The impurities included carbon, hydrogen, silicon, and halides. Details of the reaction conditions and product analyses are displayed in Table 1.1.

Table 1.1: Reaction conditions and product analyses for the production of GaAs and indium arsenide via the dehalosilylation reaction, $MX_3 + As(SiMe_3)_3$.

$MX_3 + As(SiMe_3)_3 \rightarrow MAs + 3\ XSiMe_3$					
MX_3	Treatment	Precipitate	M:As mole ratio[a]	Purity[a] (%)	Impurities[a] (weight %)
$GaCl_3$	Pentane, RT, o/n Toluene, 90 °C, o/n Neat, 140-160 °C, o/n Neat, 160-180 °C, 3 h Neat, 400-500 °C, 2 h	Light brown to black	1.00:1.01	96	C: 1.68 H: 0.30 Cl: 2.51 Si: 0.51
$GaBr_3$	Benzene, 47 °C, o/n Benzene, 75-85 °C, o/n Neat, 410 °C	Red-brown to black		88	C: 3.58 H: 0.19 Br: 7.21 Si: <0.7
$InCl_3$	Pentane, RT, 3 days Benzene, 70-75 °C, 4 days Neat, 150 °C, o/n Neat, 400-500 °C, 15 min	Salmon to dark brown to black	1.00:0.99	98	C: 0.56 H: 0.17 Cl: 0.80 Si: <0.1

[a]based on elemental analysis. RT = room temperature. o/n = overnight.

The size of the resulting material proved to be dependent on the solvent.[30] Alivisatos et al. repeated Wells's preparation of GaAs from $GaCl_3$ and $As(SiMe_3)_3$ and found the material to have a domain size of 100 Å. The same reaction was then carried out in refluxing quinoline for 3 days. The resulting red powder was identified as GaAs by XRD. The domain size was 24 Å. Prior to annealing, this powder was soluble in quinoline and pyridine. Annealing the product under vacuum at 450 °C improved the crystallinity, but also decreased the solubility. Carbon and nitrogen impurities were detected in the product and the Ga:As mole ratio was found to be 5:4.

Sonication of GaX_3 (X = Cl, Br, I) with $P(SiMe_3)_3$ in pentane or a pentane/toluene mixture for 14-16 h resulted in the formation of $[X_2GaP(SiMe_3)_2]_2$, from which X-ray quality crystals were grown for X = Cl, Br from a toluene solution.[31,32] It is interesting to note that, in the analogous reactions of the gallium-arsenic system, no stable intermediate precursors could be isolated on the reaction pathway to GaAs. However, in the case of

the indium-phosphorus system reported by Barron et al., an intermediate precursor with the proposed structure $[Cl_2InP(SiMe_3)_2]_x$ can be isolated prior to undergoing thermal decomposition and formation of indium phosphide.[33] Heating $[X_2GaP(SiMe_3)_2]_2$ to 300-320 °C in a water-cooled sublimator under vacuum overnight resulted in dehalosilylation and formation of dark brown powders. In the cases of X = Br, I, the powders were annealed at 400-500 °C for 1 h. Elemental analysis revealed the presence of gallium phosphide along with relatively high levels of impurities, as shown in Table 1.2.

$$GaX_3 + P(SiMe_3)_3 \rightarrow \tfrac{1}{2}\,[X_2GaP(SiMe_3)_2]_2 + XSiMe_3$$

$$[X_2GaP(SiMe_3)_2]_2 \rightarrow 2\,GaP + 4\,XSiMe_3$$

$$X = Cl, Br, I$$

The peaks of the XRD patterns were found to be broad, which is indicative of the presence of nanocrystalline particles. Using the Debye-Scherrer formula[34] to relate the broadness of the peaks to the average domain size revealed that the values were 3 nm for X = Br, I and 1 nm for X = Cl. The difference in domain size between the bromide, iodide and chloride implies that annealing has an influence on domain size. Thermal gravimetric analyses (TGA) of $[X_2GaP(SiMe_3)_2]_2$ under a nitrogen stream indicated that the thermal stability of the precursor increases with the size of X. Approximately two molar equivalents of $XSiMe_3$ were eliminated by 250 °C for X = Cl. In the case of X = Br, complete $XSiMe_3$ elimination occurred by 350 °C. The thermogram for X = I was not well resolved and the elimination of only one molar equivalent of $XSiMe_3$ was detected at 195 °C.

The sonication of two equivalents of $GaCl_3$ and $P(SiMe_3)_3$ in pentane solution for 15 h resulted in a compound of composition PCl_3Ga_2.[32] On the other hand, when $GaBr_3$ or GaI_3 were used instead of $GaCl_3$, only unstable oils were produced. The thermolysis of PCl_3Ga_2 at 300 °C for 2 h and 440 °C for 2 h under vacuum in a water-cooled sublimator

resulted in the elimination of $GaCl_3$ and the formation of gallium phosphide with a domain size of 3 nm. The sample of gallium phosphide had high levels of impurities along with an excess of phosphorus. The analogous arsenic reaction in a stirred pentane solution at room temperature for 16 days resulted in the formation of a precursor with the empirical formula $AsCl_3Ga_2$.[35] Heating this precursor to 380-410 °C under static vacuum in a water-cooled sublimator for 22 h resulted in the elimination of $GaCl_3$ and the production of GaAs as a black solid in 93% purity. Product analyses for the thermal decompositions of both PCl_3Ga_2 and $AsCl_3Ga_2$ are presented in Table 1.2.

$$2\ GaCl_3 + E(SiMe_3)_3 \rightarrow ECl_3Ga_2 + 3\ ClSiMe_3$$

$$ECl_3Ga_2 \rightarrow GaE + GaCl_3$$

$$E = P, As$$

Two equivalents of $InCl_3$ and $As(SiMe_3)_3$ were added together in a toluene/THF solution and stirred for 72 h at room temperature.[36] The volatiles and solvents were removed under vacuum, resulting in a red-brown powder with an elemental composition that was significantly different from that expected for $AsCl_3In_2$. However, after annealing for 4 h at 350 °C in a sublimator under vacuum, a black powder was produced and identified by XRD as indium arsenide with a domain size of 16 nm. The purity of this product was 87.9% and the mole ratio was found to be 1.00:1.00 on the basis of elemental analysis.

Table 1.2: Product analyses for production of gallium phosphide from the dehalosilylation of $[X_2GaP(SiMe_3)_2]_2$ and for the production of gallium phosphide and GaAs via the thermal decomposition of ECl_3Ga_2.

$[X_2GaP(SiMe_3)_2]_2 \rightarrow 2\ GaP + 4\ XSiMe_3$				$ECl_3Ga_2 \rightarrow GaE + GaCl_3$			
X	Ga:P mole ratio[a]	Purity[a] (%)	Impurities[a] (weight %)	E	Ga:E mole ratio[a]	Purity[a] (%)	Impurities[a] (weight %)
Cl	1.03:1.00	84.8	C: 7.24 H: 1.22 Cl: 6.88	P	1.00:1.12*		Cl: 1.78*
Br	1.00:1.18		C: 3.23 H: 0.37	As	1.01:1.00	93	C: 5.17 H: 0.35
I	1.00:1.27		C: 2.71 H: 0.30 I: 7.65				Cl: 2.41 Si: ≤0.22

[a]based on elemental analysis. *Values are averages of two reported measurements.

Reaction mixtures of InX_3 (X = Cl, Br, I) with $P(SiMe_3)_3$ were sonicated in pentane solution for 20 min and subsequently stirred at room temperature for 2 d prior to solvent removal under reduced pressure.[36] The resulting powders were subsequently loaded into a sublimator and annealed under vacuum at 400 °C for 3 h, thereby producing indium phosphide. Interestingly, the reaction of $P(SiMe_3)_3$ and InI_3 in toluene/ether solution produced $I_3In{\bullet}P(SiMe_3)_3$ as a white-yellow powder after stirring the reaction mixture for 2 d followed by recrystallization from toluene solution at -15 °C. Barron et al. reported the formation of a different product from the same protocol.[33] The isolation of two different products from the same reaction may be a consequence of using different reaction times and temperatures. It is pertinent to mention that indium arsenide can be produced from the reaction of InX_3 and $As(SiMe_3)_3$ using the same procedure.

$$InX_3 + E(SiMe_3)_3 \rightarrow InE + 3\ XSiMe_3$$

$$E = P, X = Cl, Br; E = As, X = Cl, Br, I$$

$$InI_3 + P(SiMe_3)_3 \rightarrow I_3In{\bullet}P(SiMe_3)_3 \rightarrow InP + 3\ ISiMe_3$$

It is likely that the domain sizes of indium phosphide and indium arsenide were strongly influenced by temperature and the characteristics of solvent used in the synthesis. The oxides of indium and arsenic were evident in the X-ray photoelectron spectroscopic (XPS) analysis of the indium arsenide produced via the reaction of $InCl_3$ and $As(SiMe_3)_3$. The pertinent product analyses are presented in Table 1.3.

Table 1.3: Product analyses for indium phosphide and indium arsenide resulting from the dehalosilylation reaction, $InX_3 + E(SiMe_3)_3$.

$InX_3 + E(SiMe_3)_3 \rightarrow InE + 3\ XSiMe_3$					
X, E	Precipitate	In:E mole ratio[a]	Purity[a]	Impurities[a] (weight %)	Domain Size[b] (nm)
Cl, P	Pale yellow to bright yellow, orange, brown-black	1.00:1.09	91.53%		3.7
Br, P	Yellow-orange to brown-black	1.00:1.03	93.08%		4
I, P	White-yellow to brown-black	1.00:1.14	84.06%	C: 0.83 H: 0.28 I: ≤0.50	2.5
Cl, As	Yellow to orange, red, brown, brown-black	1.00:1.03	99.47%	C: 0.42 H: 0.10 Cl: 0.36	9
Br, As	Red-brown to black	1.00:1.00	99.65%		10
I, As	Red-orange to black	1.10:1.00	85.95%		12

[a]based on elemental analysis. [b]based on XRD data.

The adducts $X_3Ga{\bullet}P(SiMe_3)_3$ (X = Cl, Br, I) were prepared via the reaction of GaX_3 and $P(SiMe_3)_3$ in hexane or pentane solution. The reaction mixtures were stirred overnight at room temperature.[37]

$$GaX_3 + P(SiMe_3)_3 \rightarrow X_3Ga{\bullet}P(SiMe_3)_3 \rightarrow GaP + 3\ XSiMe_3$$

$$X = Cl, Br, I$$

The pyrolyses of the adducts were performed in a sublimator under a static vacuum. The temperature of each reaction mixture was slowly ramped up to 450 °C and held at

that temperature for 12 h. The identity of the product was confirmed to be that of gallium phosphide by XRD. A summary of the purities of the materials is presented in Table 1.4. The TGA plots provide evidence for the incomplete elimination of the third equivalent of $XSiMe_3$ for X = Cl, Br, and I. The incomplete nature of these reactions resulted in carbon, silicon, and halide contamination in the gallium phosphide products. Furthermore, methane evolution was also evident and results from the decomposition of $SiMe_3$ groups at temperatures as low as 200 °C. For the foregoing reasons, future pyrolyses should be carried out as completely as possible below this temperature prior to subsequent heating.

Table 1.4: Analytical data for the gallium phosphide produced via the pyrolysis of $X_3Ga{\bullet}P(SiMe_3)_3$.

$X_3Ga{\bullet}P(SiMe_3)_3 \rightarrow GaP + 3\ XSiMe_3$			
X	Ga:P mole ratio[a]	Impurities[a] (weight %)	Domain Size[b] (nm)
Cl	1.01:1.00	C: 4.47	5
Br	0.94:1.00	C: 0.73	4.6
I	0.89:1.00	C: 5.40 H: 0.84 Si: 3.75	4

[a]based on elemental analyses. [b]estimated from XRD data.

Alcoholysis Precursors

In 1988, Theopold et al. reported the synthesis of the first monomeric arsinogallane and the subsequent alcoholysis of this precursor to afford GaAs.[38] A pentane solution of $(Cp^*_2GaCl)_2$ (Cp* = pentamethylcyclopentadienyl) was treated with two equivalents of $LiAs(SiMe_3)_2$, resulting in salt elimination and the production of $Cp^*_2GaAs(SiMe_3)_2$, which is soluble in common organic solvents and is stable up to 60 °C in an inert gas atmosphere. Subsequent reaction of this precursor with an excess of *tert*-butanol in a pentane solution resulted in the elimination of two equivalents of

pentamethylcyclopentadiene and *tert*-butyl(trimethylsilyl)ether. This reaction was accompanied by the formation of a red powder that was subsequently identified as GaAs by elemental analysis and SEM. Subsequent to annealing at 500 °C for 48 hours, the XRD pattern of this material was found to match that of crystalline GaAs. Further details of precursor synthesis and the consequences of *tert*-butanol treatment are summarized in Scheme 1.4. Monitoring of the absorption spectra subsequent to the *tert*-butanol treatment revealed a red shift in the reaction mixture as time progressed. Specifically, the color of the reaction changed from faint yellow for the precursor alone to an orange color following the addition of an excess of *tert*-butanol. Eventually, the reaction mixture assumed a red-brown color. The above observations are indicative of the merging of discrete energy levels of the individual molecules into bands of the bulk material. This is a consequence of the aggregation of GaAs to form dimers, clusters, microscopic particles, and ultimately a finely divided macroscopic powder.

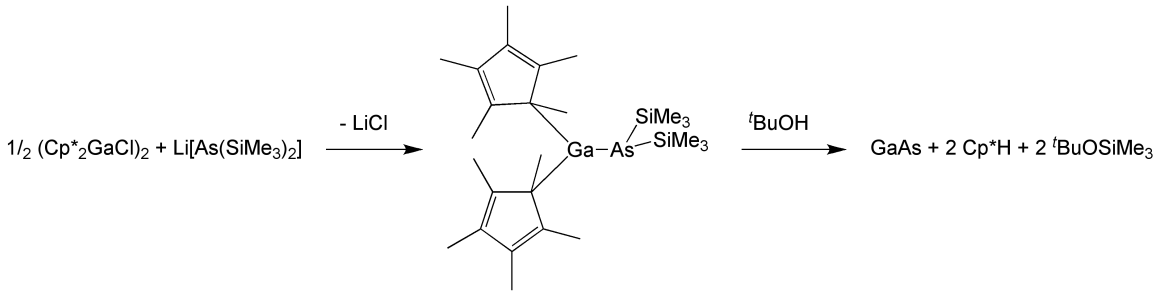

Scheme 1.4: Arsinogallane synthesis and subsequent alcoholysis to yield GaAs.

The synthesis and alcoholysis of four dimer molecules containing covalent bonded indium and phosphorus were also reported by Theopold et al. in 1991.[39] These compounds were prepared via the reaction of alkylindium chlorides and either $P(SiMe_3)_3$ or $LiP(SiMe_3)_2$. Treatment of these precursors with an excess of methanol resulted in the elimination of hydrocarbons and methyl(trimethylsilyl)ether along with a fine orange

powder that was identified as indium phosphide on the basis of elemental analysis. NMR studies of the methanol treatment revealed the presence of a dialkylmethoxyindium species along with phosphine, indicating that heterolytic cleavage of the bond between indium and phosphorus took place prior to the precipitation of indium phosphide. Based on the latter observation, the mechanism shown in Scheme 1.5 is proposed. As the reaction progressed, the color changed from colorless to yellow, then orange and finally to dark red-brown. Monitoring this reaction by means of UV-vis spectroscopy revealed a red shift of the absorption onset with time. Akin to the GaAs system, these observations are indicative of the growth of indium phosphide clusters from monomers.

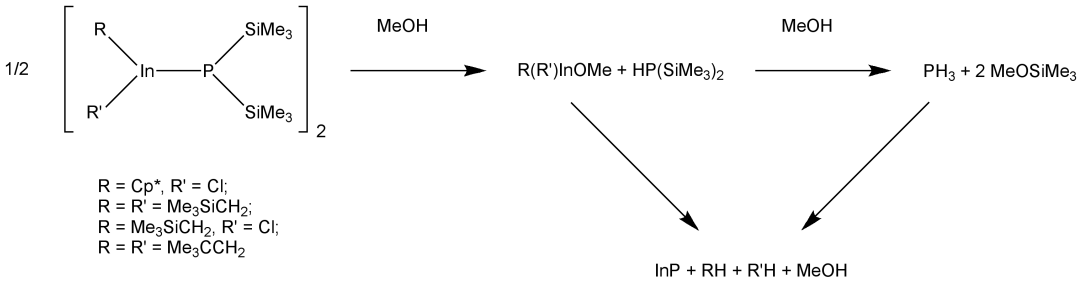

Scheme 1.5: Proposed mechanism for the alcoholysis of indium phosphide precursors.

Research Objectives

Using β-hydride elimination routes, Cowley and Jones, et al. prepared indium phosphide and indium antimonide films starting from $(Me_2InE^tBu_2)_n$ (E = P, n = 2; E = Sb, n = 3).[15,40] Gallium phosphide and indium phosphide nanocrystals have been synthesized by O'Brien et al. via thermolysis of $M(P^tBu_2)_3$ (M = Ga, In) in alkylpyridine.[41,42] O'Brien et al. also succeeded in synthesizing hexadecylamine-capped GaAs and indium arsenide nanoparticles starting from $(R_2MAs^tBu_2)_2$ (M = Ga, R = Me;

M = In, R = Et).[43,44] The number of boron-arsenic complexes that feature hydrocarbon ligands and sigma bonds between boron and arsenic are very limited and confined to Ph_2BAsPh_2, (p-tolyl)$_2$BAsPh$_2$;[45] $(H_2BAsMe_2)_3$, $(H_2BAsMe_2)_4$, $(Me_2BAsMe_2)_3$, $(Ph_2BAsMe_2)_x$;[46] $(Mes)_2BAs^iPr_2$ and $(Mes)_2BAs^tBu_2$.[47] Unfortunately none of these complexes are suitable for β-hydride elimination and film growth studies. Several boron and arsenic adducts and dimers that feature ligands that in principle are capable of undergoing dehalosilylation reactions have been reported by Wells et al.[48,49] However, pyrolysis studies of these precursors were not reported due to the high levels of contamination that were evident in preliminary attempts. Given the abundance of literature on other III-V compounds, the available information on boron arsenide is surprisingly sparse and single source precursor work is limited to the reactions discussed below.

RESULTS AND DISCUSSION

Dehalosilylation Precursors

In order to explore the pyrolysis approach to boron arsenide synthesis, the compounds $X_3B{\bullet}As(SiMe_3)_3$ (X = Cl (**1**), Br (**2**), I (**3**)) and $[X_2BAs(SiMe_3)_2]_2$ (X = Cl (**4**), Br (**5**), I (**6**)) were prepared using a modification of the syntheses first reported by Wells et al. Wells et al. prepared compounds **1** and **2** by the independent reactions of BCl_3 and BBr_3 respectively with $As(SiMe_3)_3$ in a pentane solution that was stirred under an argon atmosphere at room temperature.[48] After 48 h, the solvent was removed under reduced pressure, which resulted in the production of off-white or yellow solids. These solids were collected and washed in pentane solution, resulting in the isolation of **1** and **2** in 88.3% and 88.0% yields, respectively. Interestingly, the analogous reaction with BI_3 resulted in formation of the dimer, **6**, in 44.4% yield. A low-temperature route using a

two-bulbed flask was employed for the synthesis of **3**.[49] The upper bulb was charged with $As(SiMe_3)_3$ in pentane solution while neat BI_3 was placed in the lower bulb at -78 °C. The arsenic compound was then added to the boron trihalide slowly and the reaction mixture was stirred for 2 h at -78 °C, following which the solvent was removed under vacuum at 0 °C, leaving behind white solid **3** in 89.3% yield. Crystals of **1**-**3** and **6** suitable for X-ray structural determinations were grown from toluene solutions at -15 °C. The modified syntheses represent a significant improvement in simplicity. Typically, the boron trihalide was weighed into a vial in a drybox, and a slight excess of $As(SiMe_3)_3$ was weighed into an amber vial. Each compound was dissolved in hexane and the boron trihalide solution was added dropwise to the arsine solution. A white solid was deposited immediately and the resulting mixture was stirred for 2 h at room temperature in a drybox. The precipitate was then filtered off and rinsed with fresh solvent. Compounds **1**, **2**, and **3** are isolated in 81.4%, 79.2% and 74.2% yields. The identity of each compound was determined on the basis of multinuclear NMR spectroscopy by comparison with literature values.

Wells et al. prepared **4** and **5** using a two-bulbed flask. A pentane solution of BX_3 was placed in the upper bulb and a toluene solution of $LiAs(SiMe_3)_2$ was added to the lower bulb at -78 °C.[48] The BX_3 was added to the clear, colorless arsenide solution, which gradually developed a cloudy, yellow appearance. The reaction mixture was allowed to warm to room temperature and subsequently stirred in the dark for 48 h for X = Cl and 12 h for X = Br. The reaction mixture was then filtered to remove LiCl and the solvent was removed under reduced pressure to produce **4** and **5** as off-white or yellow powders, which were rinsed in pentane and isolated in 36.0% and 20.8% yields, respectively. Moreover, it was possible to grow X-ray quality crystals of **4** and **5** in toluene solution at -15 °C. This reaction was repeated successfully in the case of **5** at

room temperature after stirring overnight. However, the method of accessing **4**-**6** described here was to heat adducts **1**-**3** to 100-115 °C under vacuum for 2 h. Multinuclear NMR spectra were used to confirm the identities of each dimer by comparison with literature values. The synthesis of **1**-**6** is displayed in Scheme 1.6.

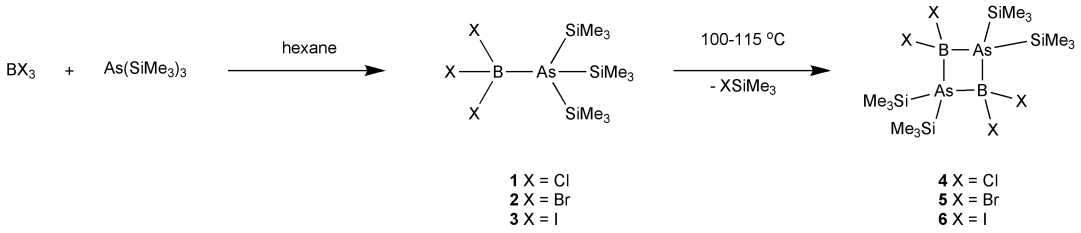

Scheme 1.6: The synthesis of adducts and dimers for dehalosilylation.

In order to conduct pyrolysis studies, colorless crystals of **3** were heated under vacuum to 100 °C which resulted in the formation of a fine white powder that was identified as **6** on the basis of ^{1}H, ^{13}C, and ^{11}B NMR spectroscopy. Upon further heating to 130 °C and eventually to 155 °C, ^{11}B NMR spectroscopic examination indicated that the material was still in the dimeric form. However, after heating to 190 °C, the material changed color from off-white to brown and became insoluble, thus precluding NMR analysis. By 250 °C, the material assumed a dark brown color. It was not possible to record an XRD pattern for this material. However, a high-resolution XPS analysis revealed a B:As mole ratio of 1.00:1.98. The survey scan also revealed the presence of iodine and silicon, along with carbon and oxygen. Moreover, the boron peak is split into two components, which is indicative of the presence of two boron species. While one of these peaks may be attributable to BAs, the source of the additional peak is unknown. The pertinent spectra are displayed in Figures 1.2 and 1.3 and quantification data are available in Table 1.5.

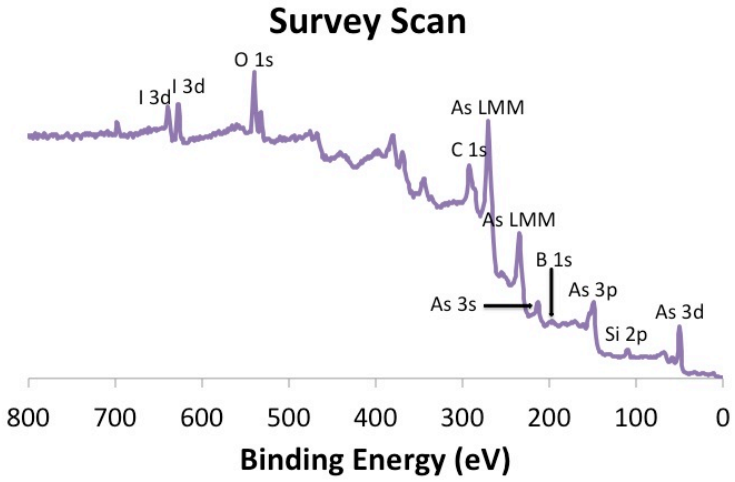

Figure 1.2: XPS survey scan of the material produced by the pyrolysis of $I_3B{\bullet}As(SiMe_3)_3$ at 250 °C.

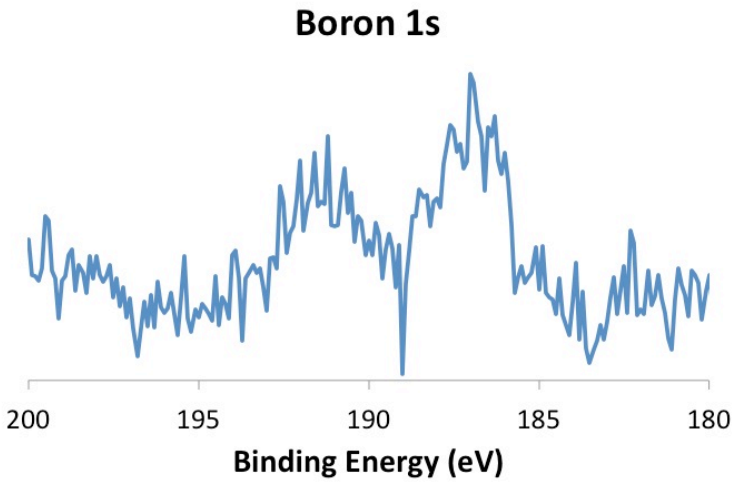

Figure 1.3: XPS high-resolution boron 1s spectrum of the material produced by the pyrolysis of $I_3B{\bullet}As(SiMe_3)_3$ at 250 °C.

Table 1.5: XPS quantification data for the material produced by the pyrolysis of $I_3B{\bullet}As(SiMe_3)_3$ at 250 °C.

Peak	Position (eV)	R.S.F.	Area	Atomic % Conc.
B 1s	187.00	0.159	300.9	33.58
As 3d	40.15	0.677	2457.1	66.42

Colorless crystals of **2** were grown from a toluene solution at -40 °C and loaded in a quartz boat, which subsequently was placed in a tube furnace. Upon opening the reaction vessel to vacuum, the crystals collapsed into an off-white powder. In one pyrolysis study, the sample was heated to 115 °C for 2 h, following which the resulting solid was identified as the dimer on the basis of ^{1}H and ^{11}B NMR spectroscopy. In a second pyrolysis study, intermediate steps were not collected and characterized in order to avoid possible oxygen and moisture exposure. Instead, the powder was heated directly to 500 °C under vacuum for 3 h during which time it gradually assumed a dark brown color. No XRD pattern was evident, thus implying that the dark brown powder was amorphous. As shown in Figure 1.4 and quantified in Table 1.6, a high-resolution XPS analysis revealed a B:As mole ratio of 1.00:0.41 accompanied by bromine and silicon impurities of 14.54% and 14.97% by weight, respectively. The bromine and silicon contamination was possibly a result of ramping the temperature unduly quickly. The differences in the volatilities of boron and arsenic are evident from these results, since arsenic was preferentially eliminated at high temperature under vacuum. Further proof of this conclusion became evident as the sample was further heated to 800 °C. The XPS analysis of this new material, which is displayed in Figure 1.5 and quantified in Table 1.7, indicated the complete absence of arsenic.

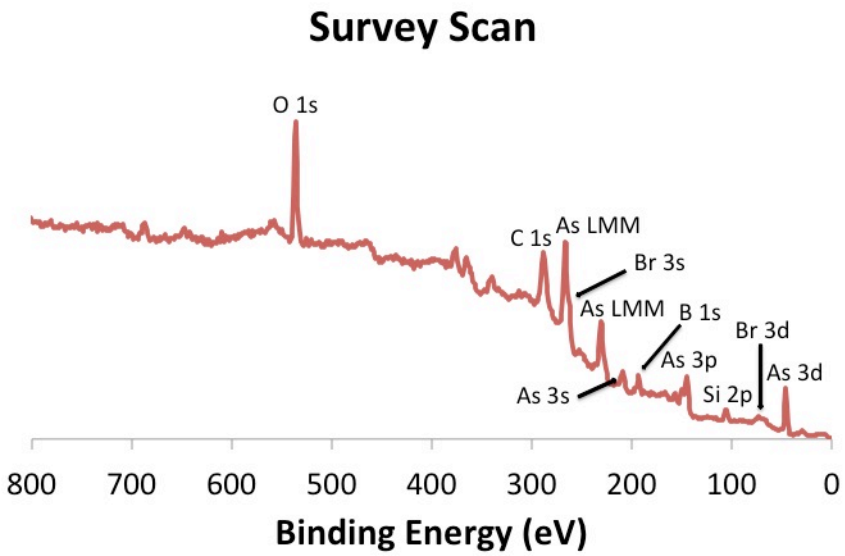

Figure 1.4: XPS survey scan of the material produced by the pyrolysis of $Br_3B{\bullet}As(SiMe_3)_3$ at 500 °C.

Table 1.6: XPS quantification data for the material produced by the pyrolysis of $Br_3B{\bullet}As(SiMe_3)_3$ at 500 °C.

Peak	Position (eV)	R.S.F.	Area	Atomic % Conc.	Mass % Conc.
B 1s	192.60	0.159	1153.5	56.01	19.12
	193.30		1219.9	53.74	17.96
As 3d	45.45	0.677	1832.3	21.58	50.99
	46.45		2141.0	22.87	52.94
Br 3d	72.85	1.055	817.1	6.15	15.49
	74.35		806.0	5.50	13.58
Si 2p	106.00	0.328	675.8	16.26	14.41
	106.50		819.4	17.89	15.52

The presence of duplicate data is due to the analysis of two spots on the material.

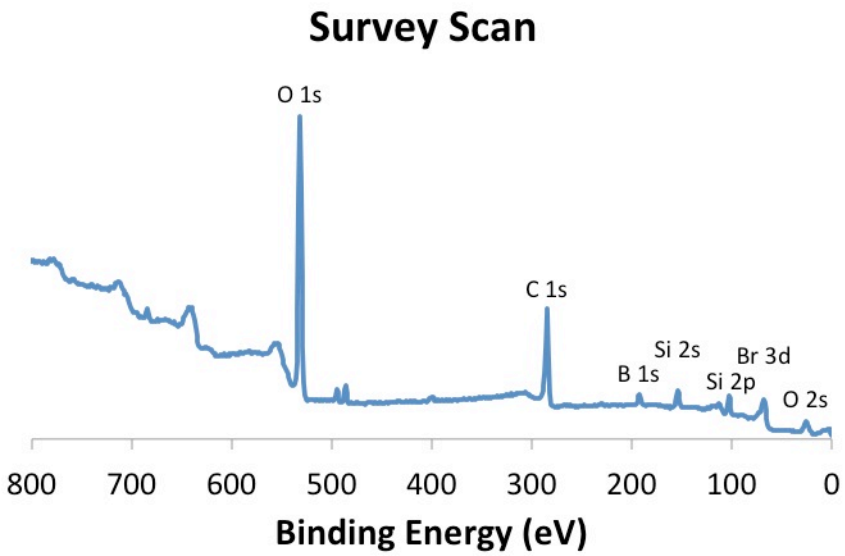

Figure 1.5: XPS survey scan of the material produced by the pyrolysis of $Br_3B{\bullet}As(SiMe_3)_3$ at 800 °C.

Table 1.7: XPS quantification data for the material produced by the pyrolysis of $Br_3B{\bullet}As(SiMe_3)_3$ at 800 °C.

Peak	Position (eV)	R.S.F.	Area	Atomic % Conc.	Mass % Conc.
B 1s	192.40	0.159	718.5	35.15	11.04
	193.80		1119.2	39.21	13.42
As 3d	45.55	0.677	50.8	0.60	1.31
	44.75		65.3	0.55	1.31
Br 3d	68.05	1.055	3091.9	23.45	54.39
	67.65		3567.4	19.38	48.97
Si 2p	102.90	0.328	1682.3	40.80	33.26
	102.90		2352.6	40.86	36.30

The presence of duplicate data is due to the analysis of two spots on the material.

Ramping the temperature unduly quickly in pyrolysis of single source precursors may result in ligand contamination in the desired materials. Additionally, undesired ligand decomposition and side reactions may occur at elevated temperatures, such as the decomposition of $SiMe_3$ groups, which begins at temperatures as low as 200 °C under reduced pressure.[37] For these reasons, colorless crystals of **1** were heated to 200 °C for

10 h before the temperature was further increased so that ligand elimination could occur as completely as possible at a relatively modest temperature. The temperature was then increased to 350 °C for 2 h. This temperature was chosen because it is well below 500 °C, which was thought to cause the undesired elimination of elemental arsenic in the pyrolysis of the analogous bromide system discussed above. Elemental analysis of the resulting dark brown powder revealed a B:As mole ratio of 1.00:1.12, accompanied by carbon, hydrogen, chloride, and silicon contamination, quantified in Table 1.8.

Table 1.8: Elemental analysis data for the material produced by the pyrolysis of $Cl_3B{\bullet}As(SiMe_3)_3$ at 350 °C.

Element	Elemental Analysis	Atomic % Conc.
Boron	5.86%	17.95
Arsenic	45.60%	20.17
Carbon	6.12%	16.89
Hydrogen	1.23%	40.40
Chloride	4.93%	4.60
Silicon	90 ppm	0.01

Alcoholysis Precursors

An arsinoborane, $Cp^*_2BAs(SiMe_3)_2$ (**7**), analogous to Theopold's arsinogallane[38] was isolated from the reaction of Cp^*_2BCl with one equivalent of $LiAs(SiMe_3)_2$. The reaction mixture was stirred overnight in hexane at room temperature resulting in the formation of **7** and LiCl. The precipitated salt was removed by filtration and compound **7** was isolated as a yellow-orange semi-solid in 85.5% yield. The ^1H NMR spectrum of **7** exhibits only two signals in a 30:18 ratio. The larger, broad signal is attributable to the Cp* protons and the less intense one is due to the $SiMe_3$ protons. Crystals suitable for X-ray diffraction were grown from a saturated pentane solution at -40 °C. As illustrated in Figure 1.6, the structure is monomeric with an approximately trigonal planar geometry at the boron center and trigonal pyramidal geometry at the arsenic center. Due to the small

size of the boron atom, the pentamethylcyclopentadienide rings underwent a Diels Alder reaction that resulted in ring fusion. Details of data collection, structure solution, and refinement are compiled in Table A1.1 and selected metrical parameters are listed in Tables A1.2 and A1.3. The precursor synthesis and alcoholysis is displayed in Scheme 1.7.

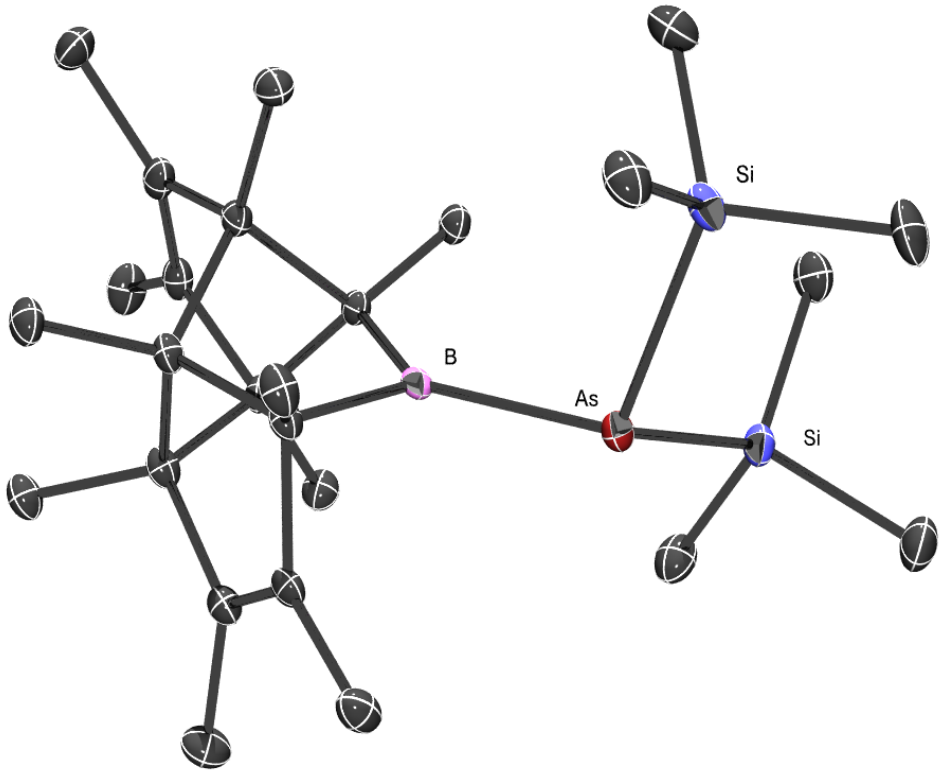

Figure 1.6: Molecular structure of $Cp^*_2BAs(SiMe_3)_2$ showing the fused nature of the Cp* rings.

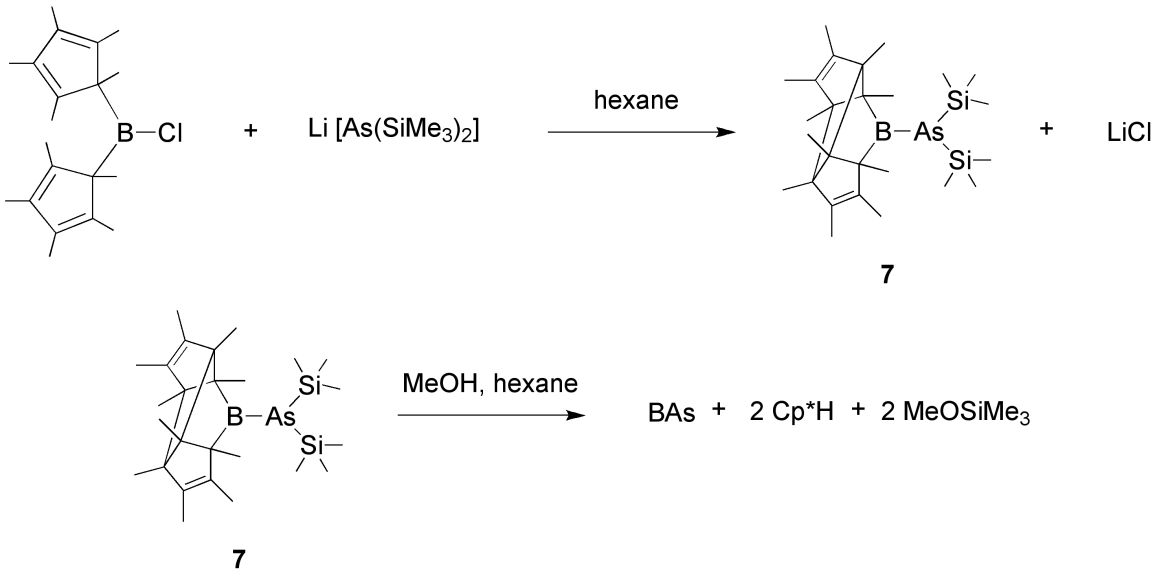

Scheme 1.7: Precursor synthesis and alcoholysis for $Cp^*_2BAs(SiMe_3)_2$.

This single source precursor was treated with three equivalents of methanol then stirred in hexane overnight. The resulting solution was analyzed by ^1H NMR spectroscopy, which revealed the presence of Cp*H and $MeOSiMe_3$. The resulting red-brown material was rinsed three times with fresh solvent and subsequently analyzed by XPS. The XPS data are presented in Figures 1.7 and 1.8 and quantified in Table 1.9. The product featured a 1.00:1.39 B:As mole ratio and was contaminated by silicon to the extent of 10.92% by weight. Additionally, the arsenic 3d peak appeared to consist of two species. While the major peak is most likely due to BAs, the identity of the other minor peak is unknown. It is possible that the fused Cp* rings do not hydrolyze as readily as those of the corresponding monomeric species.

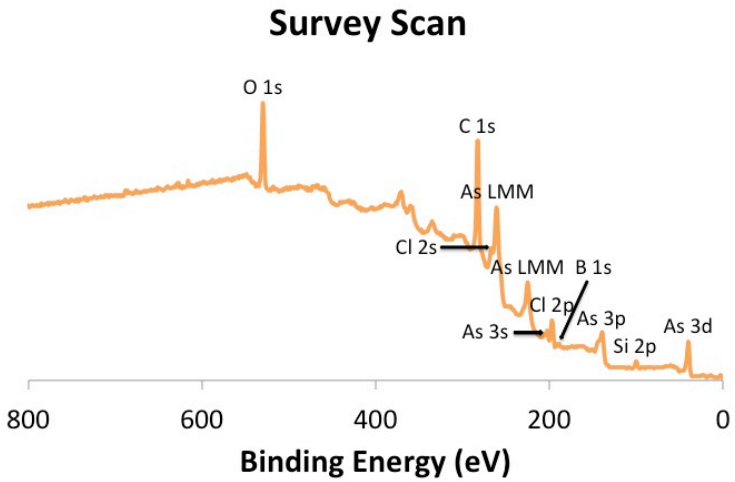

Figure 1.7: XPS survey scan of the material produced by the alcoholysis of $Cp^*_2BAs(SiMe_3)_2$ at room temperature.

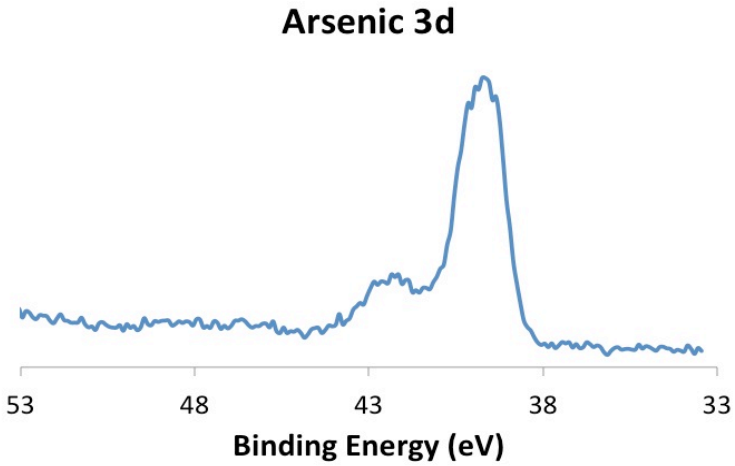

Figure 1.8: XPS high-resolution arsenic 3d spectrum of the material produced by the alcoholysis of $Cp^*_2BAs(SiMe_3)_2$ at room temperature.

Table 1.9: XPS quantification data for the material produced by the alcoholysis of $Cp^*_2BAs(SiMe_3)_2$ at room temperature.

Peak	Position (eV)	R.S.F.	Area	Atomic % Conc.	Mass % Conc.
B 1s	190.20	0.159	462.3	34.57	8.38
As 3d	39.65	0.677	2651.2	48.08	80.70
Si 2p	99.70	0.328	468.4	17.36	10.92

Other Synthetic Approaches

As it became evident that single source precursor methods were not yielding high-quality BAs, other synthetic approaches were considered. Boron phosphide ultrafine powders and nanocrystals have been prepared in an autoclave at temperatures ranging from 300-600 °C from PCl_3 and various sources of boron including elemental boron, BBr_3, and $NaBF_4$.[50] Lithium or sodium metals served as reducing agents in some cases, and benzene served as a solvent in some cases. The identity of the materials produced was confirmed using XRD. In the reactions involving benzene as a solvent, small amounts of carbon contamination were detected. The materials produced from solvent-free reactions were free of carbon contamination. However, it is undesirable to heat $AsCl_3$ to 300-600 °C, so analogous reactions with arsenic were not attempted.

The independent metathetical reactions of Na_3As with BX_3 (X = Cl, Br) resulted in the formation of sodium salts, which were identified by XRD, along with insoluble, amorphous materials. The amorphous materials were analyzed by XPS and a B:As mole ratio of 1.00:0.90 was found when X = Cl. When X = Br, a mole ratio of 1.00:0.40 was found. Each material also had significant sodium and halide contamination. These materials were annealed in sealed evacuated silica tubes at 500 °C for 48 h. Evidently, elemental arsenic was eliminated from the products, presumably due to its relative volatility, since the B:As mole ratio after annealing was 1.00:0.79 for X = Cl. For X = Br, very little arsenic was detected by XPS after annealing. Additionally, the XRD pattern of elemental arsenic was observed for metallic products that appeared in both samples after annealing, further indicating elimination of elemental arsenic from the materials. The XPS spectra for the independent metathetical reactions of Na_3As and BX_3 (X = Cl, Br) are displayed in Figures 1.9 and 1.10, respectively and quantification data are found in Tables 1.10 and 1.11, respectively.

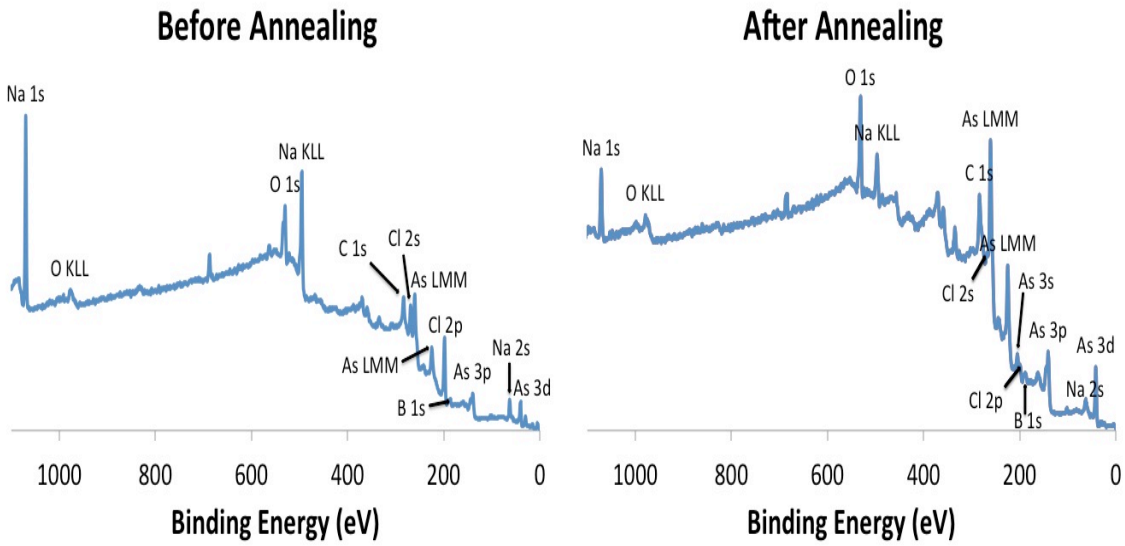

Figure 1.9: XPS survey scans of the product of the metathetical reaction of Na_3As with BCl_3 before and after annealing.

Table 1.10: XPS quantification data for the product of the metathetical reaction of Na_3As with BCl_3 before and after annealing.

Before Annealing					
Peak	R.S.F.	Position (eV)	Area	Atomic % Conc.	Mass % Conc.
B 1s	0.159	186.75	835.2	15.64	5.22
As 3d	0.677	40.35	3178.9	14.09	32.55
Na 1s	1.685	1070.30	20877.7	37.88	26.85
Cl 2p	0.891	198.45	9705.8	32.38	35.39
After Annealing					
Peak	R.S.F.	Position (eV)	Area	Atomic % Conc.	Mass % Conc.
B 1s	0.159	187.55	1544.2	41.78	12.59
As 3d	0.677	41.65	5117.0	32.78	68.39
Na 1s	1.685	1071.50	6709.7	17.59	11.26
Cl 2p	0.891	199.45	1630.6	7.86	7.76

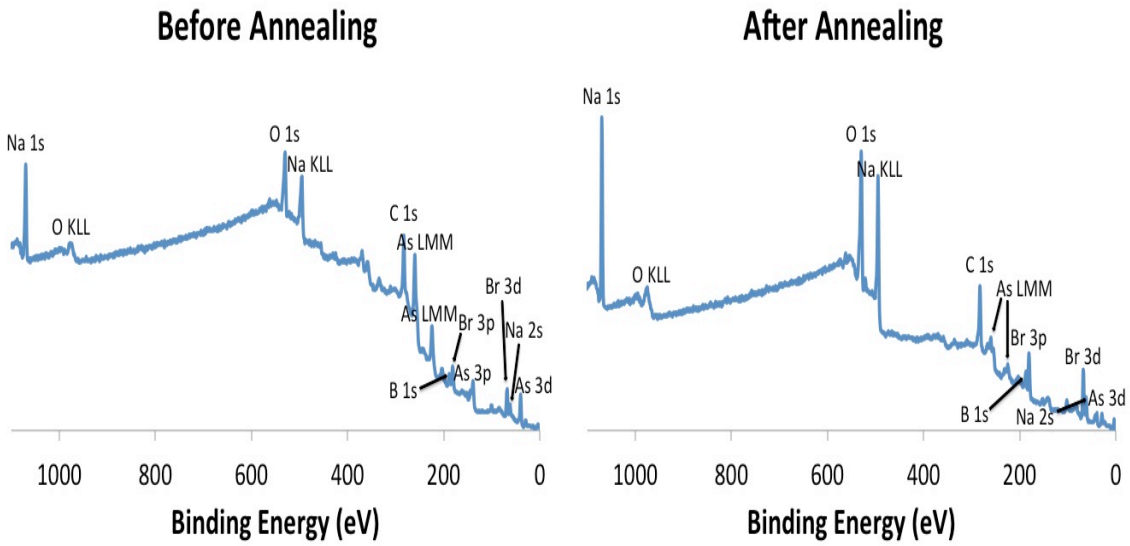

Figure 1.10: XPS survey scans of the product of the metathetical reaction of Na_3As with BBr_3 before and after annealing.

Table 1.11: XPS quantification data for the product of the metathetical reaction of Na_3As with BBr_3 before and after annealing.

Before Annealing					
Peak	R.S.F.	Position (eV)	Area	Atomic % Conc.	Mass % Conc.
B 1s	0.159	188.25	2303.8	44.46	14.31
As 3d	0.677	40.25	3928.6	17.95	40.01
Na 1s	1.685	1070.00	13794.6	25.80	17.64
Br 3d	1.055	68.90	4025.5	11.79	28.03
After Annealing					
Peak	R.S.F.	Position (eV)	Area	Atomic % Conc.	Mass % Conc.
B 1s	0.159	187.45	2781.0	48.98	18.78
As 3d	0.677	39.85	1567.5	6.54	17.35
Na 1s	1.685	1070.00	18034.5	30.78	25.07
Br 3d	1.055	67.70	5124.2	13.70	38.79

CONCLUSIONS

The use of single source precursors to prepare III-V semiconductor materials is intended to address the problems associated with dual source methods. However, the synthesis of boron arsenide with an exact one-to-one stoichiometry proved to be more difficult than originally anticipated. For each precursor, ligand elimination failed to produce materials with the desired elemental B:As ratio that were free of contamination. None of the routes employed here produced materials that were satisfactory for photoelectrochemical studies. For this reason, the reaction of the elements was pursued and will be presented in the following chapter.

EXPERIMENTAL DETAILS

General Methods

All of syntheses were performed under a dry, oxygen-free argon atmosphere or vacuum using standard Schlenk line and dry box techniques. All glassware was dried at least 24 h in a 120 °C oven prior to use. Hexane and toluene were distilled over sodium with a sodium benzophenone ketyl indicator and were degassed before use. Methanol was distilled and stored over molecular sieves. Deuterated solvents were purchased from Cambridge Isotopes and stored over molecular sieves in the dry box prior to use. Tris(trimethylsilyl)arsine and lithium bis(trimethylsilyl)arsenide were prepared according to literature procedures,[51] as was bis(pentamethylcyclopentadienyl)chloroborane[52] and sodium arsenide.[53] Boron trichloride (1 *M* solution in hexane) and boron tribromide (99.9%) were purchased from Acros Organics and used without further purification. Boron triiodide (98+%) was purchased from Alfa Aesar and used as received. The NMR spectra were recorded on a Varian 300 Unity Plus spectrometer (300 MHz, 298 K) or a Varian DirectDrive 600 (600 MHz, 298 K). For ^{1}H and ^{13}C spectra, chemical shifts are

referenced to the deuterated solvent. An external standard, BF_3 ethyl ether complex, was used as a reference for ^{11}B NMR. Mass spectrometry was performed using a Thermo Finngan TSQ 700 instrument.

Instruments

X-ray Photoelectron Spectroscopy

The XPS spectra were recorded on a Kratos Axis Ultra X-ray photoelectron spectrometer utilizing a monochromated Al Kα X-ray source. All spectra were collected with a pass energy of 20 eV. CasaXPS software version 2.3.16 was used to determine the stoichiometries of the samples from the corrected peak areas by applying the relative sensitivity factors of 0.159, 1.685, 0.328, 0.891, 0.677, and 1.055 for B 1s, Na 1s, Si 2p, Cl 2p, As 3d, and Br 3d respectively.

X-ray Crystallography

The X-ray data were collected at 153 K on a Rigaku AFC12 with Saturn 724+ CCD diffractometer with graphite monochromated Mo-Kα radiation (λ = 0.71073 Å). The sample was covered in mineral oil and mounted on a nylon thread loop. The structure was solved by direct methods using full-matrix least-squares methods in conjunction with the SHELX 97 program package. The coordinates of non-hydrogen atoms were refined anisotropically. Hydrogen atoms were included in the calculations isotropically but not refined. The total number of reflections, collection ranges, and final R-values are listed in the crystallographic data table.

Synthesis and Decomposition Studies of Precursors

$Cl_3B \bullet As(SiMe_3)_3$ (1)

In a dry box, a 1*M* hexane solution of BCl_3 (0.35 mL, 0.35 mmol) was added dropwise to a hexane solution of $As(SiMe_3)_3$ (0.1048 g, 0.3559 mmol) in an 8 mL amber vial. A white precipitate crashed out immediately. The slurry was stirred overnight at room temperature before the solvent was removed under reduced pressure to yield a pale yellow/orange solid (0.1193 g, 0.2898 mmol, 81.4% yield). The solid was rinsed three times in hexane and colorless crystals were grown at -40 °C from a saturated toluene solution. ^{1}H NMR (300 MHz, C_6D_6) δ: 0.320 (s); $^{11}B\{^{1}H\}$ NMR (96 MHz, C_6D_6) δ: 4.392 (s); $^{13}C\{^{1}H\}$ NMR (75 MHz, C_6D_6) δ: 1.647 (s).

$Br_3B \bullet As(SiMe_3)_3$ (2)

In a dry box, a hexane solution of BBr_3 (0.0908 g, 0.3623 mmol) was added dropwise to a hexane solution of $As(SiMe_3)_3$ (0.1046 g, 0.3552 mmol) in an 8 mL amber vial. A white precipitate crashed out immediately. The slurry was stirred overnight at room temperature before the precipitate was isolated by removal of solvent under reduced pressure to yield a pale yellow solid (0.1533 g, 0.2813 mmol, 79.2% yield). The solid was rinsed three times in fresh hexane and colorless crystals were grown at -40 °C from a saturated toluene solution. ^{1}H NMR (300 MHz, C_6D_6) δ: 0.358 (s); $^{11}B\{^{1}H\}$ NMR (96 MHz, C_6D_6) δ: -18.757 (s).

$I_3B \bullet As(SiMe_3)_3$ (3)

In a dry box, a hexane solution of BI_3 (0.1465 g, 0.3742 mmol) was added dropwise to a hexane solution of $As(SiMe_3)_3$ (0.1085 g, 0.3684 mmol) in an 8 mL amber vial. A white precipitate crashed out immediately. The slurry was stirred overnight at room temperature before the solvent was removed under reduced pressure to yield a

tan/orange solid (0.1875 g, 0.2733 mmol, 74.2% yield). The solid was rinsed three times in fresh hexane and colorless crystals were grown at -40 °C from a saturated toluene solution. ^{1}H NMR (300 MHz, C_6D_6) δ: 0.430 (s); ^{11}B{^{1}H} NMR (96 MHz, C_6D_6) δ: -88.104 (s); ^{13}C{^{1}H} NMR (75 MHz, C_6D_6) δ: 2.430 (s).

[Cl$_2$BAs(SiMe$_3$)$_2$]$_2$ (4)

The adduct **1** (0.3171 g, 0.7703 mmol) was placed in a 25 mL round bottom flask and heated under reduced pressure to 100 °C overnight. The formation of **4** (0.2033 g, 0.3355 mmol, 87.1% yield) was confirmed by NMR. ^{1}H NMR (300 MHz, C_6D_6) δ: 0.501 (s), 0.323 (s); ^{11}B{^{1}H} NMR (96 MHz, C_6D_6) δ: 4.401 (s), -1.784 (s); ^{13}C{^{1}H} NMR (75 MHz, C_6D_6) δ: 2.432 (s), 1.646 (s).

[Br$_2$BAs(SiMe$_3$)$_2$]$_2$ (5)

The adduct **2** (0.3310 g, 0.6073 mmol) was placed in a quartz boat, which was heated in a tube furnace under vacuum to 115 °C for 2 h. No visible change was observed, however the formation of **5** (0.1953 g, 0.2492 mmol, 82.1% yield) was confirmed by NMR. ^{1}H NMR (300 MHz, C_6D_6) δ: 0.555 (s); ^{11}B{^{1}H} NMR (96 MHz, C_6D_6) δ: -15.815 (s).

[I$_2$BAs(SiMe$_3$)$_2$]$_2$ (6)

The adduct **3** was placed in a Schlenk flask, which was heated under vacuum to 100 °C for 2 h. No visible change was observed, however the formation of **6** was confirmed by NMR. ^{1}H NMR (300 MHz, C_6D_6) δ: 0.636 (s); ^{11}B{^{1}H} NMR (96 MHz, C_6D_6) δ: -55.607 (s); ^{13}C{^{1}H} NMR (75 MHz, C_6D_6) δ: 3.442 (s).

Thermolysis of Cl_3B•$As(SiMe_3)_3$ (1)

Colorless crystals of **1** (0.9297 g, 2.258 mmol) were placed in a Schlenk flask and heated under reduced pressure in a sand bath to 200 °C for 10 h. The temperature was then increased to 350 °C for 2 h, followed by slow cooling to room temperature. A dark brown powder (0.1700 g) was collected. B:As mole ratio 1.00:1.12.

Thermolysis of Br_3B•$As(SiMe_3)_3$ (2)

Colorless crystals of **2** were placed in a quartz boat in a tube furnace at room temperature. The furnace was then heated to 500 °C under vacuum for 3 h, at which point a dark brown powder was collected. B:As mole ratio 1.00:0.41; Br and Si 14.54% and 14.97% by weight, respectively.

Thermolysis of I_3B•$As(SiMe_3)_3$ (3)

Colorless crystals of **3** were placed in a Schlenk flask and heated first to 100 °C for 2 h, then temperature was slowly ramped to 250 °C. A dark brown powder was collected. B:As mole ratio 1.00:1.98.

$Cp^*_2BAs(SiMe_3)_2$ (7)

A 100 mL Schlenk flask was charged with Cp^*_2BCl (0.86 g, 2.72 mmol) and $LiAs(SiMe_3)$•$THF_{0.68}$ (0.750 g, 2.73 mmol, THF content determined by ^1H NMR) and 50 mL of hexane was added. The resulting yellow-orange mixture was stirred overnight at room temperature following which it was filtered. The solvent from the filtrate was removed under vacuum, resulting in the formation of a yellow-orange waxy solid (1.168 g, 2.32 mmol, 85.5% yield). The crystals were grown from a saturated pentane solution at -40 °C. ^1H NMR (300 MHz, C_6D_6) δ: 1.715 (s, 30 H), 0.498 (s, 18H); $^{11}B\{^1H\}$ NMR (192 MHz, C_6D_6) δ: 100.368 (s); $^{13}C\{^1H\}$ NMR (150 MHz, C_6D_6) δ: 125.235 (m), 15.090 (m), 5.708 (s). HRMS (CI+) calcd for $C_{26}H_{48}BAsSi_2$ 502.2604, found 502.2592.

Methanolysis of $Cp^*_2BAs(SiMe_3)_2$ (7)

In a 20 mL vial in a dry box, **7** (1.600 g, 3.19 mmol) was dissolved in hexane. Methanol (0.40 mL, 9.88 mmol) was added and the reaction mixture stirred overnight at room temperature. A red brown precipitate formed (approx. 10 mg), which was collected and rinsed three times with fresh solvent. The B:As mole ratio was found to be 1.00:1.39 and the material was contaminated with silicon to the extent of 10.92% by weight.

Metathetical Reaction of Na_3As with BCl_3

In a 250 mL Schlenk flask equipped with a reflux condenser, a 1*M* hexane solution of BCl_3 (3.48 mL, 3.48 mmol) was added to a toluene slurry of Na_3As (0.4554 g, 3.16 mmol). The solution was refluxed for 36 h following which the solvent was removed under reduced pressure. The solid was rinsed with water and ethanol and was subsequently dried overnight under vacuum at 60 °C (0.0829 g). The B:As mole ratio was found to be 1.00:0.90 and the material was contaminated with Na and Cl to the extent of 26.85% and 35.39% by weight, respectively. In a sealed, evacuated tube, a portion of the solid was annealed at 500 °C for 48 h, following which the B:As mole ratio was found to be 1.00:0.79 and the Na and Cl contamination was 11.26% and 7.76% by weight, respectively.

Metathetical Reaction of Na_3As with BBr_3

In a 250 mL Schlenk flask equipped with a reflux condenser, a toluene solution of BBr_3 (0.783 g, 3.13 mmol) was added to a toluene slurry of Na_3As (0.4500 g, 3.13 mmol). The solution was refluxed for 48 h following which the solvent was removed under reduced pressure. The solid was rinsed with water and ethanol and was subsequently dried overnight under vacuum at 60 °C (0.1495 g). The B:As mole ratio was found to be 1.00:0.40 and the material was contaminated with Na and Br to the

extent of 17.64% and 28.03% by weight, respectively. In a sealed, evacuated tube, a portion of the solid was annealed at 500 °C for 48 h, following which the B:As mole ratio was found to be 1.00:0.13 and the Na and Br contamination was 25.07% and 38.79% by weight, respectively.

X-RAY CRYSTALLOGRAPHIC DETAILS

Table A1.1: Crystal data and structure refinement for $Cp^*_2BAs(SiMe_3)_2$.

Identification code	shelxl	
Empirical formula	C26 H48 As B Si2	
Formula weight	502.55	
Temperature	153(2) K	
Wavelength	0.71069 Å	
Crystal system	monoclinic	
Space group	p21/c	
Unit cell dimensions	a = 17.104(5) Å	a= 90.000(5)°.
	b = 12.305(5) Å	b= 92.710(5)°.
	c = 26.959(5) Å	g = 90.000(5)°.
Volume	5668(3) $Å^3$	
Z	8	
Density (calculated)	1.178 Mg/m^3	
Absorption coefficient	1.295 mm^{-1}	
F(000)	2160	
Crystal size	0.3 x 0.1 x 0.1 mm^3	
Theta range for data collection	1.19 to 27.47°.	
Index ranges	-22<=h<=22, -14<=k<=15, -34<=l<=34	
Reflections collected	23686	
Independent reflections	12933 [R(int) = 0.0371]	
Completeness to theta = 27.47°	99.7 %	
Refinement method	Full-matrix least-squares on F^2	
Data / restraints / parameters	12933 / 0 / 567	
Goodness-of-fit on F^2	1.032	
Final R indices [I>2sigma(I)]	R1 = 0.0456, wR2 = 0.0984	
R indices (all data)	R1 = 0.0847, wR2 = 0.1138	
Largest diff. peak and hole	1.802 and -0.368 e.$Å^{-3}$	

Table A1.2: Selected bond lengths for $Cp^*_2BAs(SiMe_3)_2$.

As(1)-B(1)	2.050(3)	C(8)-C(9)	1.534(3)
As(1)-Si(1)	2.3547(9)	C(8)-C(19)	1.588(3)
As(1)-Si(2)	2.3572(9)	C(9)-C(10)	1.335(3)
Si(1)-C(1)	1.872(3)	C(10)-C(11)	1.522(4)
Si(1)-C(2)	1.874(3)	C(11)-C(18)	1.573(3)
Si(1)-C(3)	1.875(3)	C(17)-B(1)	1.588(4)
Si(2)-C(4)	1.872(3)	C(17)-C(18)	1.563(3)
Si(2)-C(5)	1.870(3)	C(17)-C(21)	1.533(3)
Si(2)-C(6)	1.870(3)	C(18)-C(19)	1.587(3)
C(7)-B(1)	1.597(4)	C(19)-C(20)	1.518(3)
C(7)-C(8)	1.576(3)	C(20)-C(21)	1.328(3)
C(7)-C(11)	1.568(3)		

Table A1.3: Selected bond angles for $Cp^*_2BAs(SiMe_3)_2$.

C(7)-B(1)-As(1)	133.59(18)
C(17)-B(1)-As(1)	119.96(18)
C(17)-B(1)-C(7)	106.4(2)
B(1)-As(1)-Si(1)	112.13(8)
B(1)-As(1)-Si(2)	105.43(8)
Si(1)-As(1)-Si(2)	101.44(3)

Chapter 2: The Synthesis, Characterization and Photoelectrochemistry of Boron Arsenide

PREVIOUS SYNTHESES OF BORON ARSENIDE

Various approaches to the synthesis of BAs starting from the elements were reported several decades ago. For example, heating equimolar quantities of boron and arsenic in a sealed, evacuated quartz tube at 800 °C resulted in the formation of a cubic form of BAs with an unspecified stoichiometry.[54] A previously unknown orthorhombic phase, subsequently identified as boron subarsenide ($B_{12}As_2$), was described in the same report. The latter compound was formed by evaporation of arsenic from cubic BAs at temperatures greater than 920 °C. This orthorhombic phase was found to be unusually stable and showed no evidence of reaction when boiled in alkali solution, concentrated nitric acid, or concentrated hydrofluoric acid.

In a subsequent synthetic approach, elemental boron and arsenic were located at opposite ends of an evacuated sealed silica tube.[55] The two ends of the vessel were designed to be heated independently. For example, with boron heated to 700-800 °C and arsenic pressures in excess of 1 atm, a cubic material was isolated with a boron-to-arsenic mole ratio close to unity. On the other hand, with a boron temperature of 1000-1100 °C and arsenic pressures less than 1 atm, orthorhombic compounds with boron-to-arsenic mole ratios of 5-7 to 1 were isolated and corresponded to compositions in the range of $B_{6-7}As$. When treated with hot, concentrated nitric acid, the cubic BAs decomposed. Interestingly, however, the orthorhombic $B_{6-7}As$ material resisted attack.

The reaction of boron and arsenic at high temperatures in the range of 1200-1300 °C and high pressures of the order of 2-30 kbar afforded a mixture of cubic BAs and $B_{13}As_2$, reported this time as rhombohedral rather than orthorhombic.[56] Because hot,

concentrated nitric acid decomposed the cubic phase but not the rhombohedral phase, it was not possible to isolate the cubic BAs from the rhombohedral $B_{13}As_2$ phase. However, conditions were found such that cubic BAs could be formed without the formation of $B_{13}As_2$. This was achieved by employing a boron-to-arsenic mole ratio of 1 to 2-2.5, a reaction temperature of 1200 °C and a pressure of 4-5 kbar.[57] In the absence of $B_{13}As_2$, BAs can be readily isolated from unreacted excess arsenic by treatment with 4.5 N nitric acid at 85 °C, under which conditions oxidative attack of arsenic takes place preferentially.

Both BAs and $B_{12}As_2$ have been prepared along with an estimation of the respective band gaps.[58] The syntheses were carried out in sealed silica tubes with boron at one end and an excess of arsenic at the other. The boron end of the tube was maintained at temperatures between 850 and 1100 °C and the arsenic side was retained at 640 °C in order to provide 1 atm of arsenic vapor for the reaction. Cubic BAs was formed at reaction temperatures near 875 °C, while the use of temperatures greater than 1000 °C resulted in the formation of rhombohedral $B_{12}As_2$. Transmission *vs*. wavelength measurements were taken in order to measure the band gaps of each material, which were estimated to be 1.46 eV for BAs and 1.51 eV for $B_{12}As_2$. It was noted that the latter value may be significantly less than that of the actual band gap due to significant contamination of the samples. This report also included an attempt to prepare BAs via the reaction of aluminum arsenide and boron triiodide. However, products of this reaction were found to comprise both BAs and $B_{12}As_2$, along with aluminum arsenide, aluminum silicate, and other unidentified compounds. The latter mixture, which was less than 1 μm thick, was deposited on the tube walls in layers of various colors. Further product characterization was not attempted.

Cubic BAs crystals have been formed via chemical vapor transport using iodine as the transporting reagent.[59,60] This was accomplished by sealing a mixture of polycrystalline BAs, excess arsenic and iodine in one end of a quartz tube that was subsequently placed in a two-temperature furnace. The system was arranged such that the materials were heated to 900 °C while the temperature at the cooler end of the tube was allowed to decrease slowly from 890 °C to 850 °C. It was found that a crop of single crystals of BAs gradually formed over a period of two months. Moreover films of BAs on silicon carbide and silicon substrates could be formed from a mixture of arsine and diborane in hydrogen gas.[61] Optical absorption measurements of these materials were made and indicated that these films have a direct band gap of 1.45 eV. A search of the literature revealed that this is the only reference in which a direct band gap is claimed for BAs, rather than an indirect band gap in the range of 1.1 to 1.6 eV. However, it should be pointed out that the 1.45 eV direct band gap for BAs was reported almost four decades ago and this value has not been confirmed subsequently.

RESULTS AND DISCUSSION

Synthesis, Structure, and Surface Analysis of Boron Arsenide

In the present work, BAs was prepared via the reaction of boron powder with an excess of elemental arsenic in sealed, evacuated quartz tubes that were heated to 800 °C for 12 hours.[62] Initially, the reaction of equimolar quantities of these elements was attempted. On the basis of XPS analysis of the surface composition, this reaction was found to result in the formation of a material that is deficient in arsenic. The experimental value for the boron-to-arsenic mole ratio was found to be 1.00:0.569. As a consequence, it became necessary to undertake a series of experiments in which the boron-to-arsenic mole ratios of the starting materials were systematically varied. The

results of those experiments are presented in Table 2.1 from which it is clear that it is necessary to employ a boron-to-arsenic ratio of 1.00:1.90 to produce a material with the desired stoichiometry. The pertinent boron 1s and arsenic 3d XPS peaks for the product of reaction 4 are displayed in Figure 2.1. Table 2.2 provides the corresponding XPS quantification data. XPS spectra and quantification data for reactions 1-3 and 5 are displayed in Figures A2.1-A2.4 and Tables A2.1-A2.4.

Table 2.1: Molar equivalents of arsenic used for the synthesis of BAs.

$B + xAs \rightarrow BAs_y$		
Reaction number	Reactant (x)	Product[a] (y)
1	1.00	0.569
2	1.22	0.753
3	1.44	0.794
4	1.90	0.993
5	2.54	1.213

[a]based on XPS data.

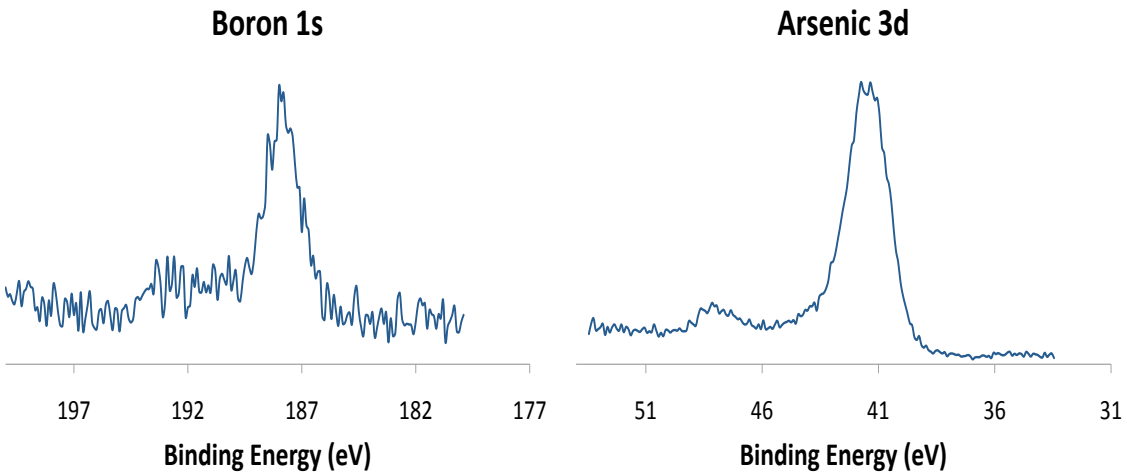

Figure 2.1: High-resolution XPS spectra of the BAs prepared from boron powder and 1.90 molar equivalents of arsenic.

Table 2.2: XPS quantification data for BAs prepared from boron powder and 1.90 molar equivalents of arsenic.

Peak	Position (eV)	R.S.F.	Area	Atomic % Conc.
B 1s	187.91	0.159	891.89	50.18
As 3d	41.26	0.677	3770.46	49.82

The structure of the new material was identified on the basis of XRD.[62] A representative XRD pattern is displayed in Figure 2.2 and is clearly a good match to that of the cubic BAs pattern found in literature.[57] The product is stable to air, water and temperatures of at least 200 °C. Samples subjected to air, water and heat displayed XRD patterns that were undistinguishable from that of the freshly prepared material. The pertinent patterns are displayed in Figure 2.3. The products of reactions 1-5 were accompanied by crystals that were identified as elemental arsenic. Treatment of the products with hot nitric acid could remove these crystals. However, it was found that the resulting product exhibited a diminished photocurrent. Accordingly, it was necessary to

remove the excess arsenic manually. The XRD pattern of the manually removed crystals confirmed their identity to be that of elemental arsenic as shown in Figure 2.4.

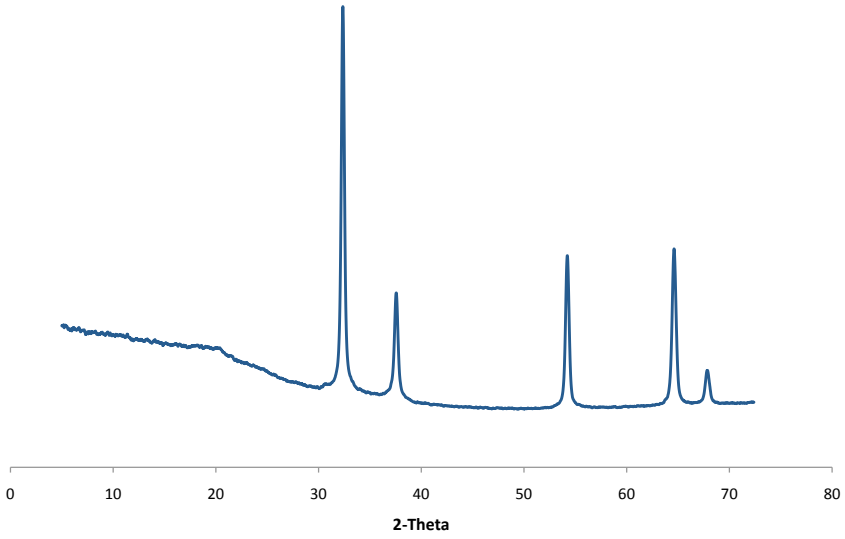

Figure 2.2: XRD data for BAs prepared from boron powder.

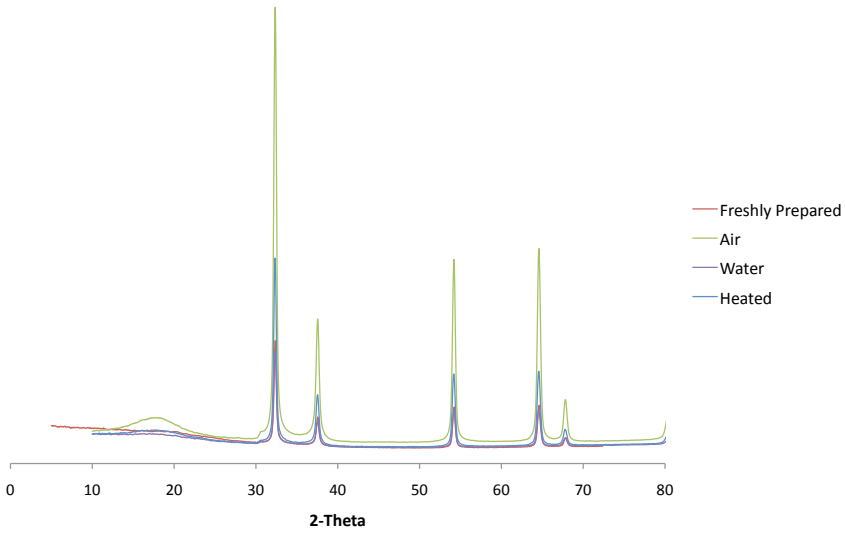

Figure 2.3: XRD data for BAs samples exposed to air, water, and a temperature of 200 °C. Each pattern is unaltered from that of the freshly prepared sample.

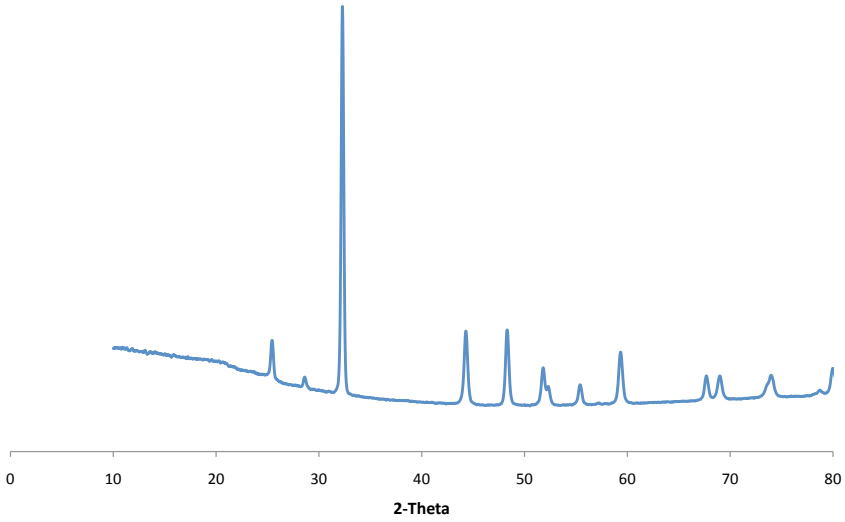

Figure 2.4: XRD data for crystals identified as elemental arsenic.

Due to the difficulty in preparing a BAs electrode from a powder sample, granular boron ranging in size from 0.42 to 4.75 mm was treated with 2 molar equivalents of arsenic in sealed, evacuated quartz tubes that were heated to 800 °C for 3 days.[62] At the conclusion of the heat treatment, the excess arsenic was removed manually. Scanning electron microscopy (SEM) was used to examine the structure of the product. The SEM images revealed that an interesting surface reaction had taken place, resulting in the deposition of a thin layer of BAs on top of the boron substrate. The BAs surface layer was not continuous and revealed gaps where the boron core was clearly visible. Displayed in Figure 2.5 are SEM images showing a single piece of the BAs material, areas of continuous BAs coverage and areas where the boron core is clearly visible.

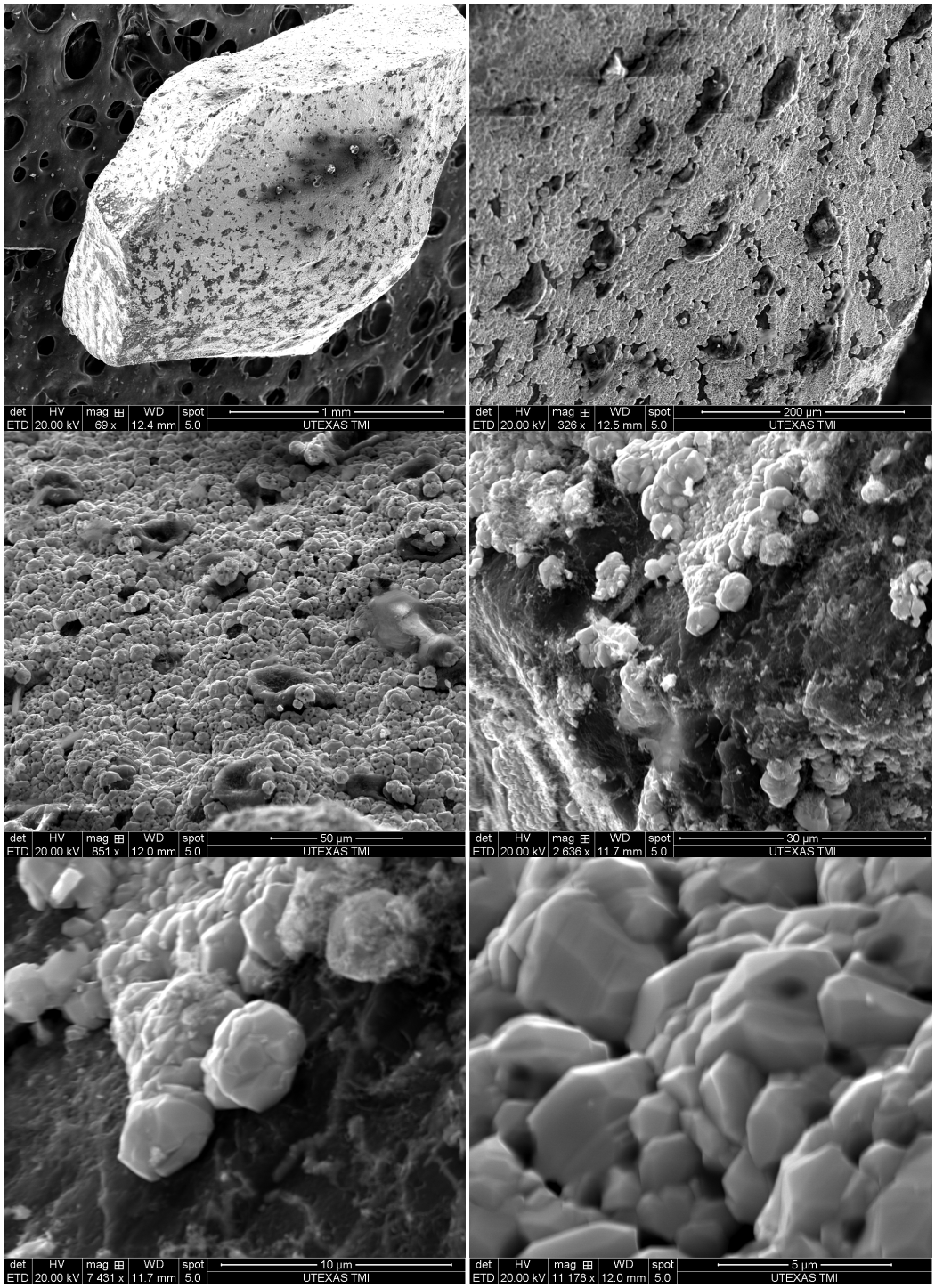

Figure 2.5: SEM images reveal the surface layer and core structure of the BAs material prepared from granular boron.

As shown in Figure 2.6, the presence of polycrystalline BAs and elemental boron was established on the basis of XRD data taken from a single piece of the material.[62] These data support the surface layer and core structure indicated by the SEM images, displayed in Figure 2.5.

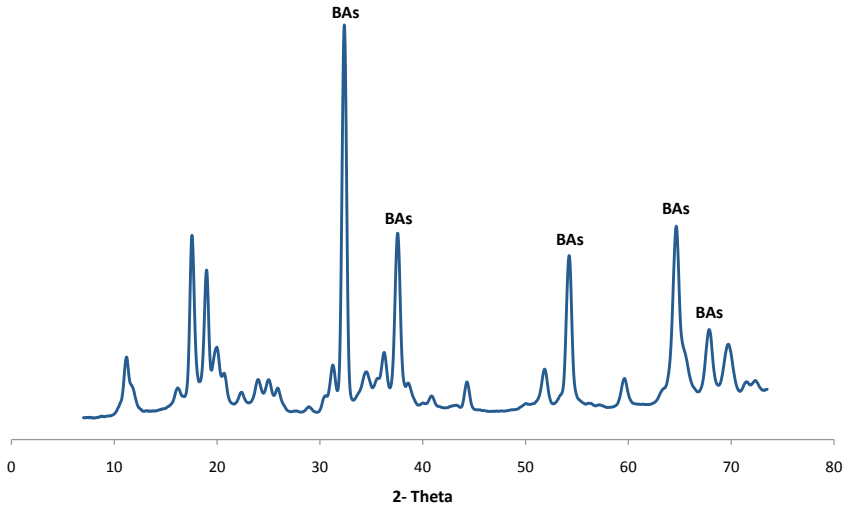

Figure 2.6: XRD data confirm the presence of both BAs and elemental boron in a single piece of the material prepared from granular boron. The peaks without labels are attributable to elemental boron.

An XPS analysis was performed in order to determine the chemical composition of the new BAs material.[62] The pertinent boron 1s and arsenic 3d peaks are displayed in Figure 2.7 and the quantification data are displayed in Table 2.3. Unfortunately due to exposure of the boron core, it was not possible to determine a reliable mole ratio for the BAs surface layer of the new material. However, the high-resolution XPS spectra revealed a mole ratio of boron and arsenic close to unity, thus indicating broad coverage of the boron core by the BAs surface layer. The major peak in the boron 1s XPS spectrum is close to that of boron nitride (189.7-190.4 eV).[63] Moreover, the major peak

in the arsenic 3d spectrum at 41.76 eV is very close to the range 40.5-41.2 eV reported for other Group III arsenides and the low intensity peak at 43-46 eV is characteristic of an arsenic oxide.[64] Finally an XPS analysis of the boron starting material revealed the presence of oxygen, thus suggesting that the starting material was a possible source for the oxide contamination.

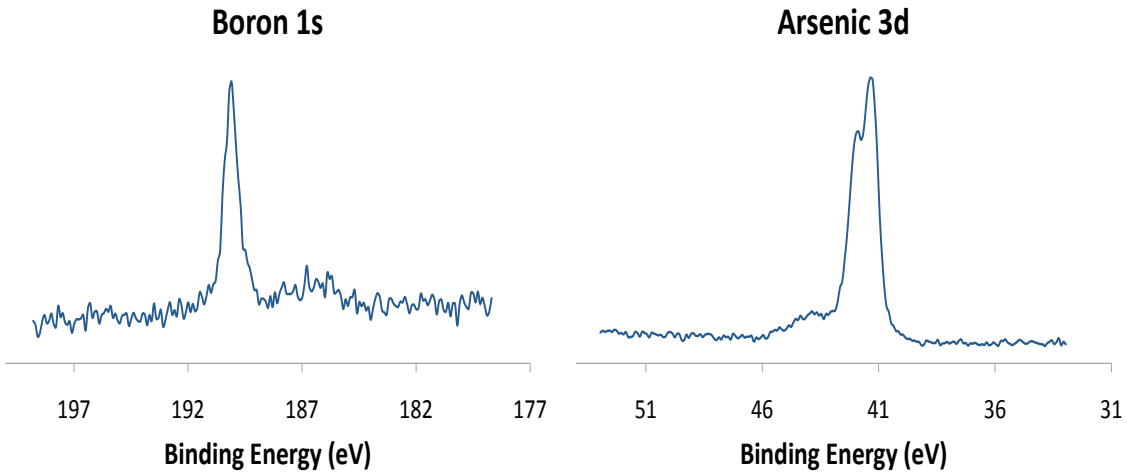

Figure 2.7: High-resolution XPS spectra of the BAs material prepared from granular boron.

Table 2.3: XPS quantification data for BAs prepared from granular boron.

Peak	Position (eV)	R.S.F.	Area	Atomic % Conc.
B 1s	188.51	0.159	929.62	50.27
As 3d	41.76	0.677	3915.91	49.73

Photoelectrochemistry of Boron Arsenide

A gold layer with a thickness of approximately 200 nm was deposited on one side of a single piece of the BAs material prepared from granular boron, the size of which was approximately 3 mm.[62] The gold deposition was accomplished by means of a commercial gold alloy electroplating solution (SG-50, Transene Co., Inc., Rowley, MA)

in a two-electrode system by applying a potential of -1.0 V at BAs relative to that of the counter electrode. A silver epoxy paste was used to connect a copper wire to the gold layer. The copper wire and the silver epoxy paste were then covered with silicone cement, resulting in a BAs electrode with an active surface area of 1 mm^2. A typical BAs photoelectrode is displayed in Figure 2.8.

Figure 2.8: A typical boron arsenide electrode.

Photocurrent Determination

The electrode was found to be photoactive under both visible light ($\lambda > 420$ nm) and UV-visible (Xe lamp) irradiation, as demonstrated by the linear sweep voltammograms (LSVs) displayed in Figure 2.9.[62] The LSVs spanned a potential range of 0.0 to -0.5 V *vs*. Ag/AgCl at a scan rate of 20 mV/s. The incident light intensity at the electrode surface was 100 mW/cm^2 using a 150 W Xe lamp. The voltammetric measurements, which were carried out in a 0.1 *M* aqueous Na_2SO_4 solution containing 0.01 *M* methyl viologen, showed a cathodic photocurrent attributable to the reduction of methyl viologen, thereby indicating p-type behavior. The response to continuous visible light and UV-visible irradiation is shown in Figure 2.9A. Figures 2.9B and 2.9C display the corresponding LSVs of the BAs photoelectrode using chopped visible light and UV-visible irradiation, respectively. This was accomplished by revealing and hiding the irradiation from the electrode in cycles as the potential was swept.

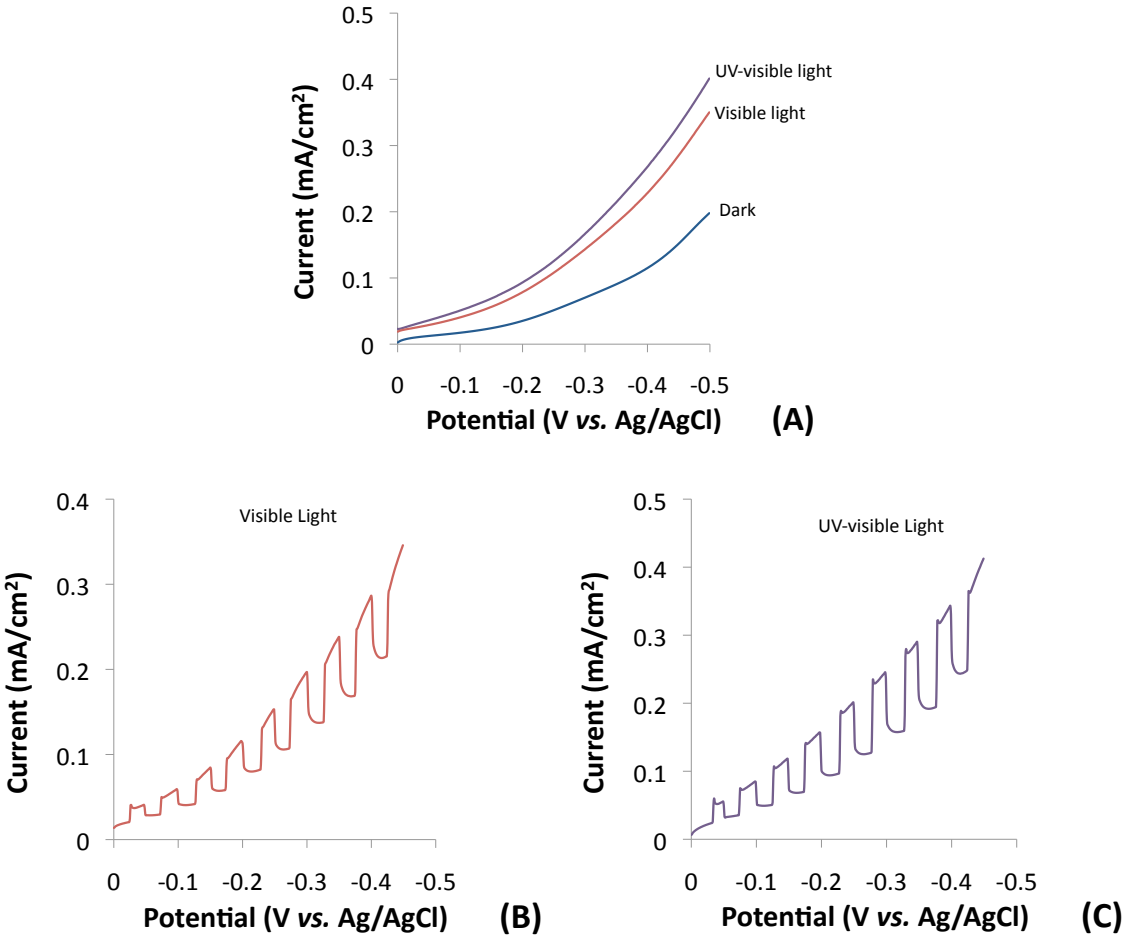

Figure 2.9: LSVs for the BAs material in a 0.1 *M* aqueous Na_2SO_4 solution containing 0.01 *M* methyl viologen. The potential was swept from 0.0 to -0.5 V *vs*. Ag/AgCl at a scan rate of 20 mV/s. The incident light intensity at the electrode surface was 100 mW/cm^2 using a 150 W Xe lamp. (A) Current flow in the dark, under visible light, and UV-vis irradiation. (B) Current flow for the BAs material under chopped visible light irradiation. (C) Current flow for the BAs material under chopped UV-vis irradiation.

The origin of the dark current from the BAs material is still not clear and merits further investigation.[62] It is possible that there may be a thin layer of boron doped with arsenic at the interface of the boron arsenide surface layer and the boron core. An arsenic-doped boron electrode was prepared by treating granular boron with a very small amount of arsenic (0.06 equivalents) in a sealed, evacuated quartz tube for 2 hours at 800

°C. This arsenic-doped boron electrode exhibited a dark current as shown in Figure 2.10. However, no photocurrent was detected with this electrode under the conditions described in Figure 8, indicating that arsenic-doped boron may be the source of the dark current in the LSVs of the BAs material.

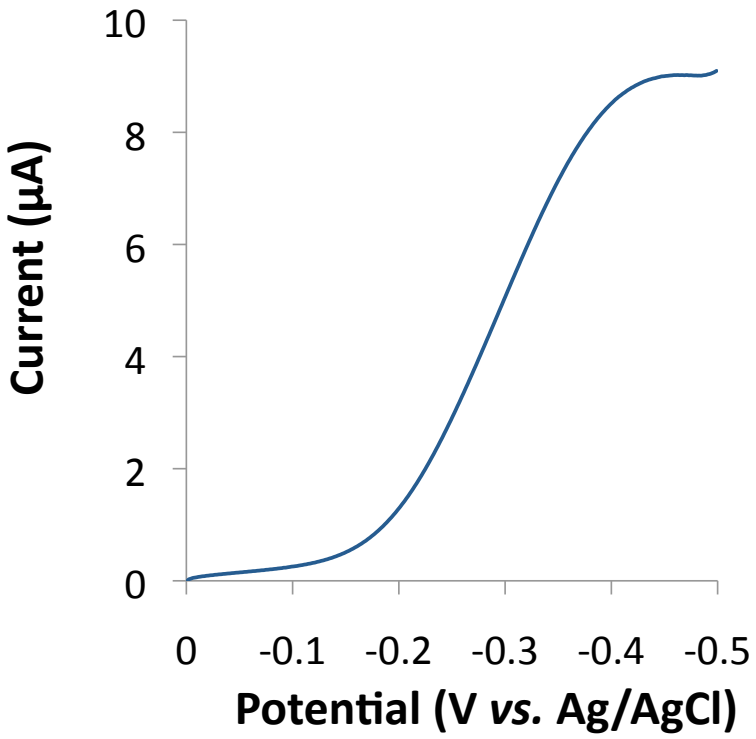

Figure 2.10: LSV of an arsenic-doped boron electrode in the dark in a 0.1 *M* aqueous Na_2SO_4 solution containing 0.01 *M* methyl viologen. The potential was swept from 0.0 to -0.5 V *vs*. Ag/AgCl at a scan rate of 20 mV/s.

The dark current was subtracted from the LSVs of the BAs photoelectrode under chopped visible light and UV-visible irradiation (Figures 2.9B and 2.9C) so that the net photocurrent could be measured.[62] These new LSVs are displayed in Figure 2.11. The net photocurrent was approximately 0.1 mA/cm^2 under full Xe lamp irradiation at an

applied potential of -0.25 V *vs*. Ag/AgCl in a 0.1 *M* aqueous Na_2SO_4 solution containing 0.01 *M* methyl viologen, as shown in Figure 2.12.

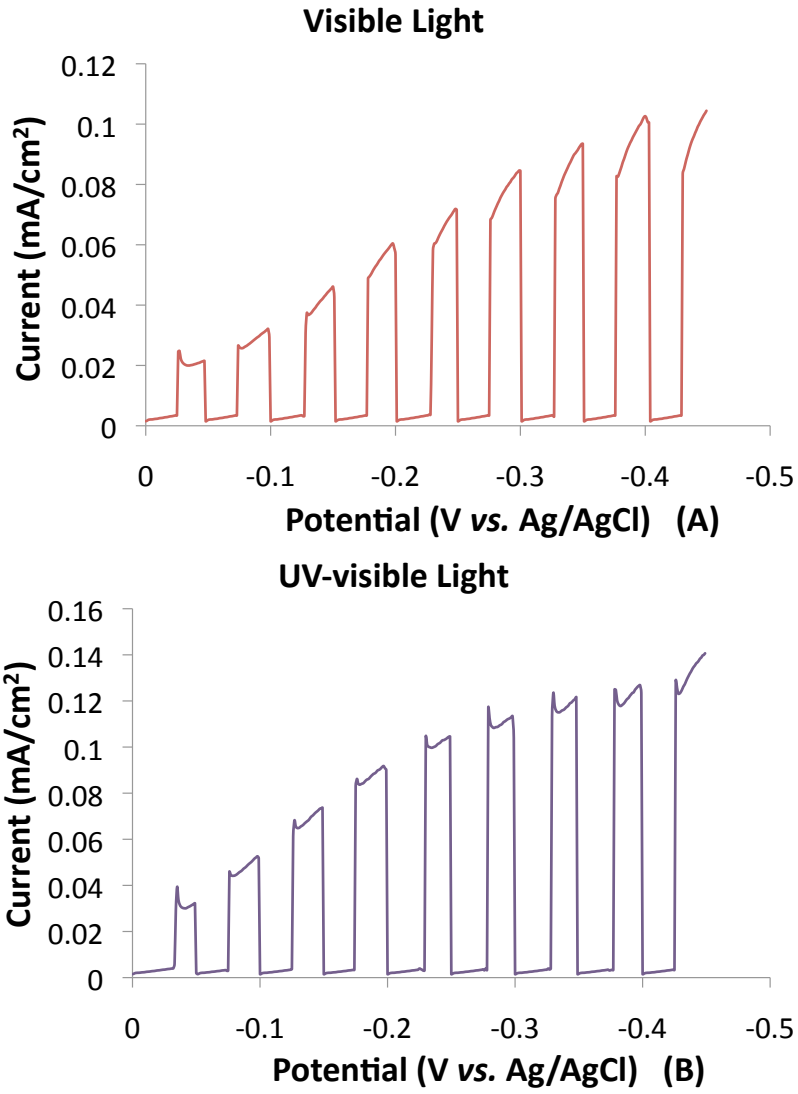

Figure 2.11: LSVs after subtraction of the dark current in a 0.1 *M* aqueous Na_2SO_4 solution containing 0.01 *M* methyl viologen. The potential was swept from 0.0 to -0.5 V *vs*. Ag/AgCl at a scan rate of 20 mV/s. The incident light intensity at the electrode surface was 100 mW/cm^2 using a 150 W Xe lamp. (A) Net photocurrent for the BAs material under chopped visible light irradiation. (B) Net photocurrent for the BAs material under chopped UV-visible light irradiation.

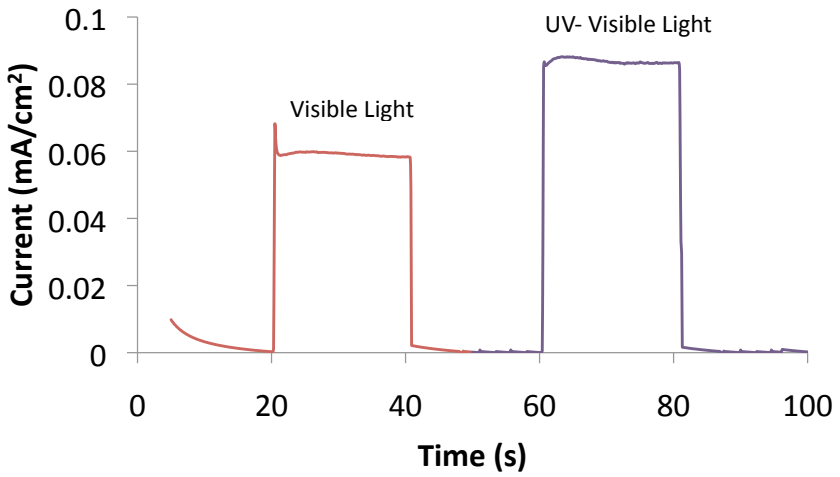

Figure 2.12: Current at an applied potential of -0.25 V *vs*. Ag/AgCl in the dark (0-20 s, 40-60 s, and 80-100 s), under visible light irradiation (20-40 s), and under UV-visible light irradiation (60-80 s) in a 0.1 *M* aqueous Na_2SO_4 solution containing 0.01 *M* methyl viologen.

Valence Band Position

To find the position of the valence band of boron arsenide, the flatband potential was explored.[62] In a semiconductor, the energy level at which the probability of occupation by an electron is one half is called the Fermi level. In a p-type material, the Fermi level lies just above the valence band. When the Fermi level equals the solution redox potential of an electrochemical cell, the cell is at the flatband potential. The flatband potential is therefore a good estimate of the valence band in a p-type material. Mott-Schottky plots are used to find the flatband potential of a material by plotting capacitance vs. potential; the flatband is found where capacitance is zero. The Mott-Schottky plots displayed in Figure 2.13 were obtained for this BAs electrode in the potential range of 200 Hz to 1000 Hz in the dark in a 0.1 *M* aqueous Na_2SO_4 solution containing 0.01 *M* methyl viologen. Although there was a significant shift in the plots

with frequency, the estimated flatband potential appears to be approximately 0.5 V *vs*. Ag/AgCl. Mott-Schottky plots are best applied to smooth, uniform films. For this reason, the flatband potential was also estimated by measuring the onset photopotential. An LSV under chopped UV-visible light irradiation spanning the potential range of 0.45 to -0.4 V *vs*. Ag/AgCl, displayed in Figure 2.14, revealed that the onset photopotential of the p-type BAs electrode is approximately 0.35 V *vs*. Ag/AgCl, or -5.1 eV *vs*. vacuum.

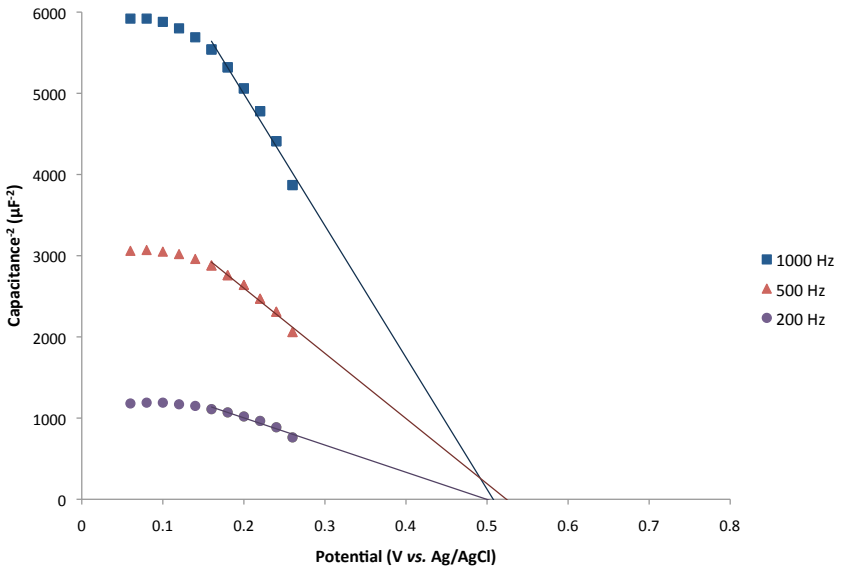

Figure 2.13: Mott-Schottky plots at three different frequencies (circles: 200 Hz, triangles: 500 Hz, squares: 1000 Hz) of the BAs electrode in the dark immersed in a 0.1 *M* aqueous Na_2SO_4 solution containing 0.01 *M* methyl viologen. The AC modulation amplitude was 10 mV peak-to-peak.

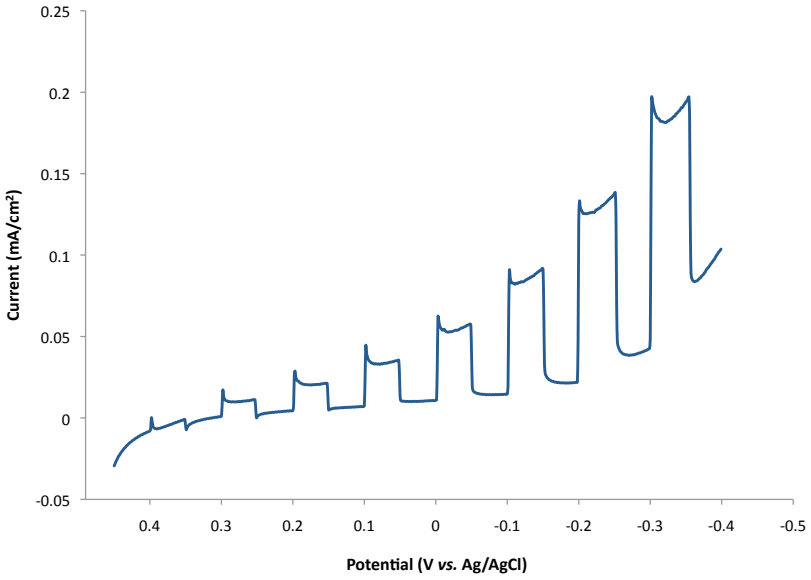

Figure 2.14: Overall current of the BAs photoelectrode in a 0.1 *M* aqueous Na_2SO_4 solution containing 0.01 *M* methyl viologen under chopped UV-visible irradiation. The incident power at the electrode surface was 100 mW/cm^2 using a 150 W Xe lamp. The potential was swept from 0.45 to -0.4 V *vs*. Ag/AgCl.

Band Gap Determination

The photocurrent for the BAs photoelectrode was measured as a function of wavelength over the range 350 to 850 nm in a 0.1 *M* Na_2SO_4 aqueous solution containing 0.01 *M* methyl viologen using a 150 W Xe lamp and a monochromator.[62] The incident photon-to-electron conversion efficiencies (IPCEs) were calculated using the following equation:

$$IPCE = 1240\left(\frac{i_{ph}}{\lambda P_{in}}\right) x\ 100\%$$

In this equation, i_{ph} is the net photocurrent in mA measured at -0.25 V *vs*. Ag/AgCl, λ is the wavelength in nm, and P_{in} represents the incident light intensity in mW at the surface

of the semiconductor electrode. The units of 1240 are W nm A^{-1} and it represents hc e^{-1} where h is the Planck constant, c is the speed of light in vacuum, and e is the elementary charge. The IPCE plot is displayed in Figure 2.15. The calculated IPCE reached approximately 5% at 400 nm for the BAs photoelectrode and decreased with increasing wavelength, reaching zero at approximately 850 nm. As a consequence, the estimated band gap[65,66] is 1.46 eV, which agrees well with the literature values[58,61] and values derived from theoretical calculations.[3,7,8]

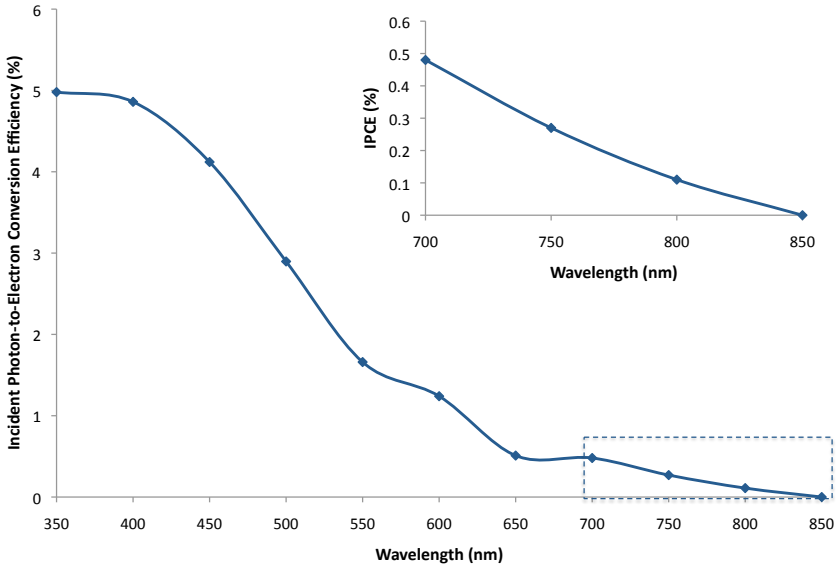

Figure 2.15: IPCE for the BAs photoelectrode calculated from the net photocurrent at -0.25 V *vs*. Ag/AgCl in a 0.1 *M* aqueous Na_2SO_4 solution containing 0.01 *M* methyl viologen. The incident light intensity at the electrode surface was 100 mW/cm^2 using a 150 W Xe lamp. The inset shows the marked box on an expanded scale.

For an indirect band gap material, a plot of $(\eta h\nu)^{1/2}$ *vs*. $h\nu$ should be linear. Here, η is the external quantum efficiency and is equal to the IPCE and $h\nu$ is the photon energy. The intercept on the energy axis gives the band gap. Figure 2.16 displays this plot for the

BAs photoelectrode over the energy range of interest, indicating that BAs is an indirect band gap material and confirming the estimated band gap of 1.46 eV.

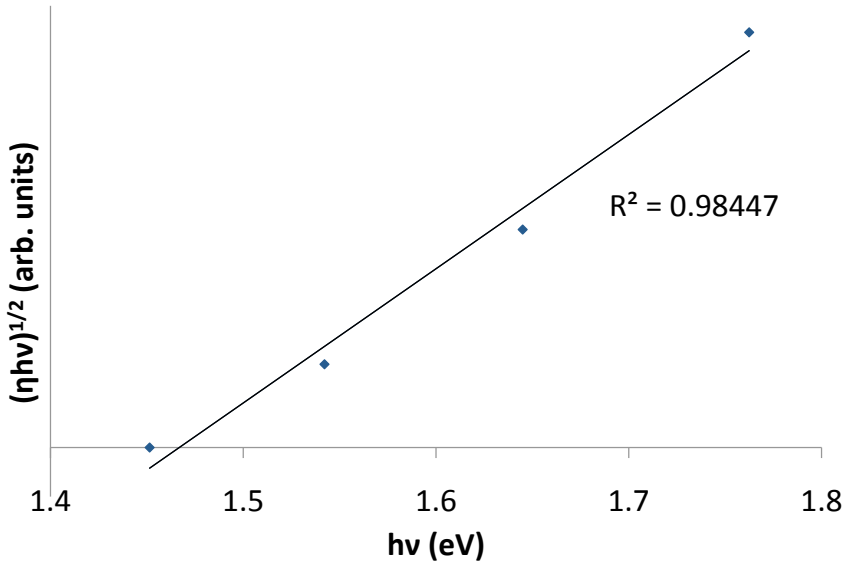

Figure 2.16: $(\eta h\nu)^{1/2}$ *vs*. $h\nu$ for the BAs photoelectrode.

CONCLUSIONS

The BAs photoelectrode prepared in the present work displayed p-type behavior and, with an experimental indirect band gap of 1.46 eV, is active under both visible and UV-visible light irradiation. It has a photocurrent of approximately 0.1 mA/cm^2, however, there are still many ways to optimize this material. The valence band lies at approximately -5.1 eV. The research presented here is very fundamental and it is possible that, with these first steps, boron arsenide may one day find some niche applications.

This simple, solid state method to the boron arsenide system was recently featured as an Angewandte Highlight.[67] The simplicity of our synthesis and electrode preparation, despite the complication arising from the possibility of multiple stoichiometries, makes

this approach important because standard photovoltaic devices are currently not cost-effective or viable without government subsidies. Our method involves standard chemistry and photoelectrochemical technologies only, as opposed to single-crystal growth, semiconductor processes, and cleanroom procedures. The SEM images alone show successful semiconductor nanostructure synthesis, as indicated by the contrast of black boron and white boron arsenide. Commercial photovoltaic cells with efficiencies up to 18% on the device level are available, however, single-crystalline or polycrystalline silicon used in these cells is expensive. Additionally, energy generated from these photovoltaic devices is difficult to store and transport over long times and distances. Our system of chemically processed electrodes can be stored and transported in an easier manner. Though our system is not suited for water splitting due to a band gap that is too small and band positions that are not suitable, it is a small step in progress toward solving our energy problem. New developments are often made in several small steps, solving problems as they arise.

EXPERIMENTAL DETAILS

General Methods

All syntheses were performed under a dry, oxygen-free argon atmosphere or vacuum using standard Schlenk line and dry box techniques. Quartz tubes were dried at least 24 h in a 120 °C oven prior to use. Boron powder (powder, amorphous and crystalline, -325 mesh, 99%), granular boron (powder, crystalline, -4+40 mesh, 99.999%), and arsenic (polycrystalline lump, 2-8 mm, puratronic, 99.9999%) were purchased from Alfa Aesar and used without further purification.

Instruments

X-ray Photoelectron Spectroscopy

The XPS spectra were recorded on a Kratos Axis Ultra X-ray photoelectron spectrometer utilizing a monochromated Al Kα X-ray source. All spectra were collected with a pass energy of 20 eV. CasaXPS software version 2.3.16 was used to determine the stoichiometries of the samples from the corrected peak areas by applying the relative sensitivity factors of 0.159 and 0.677 for B 1s and As 3d, respectively.

X-ray Powder Diffraction

The data were collected on a Rigaku R-Axis Spider diffractometer with an image plate detector using a graphite monochromator and Cu Kα radiation (λ = 1.5418 Å). The instrument was controlled using Rapid/XRD Version 2.3.8 diffractometer control software from Rigaku Americas Corporation, The Woodlands, TX. The integration of the two dimensional data into a one dimensional pattern was accomplished using 2DP Version 1.0 from Rigaku Americas Corporation, The Woodlands, TX.

Scanning Electron Microscopy

The SEM images were acquired on a Quanta FEG 650 instrument.

Synthesis of Materials

Preparation of BAs from boron powder

Boron powder (0.0218 g, 2.02 mmol) and arsenic (0.2864 g, 3.82 mmol) were ground together in a mortar and pestle and then loaded into a quartz tube of approximately 4 mL volume. The tube was evacuated and sealed and subsequently heated to 800 °C for 12 h. Subsequent to the heat treatment, the excess arsenic was removed manually.

Preparation of BAs from granular boron

Granular boron (0.0588 g, 5.44 mmol) and arsenic (0.8000 g, 10.68 mmol) were loaded into a quartz tube of approximately 4 mL volume. The tube was evacuated and sealed and subsequently heated to 800 °C for 3 d. At the conclusion of the heat treatment, the excess arsenic was removed manually.

Preparation of As-doped boron

Granular boron (0.0583 g, 5.39 mmol) and arsenic (0.0240 g, 0.32 mmol) were loaded into a quartz tube of approximately 4 mL volume. The tube was evacuated, sealed and subsequently heated to 800 °C for 2 h.

XPS SPECTRA AND QUANTIFICATION DATA

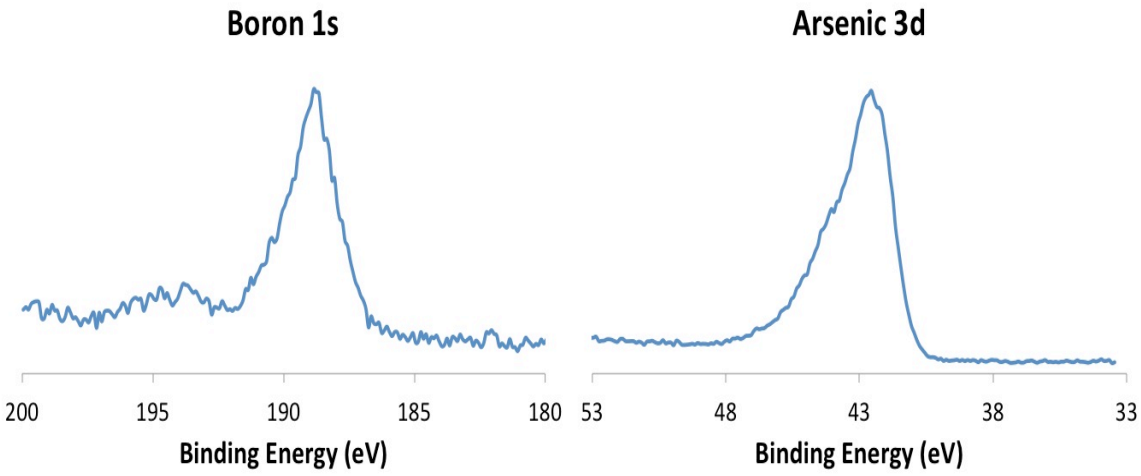

Figure A2.1: High-resolution XPS spectra of the BAs prepared from boron powder and 1.00 molar equivalent of arsenic.

Table A2.1: XPS quantification data for BAs prepared from boron powder and 1.00 molar equivalent of arsenic.

Peak	Position (eV)	R.S.F.	Area	Atomic % Conc.
B 1s	186.80	0.159	2171.1	63.74
As 3d	40.35	0.677	5099.5	36.26

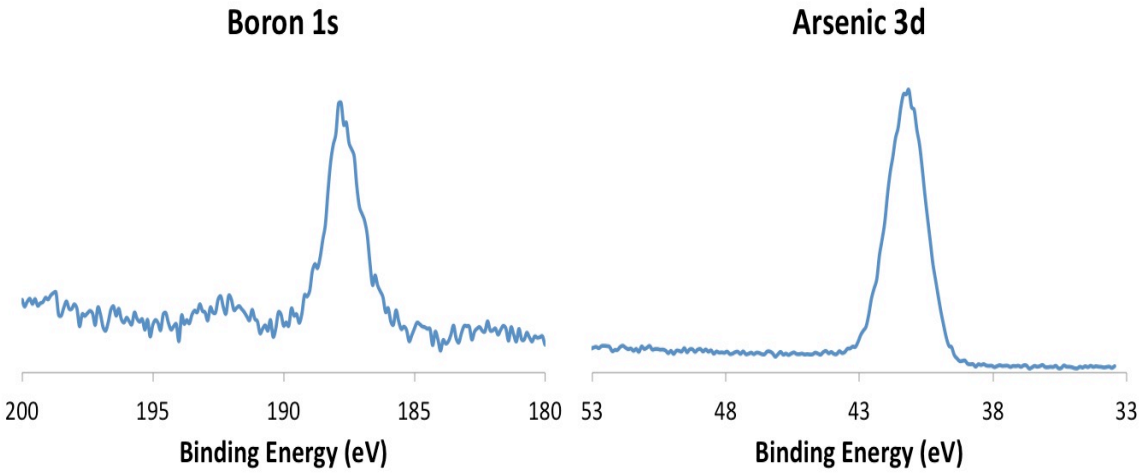

Figure A2.2: High-resolution XPS spectra of the BAs prepared from boron powder and 1.22 molar equivalents of arsenic.

Table A2.2: XPS quantification data for BAs prepared from boron powder and 1.22 molar equivalents of arsenic.

Peak	Position (eV)	R.S.F.	Area	Atomic % Conc.
B 1s	187.80	0.159	1850.5	57.05
As 3d	41.15	0.677	5751.1	42.95

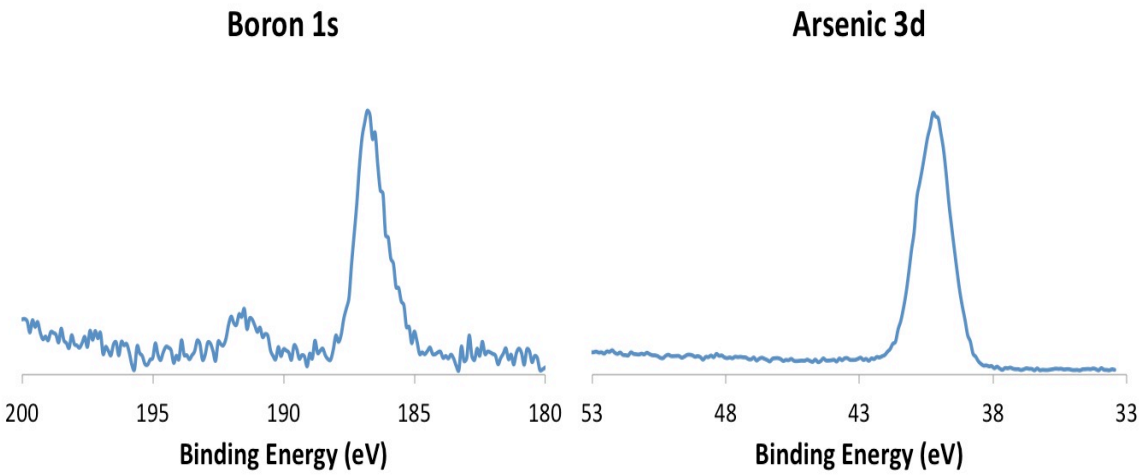

Figure A2.3: High-resolution XPS spectra of the BAs prepared from boron powder and 1.44 molar equivalents of arsenic.

Table A2.3: XPS quantification data for BAs prepared from boron powder and 1.44 molar equivalents of arsenic.

Peak	Position (eV)	R.S.F.	Area	Atomic % Conc.
B 1s	186.80	0.159	1678.2	55.75
As 3d	40.25	0.677	5500.9	44.25

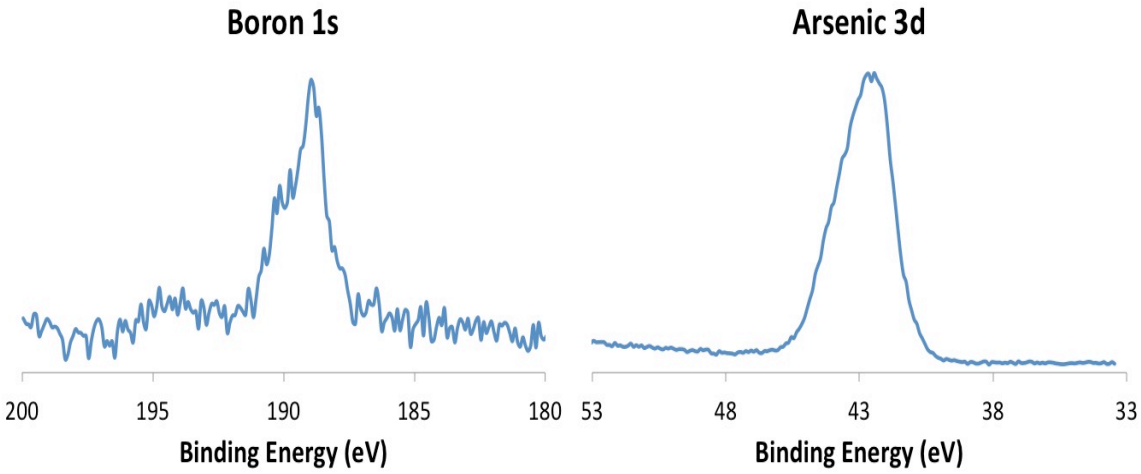

Figure A2.4: High-resolution XPS spectra of the BAs prepared from boron powder and 2.54 molar equivalents of arsenic.

Table A2.4: XPS quantification data for BAs prepared from boron powder and 2.54 molar equivalents of arsenic.

Peak	Position (eV)	R.S.F.	Area	Atomic % Conc.
B 1s	188.95	0.159	805.0	45.19
As 3d	42.45	0.677	4030.1	54.81

BLUE EMISSION FROM ALUMINUM COMPLEXES

Red and green luminescent materials and efficient organic light-emitting diodes (OLEDs) are much more readily available than the corresponding blue luminescent materials. OLEDs feature active emission, high brightness, a low driving voltage and wide viewing angles. Moreover, they are light weight and inexpensive.[68] Applications of OLEDs include full-color flat-panel displays and solid state lighting.[69] Luminophors that span the visible region are highly desirable. However, blue emitting OLEDs tend to have lower efficiencies than the corresponding red and green devices and often suffer from poor color purity and instability.[70]

Blue luminescent materials fall into three categories, namely inorganic semiconductors, organic polymers, and organic or organometallic molecules.[71] Inorganic semiconductors are expensive to make and often exhibit low efficiencies. Organic polymers have the advantage of facile formation of films that do not tend to crystallize.[72] However, devices made from organic polymers often display poor performance due to low stability and the presence of impurities. Organic or organometallic molecules offer several advantages in comparison with inorganic semiconductors and organic polymers, such as increased stability, affordability, and emission color tuning by chemical modification. Moreover, high-quality device fabrication can be achieved if the molecule is volatile and thus amenable to vacuum deposition.

The use of aluminum in metal complexes designed for blue luminescence is advantageous for three main reasons.[73] Firstly, the aluminum cation contains no *d* electrons and therefore will not alter the blue luminescence of a ligand. Secondly, the aluminum cation can adopt a wide range of coordination geometries, thus allowing it to accommodate a wide range of ligands. Lastly, the aluminum cation is a hard Lewis acid

that binds well to hard donor atoms such as nitrogen and oxygen.[74] Aluminum complexes have been found to be especially useful in the field of OLED chemistry due to their excellent emissive properties, high quantum yields and good color purity.[75]

The compounds used in OLEDs should be chemically and thermally stable, and ideally should sublime if gas-phase deposition is anticipated.[76] Additional important parameters for materials to be used in OLEDs include emission wavelength, emission efficiency and the energy levels of the HOMO and LUMO.[77] Moreover, in order to achieve an ideal mobility of charge carriers and efficient charge recombination, it is necessary to align the HOMO and LUMO energy levels of the emissive material with those of other device components. OLEDs are typically fabricated using two or more organic materials deposited as amorphous thin solid films between two electrodes. Usually one organic material functions as the electron-transporting layer and the other serves as the hole-transporting layer. The electrons from the cathode and the holes from the anode travel through the transporting layers to meet and thereby form an exciton, which causes population of the excited state of the emissive complex. This excited state then relaxes and emits electroluminescence.[78] Clearly, the orbital energy levels of the materials need to be considered carefully in order to achieve maximum efficiency.

Chapter 3: A Review of Blue Emission from Aluminum Complexes

The present chapter will focus on the photoluminescence of previously reported organometallic molecules containing aluminum, which are designed with the goal of producing blue emission. Particular emphasis is placed on the effect of chemical modification on emission and other photophysical properties. The present review will cover the pertinent literature from 1996 to 2012, starting with 8-hydroxyquinoline aluminum (AlQ_3) and its derivatives. It will then continue with aluminum complexes that are unrelated to the AlQ_3 system.

8-Hydroxyquinoline Aluminum and Derivatives

An electroluminescent device with vapor-deposited thin films of AlQ_3 used as the electron-transporting and emitting layers was first reported by Tang and Van Slyke in 1987.[79] The 8-hydroxyquinoline ligand and the AlQ_3 complex are shown in Figure 3.1. This device displayed green emission, a brightness of greater than 1000 cd m^{-2} and external quantum efficiencies of the order of 1%. Amorphous thin film formation is facile for AlQ_3 due to its rigid ball-like geometry, high glass transition temperature of 175 °C, and polymorphic nature.[80,81] Furthermore, AlQ_3 exhibits an electron mobility around 10^{-5} cm^2 V^{-1} s^{-1}.[82]

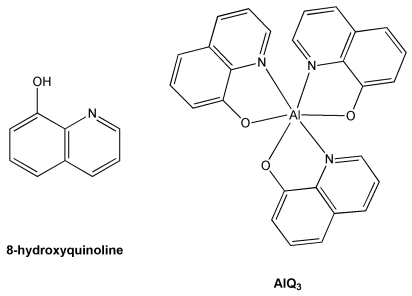

Figure 3.1: The 8-hydroxyquinoline ligand and the AlQ_3 complex.

Metalloquinolates are viable candidates for use as electroluminescent materials because they form stable thin films, exhibit good charge transport mobilities, and have satisfactory luminescence yields in the solid state.[83] Emission tuning is also possible by chemical modification of the ligand and by changing the coordination geometry at the metal center. However, some structurally modified AlQ_3 derivatives have been found to be less thermally stable and less volatile than AlQ_3, resulting in difficulty or failure in OLED fabrication.[84]

Uses for AlQ_3 have also been found in organic solar cell devices, in which a buffer layer of AlQ_3 effectively prevents cathode diffusion from the metal cathode to the organic layer.[85] AlQ_3 can also be used to increase device lifetime by protecting the device from oxygen and moisture penetration. Furthermore, increases in power conversion efficiency for organic photovoltaic cells have been observed when the donor or acceptor layers are doped with AlQ_3.[86]

The emissive properties of AlQ_3 are attributable to ligand-centered π-π^* transitions[87,88] and DFT calculations indicate that the HOMO is located on the phenoxide ring, specifically at the 5- and 8-positions, while the LUMO is located on the pyridyl side, specifically at the 2- and 4-positions.[89] The addition of electron-donating groups to the phenoxide ring should therefore destabilize the HOMO, resulting in a red-shift of the emission. On the other hand, the presence of electron-donating groups on the pyridyl side of the ligand should raise the energy level of the LUMO, thereby causing an emission blue-shift. The opposite effects should be observed when electron-withdrawing groups are used. For example, the placement of an electron-withdrawing group at the 5-position of the quinoline ring in AlQ_3 is predicted to increase the HOMO-LUMO energy gap.[90] While experimental studies show this to be generally true, there are some exceptions. For example, the addition of an electron-withdrawing cyano group at the 5-

position results in only a 4 nm blue-shift.[91] Contrary to expectation, appending a fluoro or chloro group to the 5-position results in red-shifted emission maxima.[92] The addition of an electron-donating methyl group onto the pyridyl ring will induce a blue-shift and the magnitude of the blue-shift is dependent on the position of the methyl group. The largest blue-shift occurs when the methyl group is in the 2-position.[82,92] However, due to steric effects, the tris(8-hydroxy-2-methylquinoline)aluminum complex is not stable, hence it is necessary to replace one quinoline with a smaller ligand, thereby creating a 5-coordinate complex.[93,94] The extent of the blue-shift when a methyl is introduced at the 2-position may therefore be due to the electronic effect of the methyl group or the change in geometry at the aluminum center.[95] The introduction of a heteroatom into the quinoline ring also effects emission wavelength. A nitrogen in the 4-position results in a 90 nm blue-shift whereas a nitrogen in the 5-position results in a 60 nm red-shift.[82]

Tris 8-Hydroxyquinoline Aluminum Derivatives

Two AlQ_3 derivatives, tris[5-(methyl-malononitrile)-8-hydroxyquinoline]aluminum ($Al(CNQ)_3$) and tris(2,3-dimethyl-8-hydroxyquinoline)aluminum ($Al(2,3dmQ)_3$), shown in Figure 3.2, were synthesized and used as the emitting layer in electroluminescent devices.[96] While yellow emission at 550 nm with a maximum luminance of 3400 cd m^{-2} was observed for the $Al(CNQ)_3$ device, blue emission at 470 nm with a maximum luminance of 5500 cd m^{-2} was observed for the $Al(2,3dmQ)_3$ device. The HOMO and LUMO were -5.8 eV and -3.1 eV, respectively, for $Al(CNQ)_3$ and -5.8 eV and -2.9 eV, respectively, for $Al(2,3dmQ)_3$. Electroluminescence measurements are summarized in Table 3.1. In this study, the effect of substitution position on the quinoline ring was not examined, but it was found that the addition of an

electron-accepting group such as cyano results in an emission red-shift and the addition of an electron-donating group such as methyl results in an emission blue-shift.

Table 3.1: Summary of electroluminescence measurements of AlQ_3, $Al(CNQ)_3$, and $Al(2,3dmQ)_3$.

	λ_{EL} (nm)	L (cd m^{-2})	HOMO (eV)	LUMO (eV)
AlQ_3	520	> 1000	-6.7	-3.4
$Al(CNQ)_3$	550	3400	-5.8	-3.1
$Al(2,3dmQ)_3$	470	5500	-5.8	-2.9

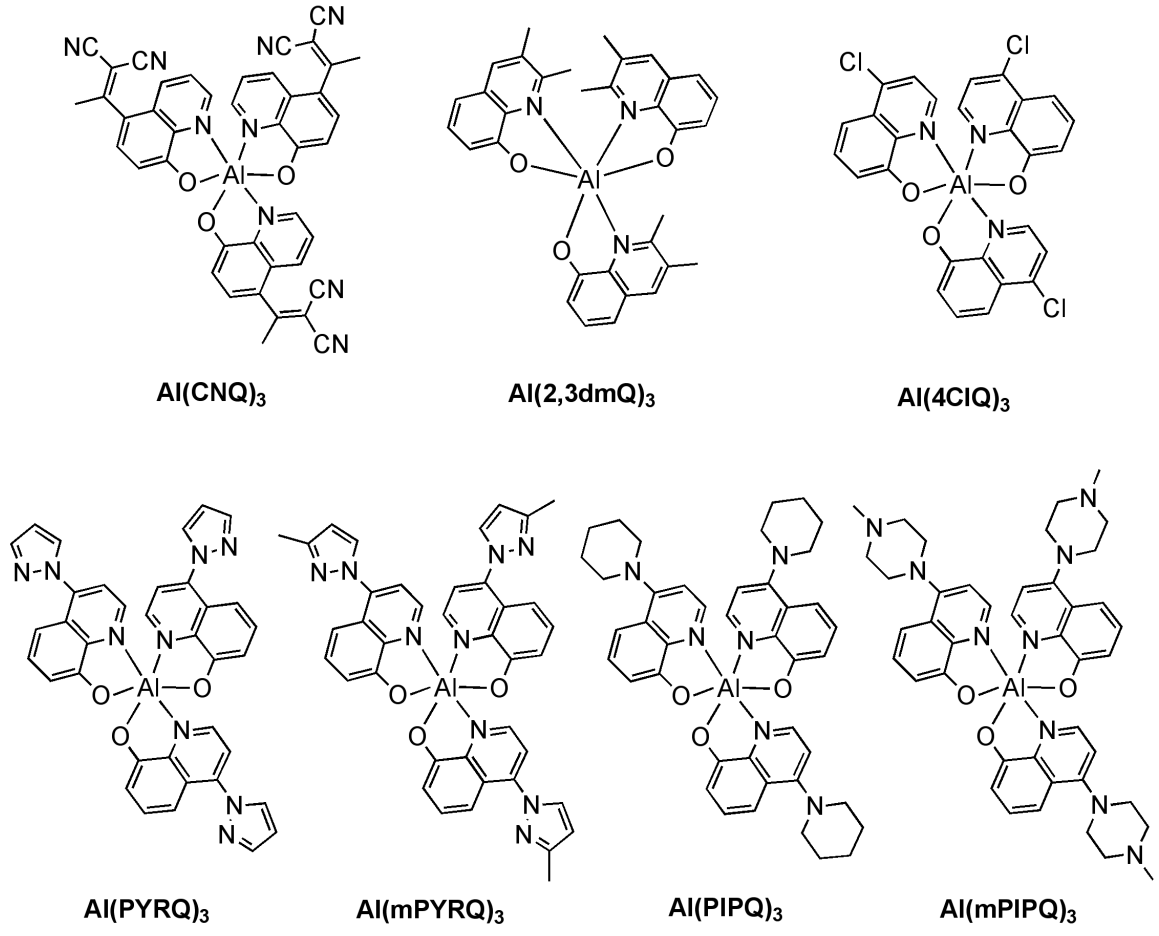

Figure 3.2: $Al(CNQ)_3$, $Al(2,3dmQ)_3$, and tris-4-substituted AlQ_3 derivatives.

To explore the effect of varying the substituents at the 4-position, five AlQ_3 derivatives were synthesized and are displayed in Figure 3.2.[97] The addition of an electron-withdrawing chloro group in $Al(4ClQ)_3$, pyrazolyl in $Al(PYRQ)_3$, and 3-methyl-pyrazolyl in $Al(mPYRQ)_3$ caused an emission red-shift in chloroform solutions in comparison with AlQ_3. On the other hand, the electron-donating piperidinyl group in $Al(PIPQ)_3$ and the *N*-methylpiperazinyl moiety in $Al(mPIPQ)_3$ caused a blue-shift. The quantum yields for $Al(PYRQ)_3$, $Al(PIPQ)_3$, and $Al(mPIPQ)_3$ were found to be higher than that of AlQ_3. The compounds $Al(PIPQ)_3$ and $Al(mPIPQ)_3$ were found to be amorphous with glass transition temperatures higher than that of AlQ_3. A device fabricated in which $Al(PYRQ)_3$ was used as the emitting layer showed electroluminescence that was red-shifted from that of an AlQ_3 device. The devices that were fabricated from $Al(PIPQ)_3$ and $Al(mPIPQ)_3$ displayed electroluminescence blue-shifted with respect to that of an AlQ_3 device. In the cases of $Al(PYRQ)_3$, $Al(PIPQ)_3$, and $Al(mPIPQ)_3$, the electroluminescence maxima were found red-shifted with respect to their photoluminescence maxima. The maximum brightness values for devices using $Al(PYRQ)_3$ and $Al(PIPQ)_3$ were found to be 9000 cd m^{-2} and 10900 cd m^{-2}, respectively. These values are significantly higher than that of a similar AlQ_3 device, with a maximum brightness of 3041 cd m^{-2}. The device fabricated from $Al(PIPQ)_3$ exhibited an external quantum efficiency of 1.15% while the corresponding AlQ_3 device had an external quantum efficiency of 0.46%. The pertinent data are summarized in Table 3.2.

Table 3.2: Photophysical, thermal, and electroluminescent properties of AlQ_3 and tris-4-substituted AlQ_3 derivatives.

	λ_{PL}[a] (nm)	ϕ_{PL}[b] (%)	E_G[c] (eV)	T_m (or T_g) (°C)	λ_{EL} (nm)	L (cd m^{-2})	η_{max} (%)	CIE coordinates
AlQ_3	512	100	3.19	412	525	3041	0.46	0.28, 0.50
$Al(4ClQ)_3$	518	146	3.11	378	nr	nr	nr	nr
$Al(PYRQ)_3$	535	202	3.05	403	555	9000	0.57	0.41, 0.53
$Al(mPYRQ)_3$	534	91	3.06	353	nr	nr	nr	nr
$Al(PIPQ)_3$	477	210	3.32	(196)	495	10900	1.15	0.20, 0.40
$Al(mPIPQ)_3$	485	338	3.29	(216)	510	1860	0.63	0.24, 0.44

[a]measured in chloroform solutions. [b]relative to AlQ_3. [c]estimated from UV-vis spectral data. nr = not reported.

A series of 5-substituted 8-quinolinolate aluminum complexes has been synthesized in which the electronic characteristics of the substituents attached through an arylethynyl ($Al(5etArQ)_3$) or aryl ($Al(5ArQ)_3$) spacer is varied.[95,98] These derivatives are displayed in Figure 3.3. Compounds in the $Al(5ArQ)_3$ series were expected to exhibit amplified emission tuning because the electronic substituents are attached directly to the quinoline ligand. This hypothesis was supported by the fluorescence spectra for the $Al(5etArQ)_3$ and $Al(5ArQ)_3$ series in dichloromethane solutions, for which the $Al(5etArQ)_3$ series spanned 80 nm and the $Al(5ArQ)_3$ series spanned 120 nm. Photoluminescence in the red to blue regions can be observed visually from these series when the solutions are excited with black light. A strong correlation between the electronic nature of the substituent and the fluorescence maxima was observed for both series. The fluorescence quantum yield and lifetime also correlate with the electronic nature of the substituent. Higher quantum yields and longer lifetimes were observed in the case of electron-poor substituents. The HOMO and LUMO levels were calculated based on cyclic voltammetry data. As expected for tuning at the 5-position, the LUMO was found to be unaffected while the HOMO energy level varied with the electronic nature of the substituent. Devices were successfully fabricated for the $Al(5ArQ)_3$ series

and the electroluminescence spectra were found to be very similar to the emission observed in solution. Unfortunately, the $Al(5etArQ)_3$ series lacked sufficient thermal and electric stability for the production of satisfactory devices. The luminance and efficiency of the devices were found to be lower than those of AlQ_3 devices. However, these devices have not been optimized. The most blue-shifted derivative, $Al(5ArQ)_3$-a, evidenced a performance comparable with that of AlQ_3. Photophysical and electroluminescent measurements are displayed in Table 3.3.

Table 3.3: Photophysical and electroluminescent data for AlQ_3 and tris-5-substituted AlQ_3 derivatives with aryl or arylethynyl spacers.

	λ_{PL}[a] (nm)	ϕ_{PL}[b] (%)	τ_F (ns)	E_G[c] (eV)	λ_{EL} (nm)	η_{max}
AlQ_3	526	17.1	15.38	2.95	520	0.83
$Al(5ArQ)_3$-a	490	53.3	29.50	nd	479	0.90
$Al(5ArQ)_3$-b	501	51.1	23.01	3.18	505	0.12
$Al(5ArQ)_3$-c	513	53.6	15.61	3.11	528	0.12
$Al(5ArQ)_3$-d	516	45.3	20.31	3.12	500	0.29
$Al(5ArQ)_3$-e	530	30.1	16.57	3.07	522	0.42
$Al(5ArQ)_3$-f	534	29.8	14.53	3.07	541	0.38
$Al(5ArQ)_3$-g	537	23.4	12.76	2.97	531	0.78
$Al(5ArQ)_3$-h	541	20.1	11.13	3.03	531	0.01
$Al(5ArQ)_3$-i	545	10.0	9.72	2.98	551	0.19
$Al(5ArQ)_3$-j	538	10.5	10.10	nd	542/672	0.03
$Al(5ArQ)_3$-k	551	9.8	6.53	2.95	555/660	0.30
$Al(5ArQ)_3$-l	564	5.7	4.73	2.47	562	0.18
$Al(5ArQ)_3$-m	564	4.9	4.33	2.47	nd	nd
$Al(5ArQ)_3$-n	612	0. 8	1.49	2.30	616	0.06
$Al(5etArQ)_3$-a	520	31.7	11.85	3.08	nr	nr
$Al(5etArQ)_3$-d	538	22.8	8.67	2.89	nr	nr
$Al(5etArQ)_3$-e	541	23.5	8.95	2.67	nr	nr
$Al(5etArQ)_3$-f	545	20.3	6.61	2.64	nr	nr
$Al(5etArQ)_3$-o	559	3.7	2.14	2.56	nr	nr
$Al(5etArQ)_3$-p	573	0.3	nr	2.45	nr	nr
$Al(5etArQ)_3$-i	561	8.8	3.56	2.53	nr	nr
$Al(5etArQ)_3$-q	561	9.2	3.30	2.55	nr	nr
$Al(5etArQ)_3$-k	569	4.7	1.86	2.35	nr	nr
$Al(5etArQ)_3$-l	573	3.6	1.28	2.35	nr	nr
$Al(5etArQ)_3$-n	600	0. 9	0.89	2.20	nr	nr

[a]measured in dichloromethane solution. [b]determined using quinine sulfate as a standard. [c]calculated from cyclic voltammetry experiments. nd = not detected. nr = not reported.

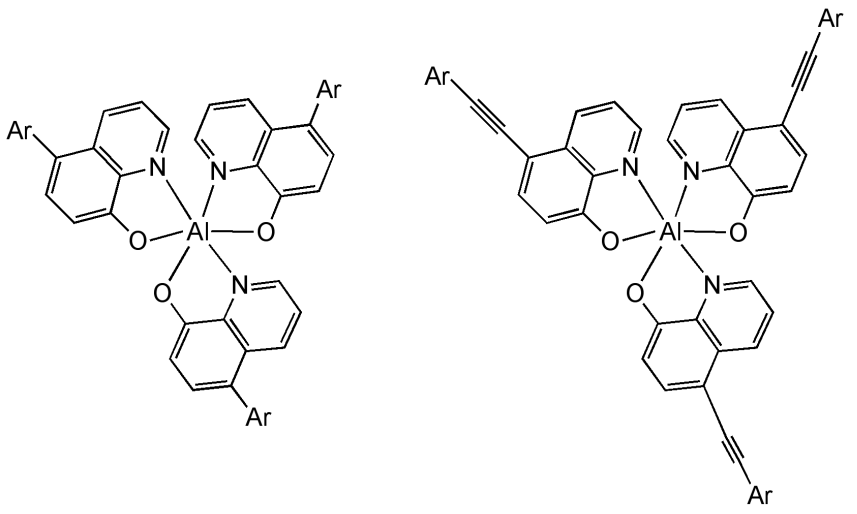

Al(5ArQ)$_3$ **Al(5etArQ)$_3$**

Ar =

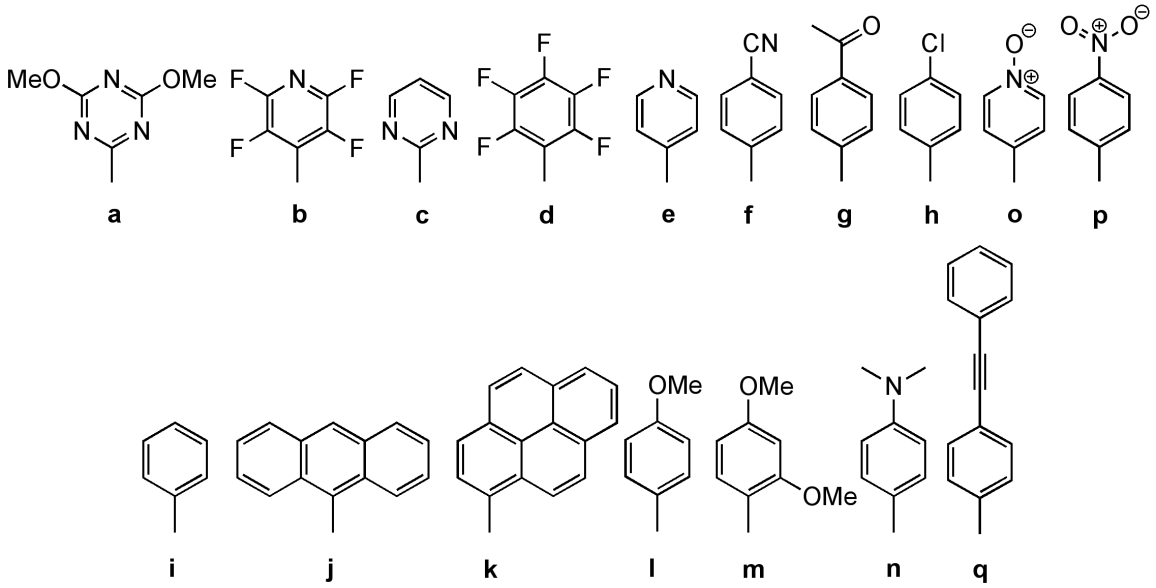

Figure 3.3: Tris-5-substituted AlQ_3 derivatives with aryl or arylethynyl spacers.

A substituted 8-hydroxyquinoline derivative, 8-hydroxy-5-piperidinylquinolinesulfonamide (QS) was synthesized and the corresponding aluminum

complex ($Al(QS)_3$) was formed, shown in Figure 3.4.[99] The sulfonamide substituent was selected because it is electron-withdrawing and offers significantly greater stability than that of a sulfonate substituent. Additionally, the piperidinyl group increases the solubility of the aluminum complex in nonpolar solvents in comparison with AlQ_3. The photoluminescence of $Al(QS)_3$ was found to be blue-shifted in comparison with the parent complex AlQ_3 in a methylene chloride solution, as a pure film, or incorporated into a poly-(vinylcarbazole) (PVK) film. The photoluminescence of $Al(QS)_3$ in solution is blue-shifted with respect to those of the $Al(QS)_3$ films. This observation may be due to excimer formation between neighboring compounds in the solid films, thus causing an emission red-shift. This effect is not observed in dilute solutions. Single-layer LEDs were fabricated with $Al(QS)_3$ and AlQ_3 in PVK using ITO and aluminum as the contacts. In each case, the electroluminescence maxima are nearly identical to those of the photoluminescence maxima, displayed in Table 3.4. The maximum internal efficiencies were approximately 0.01%. While the efficiencies for these $Al(QS)_3$ and AlQ_3 LEDs were comparable, they fall short of the efficiencies reported by Tang and Van Slyke for vacuum deposited AlQ_3 diodes.[79] However, it should be mentioned that no attempts to optimize the performance of these thin films were made.

The introduction of electron-transport substituents into a luminophor represents another method for improving device performance.[100] For example, the AlQ_3 derivative featuring electron-injecting oxadiazole substituents ($Al(OXHQ)_3$), shown in Figure 3.4, was designed and synthesized in order to improve the transporting ability of AlQ_3.[101] The fluorescence emission of $Al(OXHQ)_3$ in DMSO solution was found to be significantly blue-shifted from that of AlQ_3 with a maximum at 455 nm. This observation is most likely due to the electron affinity of the 1,3,4-oxadiazole substituent. The quantum yield

of $Al(OXHQ)_3$ in DMSO was 67% and the band gap was found to be 3.13 eV, estimated from the onset of absorption. The pertinent measurements are shown in Table 3.4.

Table 3.4: Summary of photoluminescence and electroluminescence measurements for AlQ_3 and tris-5-substituted AlQ_3 derivatives.

	$\lambda_{PL,soln}$ (nm)	ϕ_{PL}[c] (%)	$\lambda_{PL,film}$ (nm)	$\lambda_{PL,PVK}$ (nm)	$\lambda_{EL,PVK}$ (nm)	HOMO[d] (eV)	LUMO[d] (eV)	E_G[e] (eV)
AlQ_3	514[a]	17.1	519	510	508	6.65	3.43	nr
$Al(QS)_3$	480[a]	nr	502	485	482	6.50	3.24	nr
$Al(OXHQ)_3$	455[b]	67	nr	nr	nr	nr	nr	3.13

[a]measured in dichloromethane solutions. [b]meausred in DMSO solutions. [c]determined using quinine sulfate as a standard. [d]vs. vacuum. [e]estimated from the onset absorption. nr = not reported.

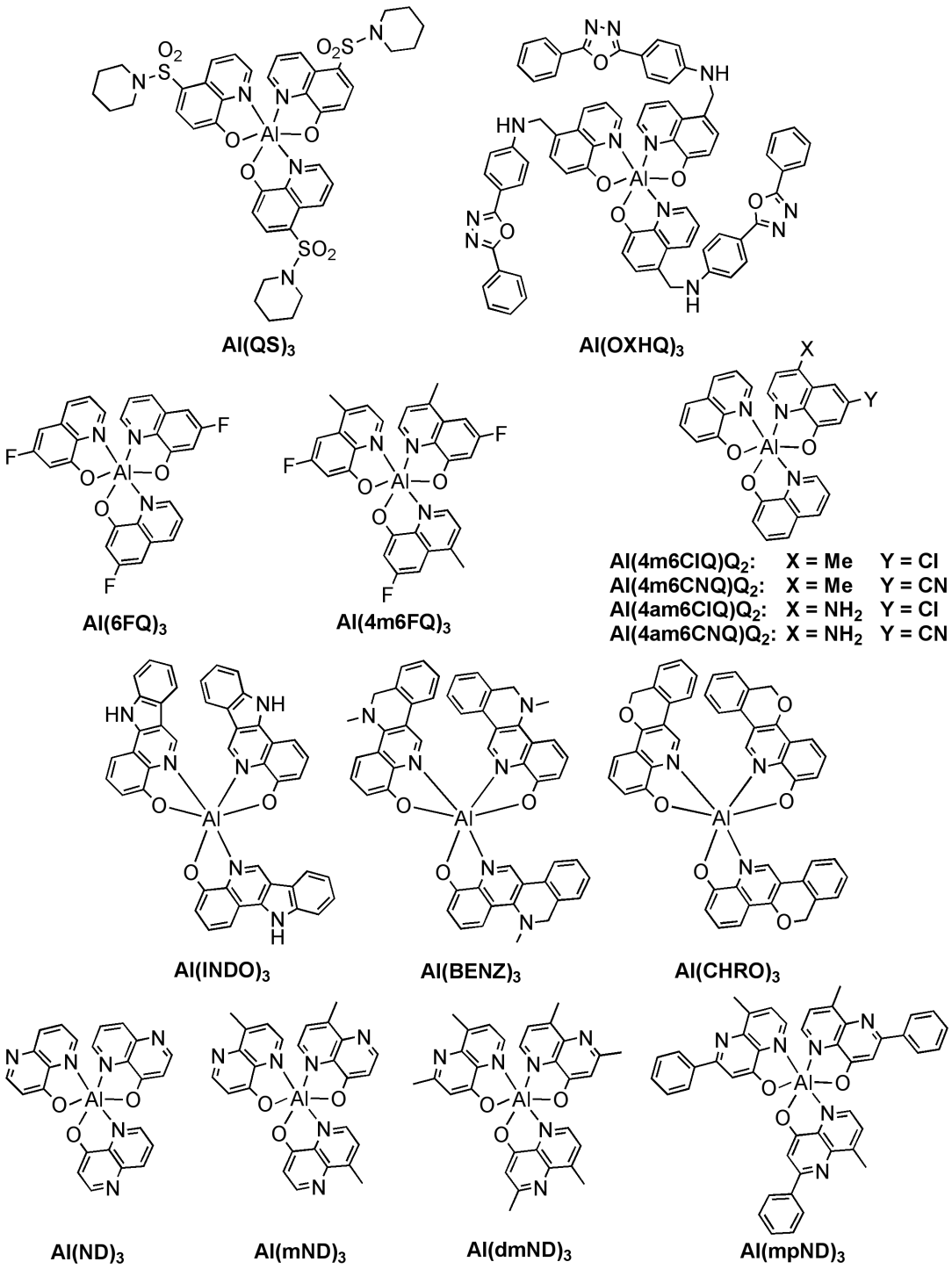

Figure 3.4: Tris-5-substituted, tris-6-substituted, theoretical, and tris-tetracyclic AlQ_3 derivatives and aluminum complexes of tris-naphthyridine derivatives.

Contrary to expectation, an AlQ_3 derivative with a fluoro group at the 5-position of 8-hydroxyquinoline caused the energy level of the HOMO to rise, thus inducing a red-shift in emission relative to AlQ_3. This observation is most likely due to conjugation effects.[102] However, appending a fluoro group at the 6-position ($Al(6FQ)_3$) resulted in the expected electron-withdrawing effect, thus lowering the HOMO and inducing a blue-shift. The placement of a fluoro group at the 7-position had very little effect on the emission wavelength. Bluish green light with a maximum emission at 495 nm was emitted by $Al(6FQ)_3$, which was prevented from a more dramatic blue-shift by the fact that both the HOMO and LUMO were lowered in energy by the introduction of the fluoro group at the 6-position. However, the HOMO energy was lowered to a greater extent than that of the LUMO. Blue emission can however be achieved by further chemical modification by using 4-methyl-6-fluoro-8-hydroxyquinoline ligands to form the aluminum complex $Al(4m6FQ)_3$, shown in Figure 3.4.[103] In chloroform solution this aluminum complex exhibits a dramatic blue-shift from both AlQ_3 and $Al(6FQ)_3$, with a maximum fluorescence emission at 467 nm. While the photoluminescence intensity of $Al(6FQ)_3$ was a 162% improvement over that of AlQ_3, $Al(4m6FQ)_3$ exhibits a photoluminescence intensity increase of 214% relative to that of AlQ_3. The glass transition temperature of $Al(4m6FQ)_3$ is 162 °C, which is close to that of AlQ_3. The decomposition of $Al(4m6FQ)_3$ occurs at 356 °C, which is indicative of excellent thermal stability. Additionally, $Al(4m6FQ)_3$ was found to be soluble in common organic solvents such as chloroform and DMF. As a consequence, thin films can be prepared by spin-coating or vacuum deposition. LUMO energy levels for AlQ_3, $Al(6FQ)_3$, and $Al(4m6FQ)_3$ were calculated based on cyclic voltammetry measurements. The band gaps were calculated using the absorption onsets in solution and the HOMO energy levels were calculated from the LUMOs and the band gaps. The HOMO level of $Al(4m6FQ)_3$

is lowered significantly from that of AlQ_3 due to the electron-withdrawing F group at the 6-position. Unlike $Al(6FQ)_3$, which experiences a drop in both the HOMO and LUMO energy levels, the drop in LUMO energy level in the case of $Al(4m6FQ)_3$ is restrained by the presence of an electron-donating methyl group at the 4-position. The pertinent parameters are displayed in Table 3.5. Theoretical predictions indicate that an even larger increase in the HOMO-LUMO band gap could be realized by using stronger electron-donating groups such as methoxy or dimethylamino at the 4-position.

Table 3.5: Photophysical parameters for AlQ_3 and tris-6-substituted AlQ_3 derivatives.

	$\lambda_{PL,soln}$[a] (nm)	$\phi_{PL,soln}$[b] (%)	$\lambda_{PL,film}$ (nm)	$\phi_{PL,film}$ (%)	HOMO[d] (eV)	LUMO[e] (eV)	E_G[f] (eV)
AlQ_3	515	100	528	100	-5.63	-2.82	2.81
$Al(6FQ)_3$	495	262	505	146	-6.18	-3.25	2.93
$Al(4m6FQ)_3$	467	314	475/478[c]	255/243[c]	-6.10	-3.10	3.00

[a]measured in chloroform solutions. [b]relative to AlQ_3. [c]spin-coated/vacuum-deposited. [d]estimated from the LUMO and E_G. [e]estimated from cyclic voltammetry experiments. [f]estimated from the onset absorptions.

The addition of electron-withdrawing and electron-donating substituents to only one of the three 8-hydroxyquinoline ligands in AlQ_3 has been theoretically studied using four disubstituted complexes of the type (4-X-6-Y-8-hydroxyquinoline)bis(8-hydroxyquinoline)aluminum ($Al(4X6YQ)Q_2$) where X is either CH_3 or NH_2 and Y represents either CN or Cl. These complexes are displayed in Figure 3.4.[104] For all four derivatives, the HOMO and LUMO energy levels are lower than the HOMO and LUMO levels of AlQ_3. The energy gaps are approximately the same as that of AlQ_3 with the exception of $Al(4m6CNQ)Q_2$, which has an energy gap 0.16 eV larger than that of AlQ_3. Theoretical emission maxima for $Al(4m6ClQ)Q_2$, $Al(4am6ClQ)Q_2$, and $Al(4am6CNQ)Q_2$ are the same as the theoretical emission maximum of AlQ_3. In the case of

$Al(4m6CNQ)Q_2$, the emission maximum is 471 nm, which represents a 52 nm blue-shift with respect to that of AlQ_3. These calculated values are displayed in Table 3.6.

Table 3.6: Calculated photophysical parameters for AlQ_3 and theoretical AlQ_3 derivatives.

	λ_{PL}[a] (nm)	HOMO[b] (eV)	LUMO[b] (eV)	E_G[b] (eV)
AlQ_3	523	-4.87	-1.65	3.22
$Al(4m6ClQ)Q_2$	523	-5.20	-1.97	3.23
$Al(4m6CNQ)Q_2$	471	-5.37	-1.99	3.38
$Al(4am6ClQ)Q_2$	522	-5.12	-1.89	3.23
$Al(4am6CNQ)Q_2$	523	-5.21	-1.98	3.23

[a]computed at the TD-PBE0/6-31G* level. [b]computed at the TD-PBE0//CIS/6-31G* level.

Three tetracyclic 8-hydroxyquinoline derivatives with strong electron-donating groups in the 4-position have been synthesized and complexed with aluminum (see Figure 3.4).[105] The photoluminescence spectra of the three complexes, tris-(11*H*-indolo[3,2-*c*]quinolin-4-ol)aluminum ($Al(INDO)_3$), tris-(5-methyl-5,6-dihydrodibenzo[*c*,*h*][1,6]naphthyridin-1-ol)aluminum ($Al(BENZ)_3$), and tris-(6*H*-isochromeno[4,3-*c*]quinolin-1-ol)aluminum ($Al(CHRO)_3$), and AlQ_3 were obtained in solution. Ethanol was used in the case of $Al(INDO)_3$ and chloroform was the solvent of choice for $Al(BENZ)_3$ and $Al(CHRO)_3$ due to solubility differences. Reference AlQ_3 photoluminescence spectra were recorded in both solvents. Typically, increasing the degree of conjugation results in a red-shift.[106] However, all three tetracyclic derivatives exhibit a blue-shift with respect to AlQ_3. This observation implies that the strong electron-donating group at the 4-position exhibits a larger influence on the emission than the extended conjugation. The complex $Al(INDO)_3$ has CIE coordinates of (0.16, 0.12), which corresponds to deep blue emission. A deep blue emission, or one with a small *y* value for the CIE coordinate, results in a decrease in power consumption in these devices.[107] The exceptionally large blue-shift in the case of $Al(INDO)_3$ may be due to the

presence of an electron-donating group at the 4-position which is fully conjugated to the 3-position. In the cases of $Al(BENZ)_3$ and $Al(CHRO)_3$, the electron-donating group at the 4-position is isolated from the 3-position. The fluorescence quantum yield of $Al(INDO)_3$ is 35% while that of AlQ_3 in ethanol is 11.6%.[108] In the case of $Al(CHRO)_3$, the fluorescence quantum yield is significantly higher than that of its non-fused analogue, tris-(4-benzyloxy-8-hydroxyquinoline)aluminum, which has a similar blue-shifted emission at 465 nm and a fluorescence quantum yield of 66% relative to AlQ_3.[109] This observation can be attributed to the rigid fused structure of the tetracyclic ligand. The complex $Al(BENZ)_3$ showed a two exponential decay, with relative amplitudes of 15% and 85% and lifetimes of 9.7 nm and 1.8 nm, respectively. Using a spin-coating technique, thin films of each tetracyclic derivative were deposited on quartz substrates. While the thin film of $Al(INDO)_3$ revealed a very weak absorption, clear emission peaks were observable and found to be similar to those displayed in solution. The thin film of $Al(BENZ)_3$ showed no fluorescence. The CIE coordinates for $Al(INDO)_3$ were again located in the deep blue region. No melting endotherms could be detected for $Al(INDO)_3$ and $Al(BENZ)_3$ in DSC analyses, thus indicating that these films are amorphous. While the complex $Al(BENZ)_3$ exhibited a T_g that was 11 °C higher than that of AlQ_3, the T_g values for $Al(INDO)_3$ and $Al(CHRO)_3$ were found to be 20 and 9 °C lower, respectively. Spin-coating may therefore not be the ideal technique for the formation of these films. However, results imply the potential use of these new materials providing a suitable deposition technique is employed. The pertinent photophysical parameters are displayed in Table 3.7.

Table 3.7: Photophysical parameters for AlQ_3 and tris-tetracyclic AlQ_3 derivatives.

	Solution				Solid		
	λ_{PL} (nm)	ϕ_{PL}[c] (%)	τ_F (ns)	CIE coordinates	λ_{PL} (nm)	τ_F (ns)	CIE coordinates
AlQ_3	519[a]/522[b]	100	8.99[a]/16.63[b]	0.33, 0.52	518	10.77	0.28, 0.53
$Al(INDO)_3$	442[a]	306	7.76	0.16, 0.12	442	0.77	0.18, 0.16
$Al(BENZ)_3$	499[b]	14	9.73/1.81	0.25, 0.41	nr	nr	nr
$Al(CHRO)_3$	478[b]	145	11.76	0.18, 0.28	480	nr	0.23, 0.32

[a]measured in EtOH solution. [b]measured in $CHCl_3$ solution. [c]relative to AlQ_3.
[d]fluorescence decay is two exponential; values are given for the 15% component/85% component. nr = not reported.

Replacement of a carbon in the phenoxide ring of 8-hydroxyquinoline by a nitrogen results in the formation of 4-hydroxy-1,5-naphthyridine (ND). The aluminum complex formed with this ligand, tris(4-[1,5]naphthyridinolato)aluminum, ($Al(ND)_3$) shows an emission blue-shift from that of AlQ_3 without losing the rigid and globular structure or volatility of the AlQ_3 complex.[84] A blue-shift has also been reported for tris(4-methyl-8-quinolinolato)aluminum.[110] The ligand that combines these two features, namely 4-hydroxy-8-methyl-1,5-naphthyridine (mND), was designed and synthesized along with two derivatives that feature an additional substituent at the 2-position, namely 2,8-dimethyl-4-hydroxy-1,5-naphthyridine (dmND) and 4-hydroxy-2-phenyl-1,5-naphthyridine (mpND).[84] Using these three ligands, three aluminum complexes were formed, as shown in Figure 3.4. In dichloromethane solution, these aluminum complexes had quantum yields between 45-47% and exhibited deep blue fluorescence between 415-417 nm. In the solid state, fluorescence maxima for $Al(dmND)_3$, $Al(mpND)_3$, $Al(mND)_3$ and $Al(ND)_3$ were red-shifted to 419, 425, 431 and 447 nm, respectively. Of the four aluminum complexes, $Al(dmND)_3$ has the smallest shift in fluorescence between the solution and solid phases. This observation may be due to a different morphology of aggregation in the solid state compared with the other aluminum complexes. Each

aluminum complex undergoes fluorescence concentration quenching in the solid state. The observation that this occurs to the greatest extent with $Al(mpND)_3$ is most likely due to π-π interactions between the phenyl substituents. The HOMO energy level of $Al(mND)_3$ is 6.4 eV below vacuum level, which is significantly lower than that of AlQ_3, for which the value is 5.9 eV. The LUMO energy levels of $Al(mND)_3$ and AlQ_3 are similar, namely 3.0 and 3.1 eV respectively. The HOMO and LUMO levels of $Al(mND)_3$ are significantly lower in energy than those of other blue fluorophores, making $Al(mND)_3$ a superior hole-blocking and electron-transporting material. The charge carrier mobilities for $Al(mND)_3$ are higher than those of $Al(dmND)_3$ and AlQ_3 for both holes and electrons. Additionally, $Al(mND)_3$ seems to be ambipolar, as indicated by very similar hole and electron mobilities. The electron mobility in $Al(dmND)_3$ is higher than the hole mobility, which is beneficial because it leads to enhanced charge balance and therefore enhanced efficiency in devices that are normally dominated by holes. The DSC thermograms show a T_g of 122 °C for $Al(ND)_3$, 196 °C for $Al(mND)_3$, 233 °C for $Al(dmND)_3$ and 204 °C for $Al(mpND)_3$. Except for $Al(ND)_3$, all the T_g values are higher than that for AlQ_3. High T_g values are indicative of superior morphological stability and glass phase stability, which, in turn, results in longer operation lifetimes for the OLEDs. With the exception of $Al(mpND)_3$, all the complexes exhibited melting points higher than that of AlQ_3. In aluminum complexes of this type, the melting process is rapidly followed by decomposition, hence higher melting points are indicative of enhanced thermal stability. OLEDs were fabricated using these complexes and it was found that the $Al(dmND)_3$ OLED had the shortest electroluminescence maximum wavelength (436 nm), the highest external quantum efficiency (4.18%), and the brightest electroluminescence (445 cd m^{-2}) at 20 mA/cm^2. The pertinent photophysical, thermal, and electroluminescent measurements are presented in Tables 3.8 and 3.9.

Table 3.8: Photophysical and thermal data for AlQ_3 and aluminum complexes of tris-naphthyridine derivatives.

	$\lambda_{PL,soln}$[a] (nm)	$\phi_{PL,soln}$ (%)	$\lambda_{PL,solid}$ (nm)	$\phi_{PL,solid}$ (%)	T_m (°C)	T_g (°C)	HOMO (eV)	LUMO (eV)
AlQ_3	524	20	516	40	412	174	5.9	3.1
$Al(ND)_3$	433	47	447	45	412	122	nr	nr
$Al(mND)_3$	415	45	431	43	420	196	6.4	3.0
$Al(dmND)_3$	416	45	419	39	436	233	nr	nr
$Al(mpND)_3$	417	45	425	6	370	204	nr	nr

[a]measured in dichloromethane solutions. nr = not reported.

Table 3.9: Electroluminescence measurements for aluminum complexes of tris-naphthyridine derivatives.

	λ_{EL} (nm)	L (cd m^{-2})	CIE coordinates
$Al(ND)_3$	466	2286	0.15, 0.19
$Al(mND)_3$	448	3824	0.15, 0.09
$Al(dmND)_3$	436	3792	0.15, 0.07
$Al(mpND)_3$	452	4078	0.15, 0.12

Bis 8-Hydroxyquinoline Aluminum Derivatives

The emission blue-shifts when coordination number of aluminum is reduced from 6 to 5.[111] This occurs because the covalency between the metal and nitrogen is decreased when the number of M-N bonds decreases.[112] The 8-hydroxyquinoline derivative, 2-methyl-8-hydroxyquinoline, has been used for the synthesis of aluminum complexes.[113] On account of significant steric effects, the otherwise stable tris-2-methyl-8-hydroxyquinoline aluminum complex will not form directly. As a consequence, it is necessary to include a secondary ligand such as a phenolato group in order to form bis(2-methyl-quinolinolato)(phenolato) aluminum(III) ($Al(2mQ)_2p$). Devices that were made using $Al(2mQ)_2p$ exhibited emission that was shifted from that of AlQ_3 to the blue region of the spectrum. The maximum emission occurred at 495 nm. The use of $Al(2mQ)_2p$ as a light-emitting material is advantageous because all the desirable properties of AlQ_3 are

retained while the emission is blue-shifted. To further explore the role of the secondary ligand, two additional aluminum complexes were synthesized using phenolato derivatives, namely bis(2-methyl-quinolinolato)(4-chloro-phenolato) aluminum(III) ($Al(2mQ)_2Clp$) and bis(2-methyl-quinolinolato)(4-methoxy-phenolato) aluminum(III) ($Al(2mQ)_2mp$). However, replacement of the phenolato group with 4-chloro-phenolato or 4-methoxy-phenolato resulted in emission that is red-shifted with respect to that of $Al(2mQ)_2p$. It has been reported previously that substituting 2-methylphenolate for phenolate resulted in an emission blue-shift due to steric effects.[94] While the steric properties of $Al(2mQ)_2Clp$ and $Al(2mQ)_2mp$ are not significantly different from that of $Al(2mQ)_2p$, the chloro group is electron-withdrawing and the methoxy group is electron-donating. It is therefore unexpected that both substitutions would result in red-shifting. The compound $Al(2mQ)_2p$ and its derivatives are displayed in Figure 3.5 and photoluminescence and electroluminescence measurements are listed in Tables 3.10.

To further explore the influence of the electronic nature of the secondary ligand (L) six complexes of the type $Al(2mQ)_2L$ were synthesized and are displayed in Figure 3.5.[114] In addition to varying the electronic nature of the secondary ligand, both mononuclear and binuclear complexes were explored. The charge transport can be improved by linking the metal centers,[115] which results in an OLED material with good charge carrier mobility. The emission from these complexes was found to be blue-shifted with respect to AlQ_3. However, no appreciable differences were evident among the complexes. Furthermore, the quantum yields were on the same order of magnitude as that of AlQ_3. Comparison of the emissions from solutions and solids of these complexes revealed that both red and blue-shifts occur. This observation implies that the secondary ligand may have an effect on the intermolecular interactions. The secondary ligand also influences the shape of the emission band in the solid phase. Thus, the secondary ligand

could be used to increase the percentage of emission in the blue region, resulting in an indirect tuning effect on the character of the emitted light. No differences were observed between the mononuclear and binuclear complexes. The photoluminescent data are displayed in Tables 3.10.

Table 3.10: Photoluminescence and electroluminescence measurements of bis(2-methylquinolinolato)(phenolato) aluminum and derivatives.

	$\lambda_{PL,soln}$[a] (nm)	$\lambda_{PL,solid}$ (nm)	λ_{EL} (nm)	L (cd m^{-2})
$Al(2mQ)_2p$	nr	470[b]	495	4000
$Al(2mQ)_2Clp$	nr	485[b]	505	2900
$Al(2mQ)_2mp$	nr	486[b]	513	1000
$Al(2mQ)_2etp$	490	460[c]	nr	nr
$Al(2mQ)_2CNp$	480	490[c]	nr	nr
$Al(2mQ)_2nip$	480	468[c]	nr	nr
μ-OArO-$(Al(2mQ)_2)_2$-a	480	488[c]	nr	nr
μ-OArO-$(Al(2mQ)_2)_2$-b	490	480[c]	nr	nr
μ-OArO-$(Al(2mQ)_2)_2$-c	480	476[c]	nr	nr

[a]measured in dichloromethane solutions. [b]measured as pure films on quartz glass. [c]measured as KBr pellets. nr = not reported.

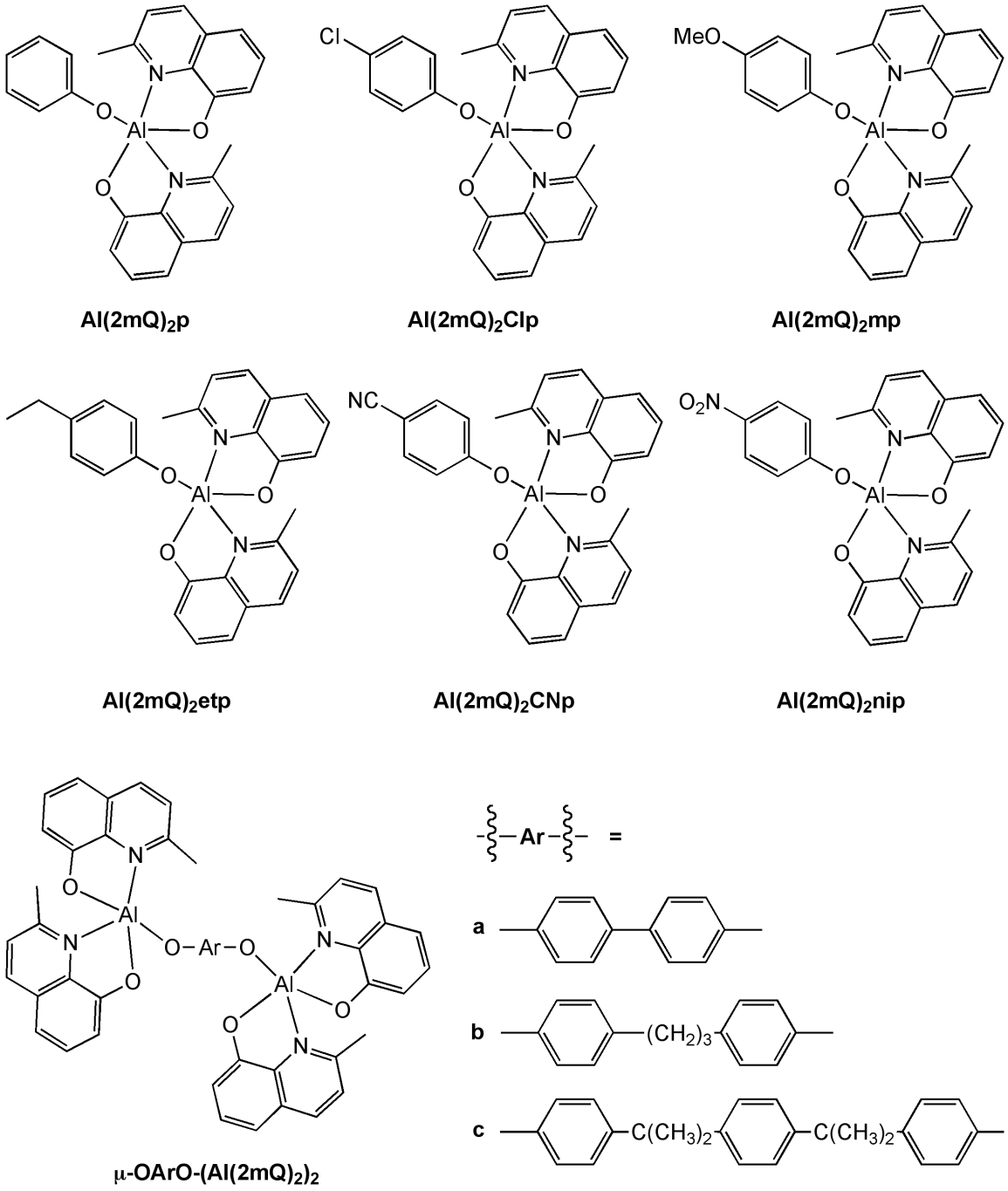

Figure 3.5: Bis(2-methylquinolinolato)(phenolato) aluminum and mononuclear and bridged dinuclear derivatives.

Five pentacoordinate aluminum complexes containing a phenolic ligand or an oxygen bridge and two 2,4-dimethyl-8-hydroxyquinolines (2,4dmQ) have been synthesized and their structures are displayed in Figure 3.6.[116] Since there are two methyl groups on the pyridyl ring, 2,4dmQ is used for blue-shifted emission. Chloroform solutions of each of the five new aluminum complexes exhibited very similar fluorescence spectra with maxima at approximately 490 nm. The spectra were blue-shifted from those of AlQ_3 and tris(4-methyl-8-hydroxyquinoline) aluminum (III) ($Al(4mQ)_3$) by 30 and 12 nm, respectively. Interestingly, the emission maxima do not vary when the phenolic ligand or the oxygen bridge is changed. The fluorescence spectra of amorphous, vacuum deposited films exhibited maxima that were shifted approximately 10 nm longer than those of the chloroform solutions. In the case of microcrystalline powders, the fluorescence spectra were found to be 25 nm shorter than those of the films. This observation is most likely due to crystallization. Additionally, the fluorescent bands differ for each powder, most likely due to varying degrees of crystallinity and crystal form. The electroluminescent spectra of each complex fall in the blue region. The pertinent photoluminescence and electroluminescence measurements are listed in Table 3.11.

A similar 5-coordinate aluminum complex featuring two 2,4dmQ ligands and a triphenylsiloxy group has been synthesized and the resulting structure is displayed in Figure 3.6.[117] The bulky triphenylsiloxy group was chosen to minimize intermolecular interactions. As intermolecular interactions decrease, a blue-shift is expected.[82] This complex has a melting point of 246 °C and begins to decompose at 340 °C. The photoluminescence spectrum displayed a maximum at 461 nm. A device fabricated using $Al(2,4dmQ)_2tps$ as the hole-blocking layer displayed an emission maximum at 446 nm, the parameters for which are listed in Table 3.11.

Table 3.11: Photoluminescence parameters and electroluminescence measurements for AlQ_3, $Al(4mQ)_3$, and the bis(2,4-dimethylquinolinolato) aluminum derivatives.

	$\lambda_{PL,soln}$[a] (nm)	ϕ_{PL}[b] (%)	$\lambda_{PL,powder}$ (nm)	$\lambda_{PL,film}$ (nm)	λ_{EL} (nm)	CIE coordinates
AlQ_3	518.0	13	500	520	532	0.34, 0.56
$Al(4mQ)_3$	501.0	31	nr	nr	nr	nr
$Al(2,4dmQ)_2p$	488.8	24	482.2	501.2	493	0.20, 0.35
$Al(2,4dmQ)_2etbp$	489.2	23	468.4	499.4	487	0.20, 0.31
$Al(2,4dmQ)_2pep$	489.0	24	467.0	491.8	478.5	0.20, 0.28
$Al(2,4dmQ)_2prbp$	490.0	25	473.2	489.4	491	0.21, 0.36
μ-O-$(Al(2,4dmQ)_2)_2$	489.8	25	491.8	501.6	494.5	0.21, 0.36
$Al(2,4dmQ)_2tps$	nr	nr	nr	461	446	0.16, 0.13

[a]measured in chloroform solutions. [b]referenced to anthracene. nr = not reported.

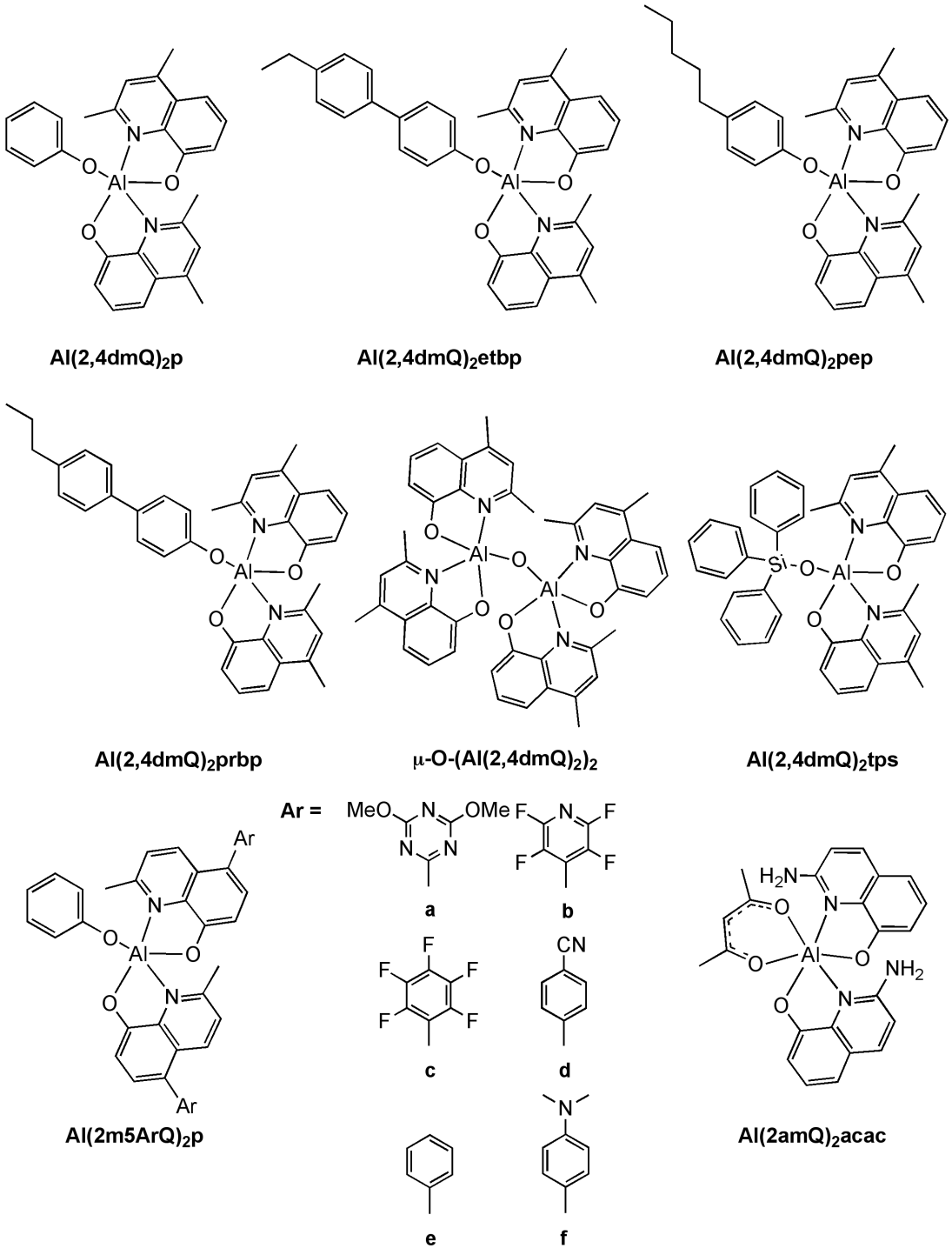

Figure 3.6: Bis(2,4-dimethylquinolinolato) aluminum derivatives, bis(2-methyl-5-arylquinolinolato)(phenolato) aluminum derivatives and $Al(2amQ)_2acac$.

As previously mentioned, quinolinolate derivatives with electron-donating and electron-withdrawing groups at the 5-position have been used to form AlQ_3 derivatives.[95,98] An emission red-shift was observed in the case of electron-donating groups and a blue-shift was observed for electron-withdrawing groups. The combined effect of two substituents that cause an emission blue-shift may be a more effective way to synthesize a genuine blue AlQ_3 derivative. For this reason, quinolinolate ligands with two substituents were synthesized and corresponding aluminum complexes were formed, as shown in Figure 3.6.[89] A methyl group in the 2-position of the quinolinolate ligand (2mQ) is known to result in an emission blue-shift for the resulting aluminum complex.[113] A variety of electron-donating and electron-withdrawing substituents were used at the 5-position of 2mQ. Emission color tuning from blue to red can be observed when methylene chloride solutions are excited with a black light. The emission maxima ranged from 455-575 nm and it appears that the two substituents on the quinolinolate ligand have an additive effect on emission. Cyclic voltammetry reveals that the LUMO levels for this series are similar to each other, but the HOMO levels vary widely across the series. This is most likely because the methyl group in each complex of the series resides at the 2-position of the ligand, which is the area of highest LUMO density. The 5-position is the area of highest HOMO density, and the substituent in this position is varied across the series. The quantum yields ranged from 30-60% for complexes a-d (Figure 3.6). Photoluminescent data is summarized in Table 3.12.

Table 3.12: Photoluminescent parameters for $Al(2mQ)_2p$ and bis(2-methyl-5-arylquinolinolato)(phenolato) aluminum derivatives.

	$\lambda_{PL,soln}$[a] (nm)	ϕ_{PL}[b] (%)	$\lambda_{PL,solid}$ (nm)	HOMO[c] (eV)	LUMO[c] (eV)	E_G[c] (eV)
$Al(2mQ)_2p$	495	40	492	-6.27	-3.14	3.13
$Al(2m5ArQ)_2p$-a	455	60	467	-6.47	-3.21	3.26
$Al(2m5ArQ)_2p$-b	468	40	487	-6.43	-3.18	3.24
$Al(2m5ArQ)_2p$-c	484	60	485	-6.42	-3.19	3.22
$Al(2m5ArQ)_2p$-d	504	30	504	-6.14	-3.19	2.94
$Al(2m5ArQ)_2p$-e	515	10	513	-6.14	-3.20	2.94
$Al(2m5ArQ)_2p$-f	574	>1	nd	<6.20	-3.18	<3.00

[a]measured in dichloromethane solution. [b]determined using quinine sulfate as a standard. [c]calculated from cyclic voltammetry data. nd = not detected.

An aluminum complex bearing two 2-amino-8-hydroxyquinoline ligands and an acetylacetone ligand, $Al(2amQ)_2acac$, was synthesized to determine the influence of an electron-donating group in the 2-position of 8-hydroxyquinoline, as shown in Figure 3.6.[70] Theoretical calculations indicate that the placement of an amino group in the 2-position influences the electron density distribution of the HOMO, and to a greater extent, the LUMO. In a dilute chloroform solution, this complex displayed emission at 460 nm and as a smooth film on quartz, it displayed emission at 465 nm. Both emissions were significantly blue-shifted, by 56 nm and 53 nm respectively, from the emission of AlQ_3 under identical conditions. The pertinent photoluminescent parameters are summarized in Table 3.13. The photoluminescence quantum yield for $Al(2amQ)_2acac$ in chloroform solution is similar to that reported for AlQ_3 in the same solvent.[108] The average fluorescence lifetime is 1.5 ns in both solution and solid state. A device was fabricated using $Al(2amQ)_2acac$ as the emitting layer. This device displayed electroluminescence that matched the photoluminescence spectrum of this complex, indicating that the electroluminescence of the device stems from the complex. The CIE coordinates were found to be 0.19, 0.23. Doping of $Al(2amQ)_2acac$ with the red

phosphorescent iridium complex, bis[1-(4,6-difluorophenyl)isoquinolinato] acetylacetonato iridium, resulted in a near-white emitting device. This device featured CIE coordinates of 0.41, 0.35, whereas the coordinates for true white light are 0.33, 0.33. Variation of the dopant concentration can alter the relative contributions to electroluminescence emission intensity of both the aluminum and the iridium complexes.

Table 3.13: Photoluminescence measurements for AlQ_3 and $Al(2amQ)_2acac$.

	$\lambda_{PL,soln}$[a] (nm)	τ_{soln}	$\lambda_{PL,film}$ (nm)	τ_{film}	CIE coordinates
AlQ_3	516	16.67	512	11.43	nr
$Al(2amQ)_2acac$	460	1.46	465	1.47	0.19, 0.23

[a]measured in chloroform solutions. nr = not reported.

Doping and Deuterating 8-Hydroxyquinoline Aluminum Derivatives

Many fluorescent organic molecules are efficient only when they are highly dispersed.[118] Color tuning can be accomplished by means of organic fluorescent dyes that are introduced into the host material in very small concentrations. The dopant is excited by energy transfer from the host material and functions as an emitting center. Dopants are known to increase device efficiency and often increase stability of the device. At high concentrations, however, dopants can aggregate, which results in electroluminescence quenching, band broadening, and a red-shift. For this reason, the dopant concentration must be carefully controlled so that reproducible electroluminescent maxima and efficiencies are obtained. In this context, perylene is an ideal dopant for blue emitting devices because the photoluminesent quantum yield of this compound is as high as 94% at low perylene concentrations.[119] However, perylene readily undergoes aggregation due to its planarity, which causes concentration-dependent complications such as electroluminescence quenching and red-shifting.[120] A nonplanar perylene derivative, 2,5,8,11-tetra-tert-butylperylene (TBP) has been reported to have similar

photophysical properties to those of perylene.[121] However, TBP has a higher melting point than perylene and therefore offers increased thermal stability.[122] Devices were fabricated using TBP as the dopant and bis(2-methyl-8-quinolinolato)(para-phenylphenolato)aluminum(III) ($Al(2mQ)_2bp$) as the host material.[118] The structures of TBP and $Al(2mQ)_2bp$ are presented in Figure 3.7. Similar devices using perylene as a dopant and $Al(2mQ)_2bp$ as a host material were also fabricated for comparison. For both dopants, the devices were made using a dopant concentration of 1-5%. For TBP at 1% and 5% dopant concentration, the CIE chromaticities were (0.168, 0.273) and (0.175, 0.273), respectively. In the case of perylene, the CIE chromaticities changed from (0.165, 0.196) at 1% dopant concentration to (0.178, 0.252) at 2% dopant concentration. The TBP-doped devices display constant chromaticity over a larger range of dopant concentration than the corresponding perylene-doped devices.

The light-emitting efficiency and high-voltage stability of OLEDs can be enhanced by deuteration of an organic material.[123] In contrast to fluorination, deuteration does not alter the emission maxima of photoluminescence and electroluminescence.[102] The decrease in C-D bond vibrational frequency compared to that of C-H suppresses electronic-vibration-coupling relaxation of the electronic excited state, thus increasing the fluorescence lifetime from 11 to 17.3 ns for D-AlQ_3 when compared with AlQ_3. Additionally, deuteration leads to an increase in the fluorescence quantum yield. In a multilayer device, a 1.5-fold increase in external quantum efficiency was observed at 400 mA/cm^2 for the device fabricated with D-AlQ_3 compared with the protonated device. At 500 mA/cm^2, the external quantum efficiency ratio is 2.8. This may result from the faster high-voltage-induced degradation of the protonated device in comparison with the deuterated device. The current density is higher for the deuterated device and increases in an almost linear fashion to 16 V for both the deuterated and protonated devices. The

brightness reaches a maximum critical voltage of 12.5 V for D-AlQ_3 and 11.5 V for AlQ_3. Beyond these critical voltages, the brightness diminishes rapidly due to irreversible degradation of AlQ_3. In order to determine whether the improvements in high-voltage stability and external quantum yields is applicable to other OLED materials, deuterated bis(2-methyl-8quinolinolato)(2,6-dimethyl-phenolato)aluminum(III) (D-Al(2mQ)$_2$dmp) was synthesized (see Figure 3.7). In this complex, the fluorescence lifetime increased from 14.3 to 19.9 ns upon deuteration and the fluorescence quantum yield increased from 12 to 22.6%. The devices were fabricated using D-Al(2mQ)$_2$dmp and protonated Al(2mQ)$_2$dmp. The electroluminescence maximum shifted from 490 nm to 500 nm upon deuteration. The external quantum efficiency of the D-Al(2mQ)$_2$dmp device is 1.9-fold higher than that of Al(2mQ)$_2$dmp at 50 mA/cm^2 and 2.8-fold higher at 150 mA/cm^2. The decrease in brightness occurred at the same critical high voltage for both D-Al(2mQ)$_2$dmp and Al(2mQ)$_2$dmp, indicating that deuteration does not increase the high voltage stability of the Al(2mQ)$_2$dmp complex. Deuteration may be applied to other OLED materials in order to improve efficiency (and in some cases, to improve high voltage stability). Due to improved efficiencies, deuterated devices can deliver the same intensity while consuming less power than the corresponding protonated devices.

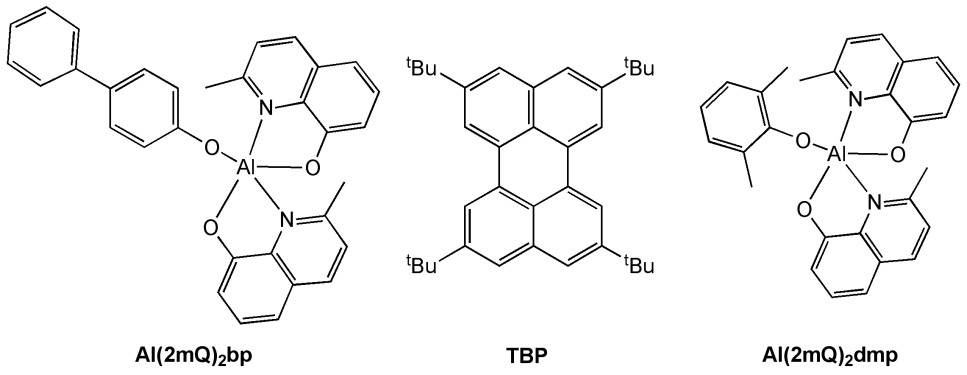

Al(2mQ)$_2$bp TBP Al(2mQ)$_2$dmp

Figure 3.7: Al(2mQ)$_2$bp, TBP, and Al(2mQ)$_2$dmp.

Supramolecular and Polymeric 8-Hydroxyquinloine Aluminum Derivatives

Calixarenes are cyclo-oligomers that form a cup-like shape. As such, they are good host molecules due to the presence of a preformed cavity.[124] The selectivity for guest ions and small molecules is made possible by functionally modifying the calixarene, thus rendering the calixarene class of ligand useful in many applications. A calixarene aluminum species with a quinoline entity (calAlQ), which is displayed in Figure 3.8, has been synthesized and used as the emissive and electron-transporting material in a supramolecular OLED in order to explore the photophysical properties. This device displayed an electroluminescent emission, which is tunable from 470-510 nm, depending on the applied voltage. The supramolecular OLED device exhibited a lifetime of hundreds of hours without perceivable degradation and a stability superior to that of a conventional device fabricated with AlQ_3. Calixarenes are known to have high chemical stability and can therefore protect the quinoline chromophore. The external quantum efficiency was found to be 0.01%. This low value is most likely due to the use of an aluminum cathode, the unoptimized thickness of the calixarene complex layer, and the differing carrier mobilities in the calixarene layer. This device could probably be improved by using a LiF/Al cathode, optimizing the calixarene layer thickness, and adding a hole-blocking layer.

Polymeric metal complexes with bicoordinate ligands combine the advantages of inorganic metal ions and conjugation polymers and often offer good thermal stability, processability, and facile film formation.[125] A ligand featuring π-conjugation and two 8-hydroxyquinoline groups has been designed and synthesized.[126] A polymeric aluminum complex featuring this ligand, polyAlQetp, is displayed in Figure 3.8. This complex has a fluorescence maximum at 514 nm in the solid state. In DMSO solution, the fluorescence maximum was found to be 470 nm. Thermal analyses of polyAlQetp

indicate that a 2.7% mass loss occurs at 280 °C, which is attributable to the loss of absorbed water molecules. A 26.5% mass loss is observed between 280 and 358 °C, which may be caused by decomposition of the main chain of the polymeric metal complex. DSC analysis indicates a T_g of 167 °C.

A norbornene monomer with an AlQ_3 complex appended via an eight atom spacer has been polymerized, resulting in polyAlQ_3. The resulting material displays an emission at a wavelength almost identical to that of pure AlQ_3.[127] Similar polymers with modified AlQ_3 complexes have also been synthesized. Furthermore, these polymers displayed the same optical properties of the small molecules from which they were derived in both solution and the solid state.[128] The pertinent polymers are displayed in Figure 3.8. Like modified AlQ_3 complexes, these polymers displayed a shift in emission wavelength, which is related to the electronic nature of the substituent. In solution, the most dramatic emission blue-shift occurred for poly$AlQ(naph)_2$, which exhibited an emission maximum of 430 nm. Other polymers that are blue-shifted from polyAlQ_3 include poly$AlQ(5CHOQ)_2$, with an emission maximum at 488 nm, poly$AlQ(5SQ)_2$ with an emission maximum at 508 nm, and poly$AlQ(2m5,7dClQ)_2$ with an emission maximum at 510 nm. The polymer poly$AlQ(niQ)_2$ also showed emission at 510 nm. However, the intensity of the emission was very low. The polymer poly$AlQ(naph)_2$ exhibits two emission maxima due to the presence of two ligands around the aluminum center. The polymer poly$AlQ(5CHOQ)_2$ displays a similar emission pattern along with a small shoulder at 450 nm. Emission shifts were observed in the solid state but to a lesser extent than in solution. A summary of emission maxima is presented in Table 3.14. Conductivity studies were carried out on thin films of polyAlQ_3 with copolymer in three ratios. All three films were found to be conductive, with the highest conductivity resulting for the film with the largest concentration of polyAlQ_3. The foregoing

observation indicates that the use of these polymers as the electron-transport and emission layer in OLEDs is promising. The emission wavelength was found to blue-shift as the concentration of polyAlQ$_3$ decreased. Similar results were found for polyAlQ(5CHOQ)$_2$. However, no shift was observed between 1:50 and 1:100 polyAlQ(5CHOQ)$_2$:copolymer ratios, thus indicating that this effect is limited. A summary of these results is presented in Table 3.15. It was found that the emission wavelength is dependent on the packing of AlQ$_3$, with shorter inter-ligand distances resulting in a red-shift, consistent with previous studies.[81] Additionally, it was found that polymer weight has little to no effect on emission wavelength.

Table 3.14: Emission maxima for polymeric AlQ$_3$ derivatives.

	$\lambda_{PL,soln}$[a] (nm)	$\lambda_{PL,solid}$ (nm)
PolyAlQ$_3$	523	511
PolyAlQ(5CHOQ)$_2$	488	510
PolyAlQ(2m5,7dClQ)$_2$	510	505
PolyAlQ(naph)$_2$	430, 490	437, 498
PolyAlQ(5niQ)$_2$	510	nr
PolyAlQ(5SQ)$_2$	508	495

[a]measured in chloroform solutions. nr = not reported.

Table 3.15: Conductivity and emission maxima for polymers of varying AlQ$_3$ derivatives:copolymer ratio.

	AlQ$_3$ derivative: copolymer	Conductivity (s cm^{-1})	$\lambda_{PL,soln}$ (nm)	$\lambda_{PL,solid}$ (nm)
PolyAlQ$_3$	1:5	12	nr	nr
	1:10	9	522	522
	1:20	4	523	511
	1:50	nr	522	502
PolyAlQ(5CHOQ)$_2$	1:10	nr	486	522
	1:20	nr	488	510
	1:50	nr	487	494

nr = not reported.

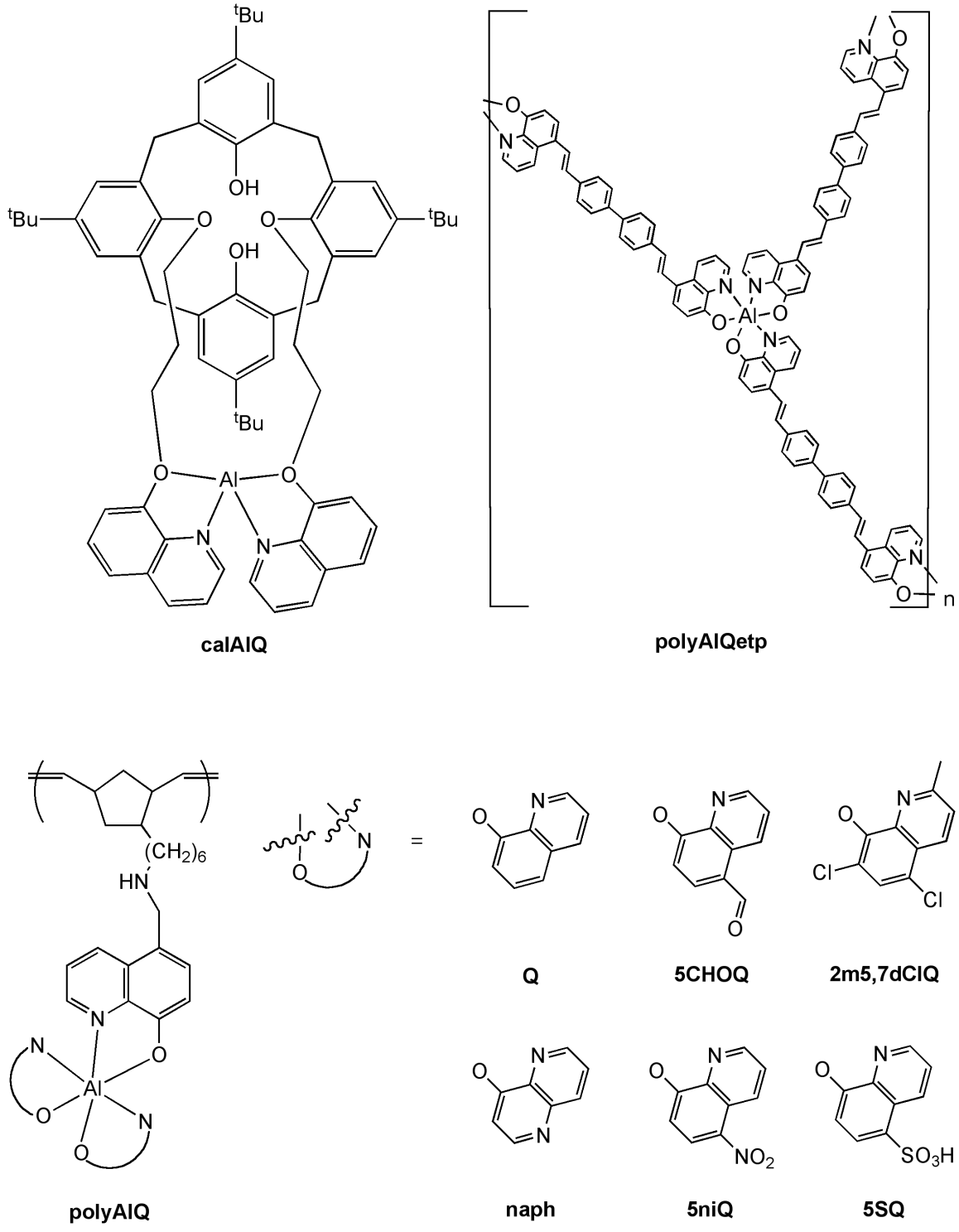

Figure 3.8: Supramolecular and polymeric AlQ_3 derivatives.

Intercalated 8-Hydroxyquinoline Aluminum and Derivatives

Meridional and facial isomers are possible for AlQ_3 and theoretical calculations predict that the facial isomer should exhibit emission that is blue-shifted from the green emission of the meridional isomer.[87,129] The α, β, and γ phases of AlQ_3 consist of the meridional isomer, However, the facial isomer, δ-AlQ_3, is formed when α-AlQ_3 is annealed at 390 °C for 6 hours.[130] The molecules are packed in δ-AlQ_3 in a way that minimizes the π-orbital overlap between ligands that belong to neighboring molecules. In the case of weak π-orbital overlap between neighboring molecules, there is no evidence for extended interactions. This effect is thought to be responsible for the blue-shift in photoluminescence.

Porous alumina can be prepared in a honeycomb array with holes on the nanometer scale that can be used to prepare nanometer-sized particles.[131] When porous alumina impregnated with AlQ_3 was prepared via anodization in sulfuric acid, pore sizes of 10-15 nm were observed.[132] When the same preparation was carried out in oxalic acid, pore sizes of 40-50 nm were observed. The photoluminescence peaks were evident at 488 nm and 510 nm for the materials that were prepared in sulfuric acid and oxalic acid, respectively. The photoluminescence blue-shift for the material prepared in sulfuric acid is probably caused by the prevention of aggregate formation in 10-15 nm holes. Pure solutions of AlQ_3 display photoluminescence peaks at 512 nm and 490 nm, for 10^{-2} M and 10^{-6} M solutions, respectively. These molecules are more easily packed into 40-50 nm holes, which causes the material prepared in oxalic acid to behave more like the concentrated solution. In the case of 10-15 nm holes, the photoluminescence of AlQ_3 appears more like that of individual monomers, as in the dilute solution.

In a separate study, AlQ_3 embedded in a porous alumina membrane exhibited a photoluminescence maximum at 498 nm, which is blue-shifted with respect to that of an

AlQ_3 thin film by 18 nm.[133] Porous alumina can be annealed in order to reduce oxygen vacancies. Analysis of AlQ_3 embedded in as-prepared porous alumina and annealed porous alumina revealed that the photoluminescence excitation intensity is decreased in the annealed material, thus suggesting that oxygen vacancies are involved in the excitation process. It is possible that carrier photogeneration may occur in oxygen vacancies, while radiative recombination occurs in AlQ_3. Moreover, there is overlap in the energy levels of AlQ_3 films and the energy levels of the oxygen vacancies in porous alumina, thus meeting the conditions necessary to produce Förster energy transfer. Additionally, Förster energy transfer can span several nanometers.[134] In the case of AlQ_3 embedded in porous alumina, Förster energy transfer is the most probable cause of the observed photoluminescence.

Films of AlQ_3 embedded in SiO_2 were prepared by simultaneous condensation of AlQ_3 and SiO_2 onto glass substrates.[135] The photoluminescence maxima tended to blue-shift as AlQ_3 concentration was lowered. A blue-shift of 0.28 eV was observed between 100% and 0.01%. Additionally, the photoluminescence was found to be dependent on the evaporation rate. In the case of a 0.5 vol % AlQ_3 film, a blue-shift was observed in concert with an increase in intensity as the evaporation rate decreased. During the simultaneous condensation, strong local heating may occur due to energy transfer from SiO_2 and AlQ_3 interactions, which causes thermal conversion of the AlQ_3 *mer*-isomer to the *fac*-isomer. Furthermore, the rigid environment of the SiO_2 matrix conserves the *fac*-isomer once condensed. At low AlQ_3 concentrations, the probability for *fac*-conversion increases because there is more energy transfer available per molecule. Additionally, the SiO_2 matrix is denser, which facilitates the conservation of the *fac*-isomer. In order to separate the contributions of *fac*- and *mer*-isomers of AlQ_3, the photoluminescence spectra of a 100% AlQ_3 film and a 0.5 vol % AlQ_3 mixed film excited at 370 nm and 440

nm were recorded. These values fall above and below the excitation maximum of *fac*-AlQ_3.[136] A 100% AlQ_3 sample showed a maximum at 536 nm, independent of excitation wavelength. The 0.5 vol % AlQ_3 mixed film evidenced emission at 465 nm when excited at 370 nm. This emission occurred at 520 nm when excited at 440 nm. These results indicate that the emission from the 0.5 vol % mixed film could be attributed to a green and a blue component. The peak positions of the green and blue components were identified by means of Gaussian fitting so the intensity of each component could be identified in films that had been prepared at various rates. Overall, it was found that the contribution from the blue component increased as the evaporation rate decreased.

An α-zirconium phosphate framework modified by intercalation of *n*-butyl amine in order to increase the interlayer separation has been prepared and has been used as a host framework for AlQ_3.[137] The emission maximum of this assembly, AlQ_3-BAZrP, is blue-shifted to 505 nm while that of an AlQ_3 aqueous solution exhibits an emission maximum at 515 nm. Furthermore, the luminescence intensity was improved 5-fold in comparison with that of the AlQ_3 aqueous solution. Both the AlQ_3-BAZrP assembly and the AlQ_3 aqueous solution show an increase in luminescence intensity as AlQ_3 concentration is increased. However, that of the AlQ_3 aqueous solution is very weak and does not reach a maximum in the range of 10-30 μM, while that of the AlQ_3 assembly is significantly stronger and reaches a maximum at 25 μM. Time-resolved studies were used to examine the time dependence of luminescence for the AlQ_3-BAZrP assembly and the AlQ_3 aqueous solution. Both display biexponential decay, characteristic of a short-lived component and a long-lived component. These two components may be the result of the coexistence of *mer*- and *fac*-isomers. In the AlQ_3 aqueous solution, the short-lived component is major and the long-lived component is minor, with 73% of the luminescence attributed to a 1.47 ns component while 27% of the luminescence comes

from a 13.33 ns component. The opposite is true for the AlQ_3 assembly, in which 82% of the luminescence comes from a 16.89 ns component and 18% of the luminescence is attributed to a 2.32 ns component.

Hybrid materials made from a magnesium-aluminum layered double hydroxide (LDH), dodecyl sulfonate (DDS^-), and an AlQ_3 derivative, tris(8-hydroxyquinoline-5-sulfonate)aluminum anion ($Al(5SQ)_3^{3-}$), shown in Figure 3.9, evidence emission that is blue-shifted from that of the corresponding sodium salt, $Na_3Al(5SQ)_3$.[138] The photoluminescence emission maximum of $Na_3Al(5SQ)_3$ is 495 nm, whereas that of the DDS-$Al(5SQ)_3$(x%)/LDH material (where x is the concentration of $Al(5SQ)_3^{3-}$) is 450 nm. This shift is due to the conversion of the *mer*-isomer to the *fac*-isomer caused by host-guest electrostatic attraction. The intensity increases as the percentage of $Al(5SQ)_3^{3-}$ increases from x = 1.96 to x = 66.67, then it drops off. The decrease in intensity at high $Al(5SQ)_3^{3-}$ concentration is probably due to aggregation via π-π interactions.[139] The stability of the excited state of $Al(5SQ)_3^{3-}$ anions is increased in the hybrid material, as evidenced by longer fluorescence lifetimes compared with those of $Na_3Al(5SQ)_3$. The rigid environment of LDH may reduce the internal mobility of $Al(5SQ)_3^{3-}$ anions, thus preventing nonradiative internal conversion processes.

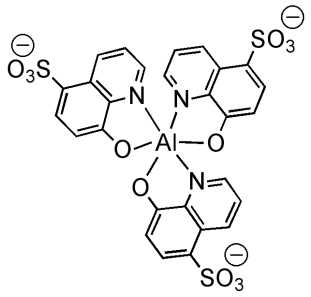

$Al(5SQ)_3^{3-}$

Figure 3.9: $Al(5SQ)_3^{3-}$.

OTHER ALUMINUM BLUE LUMINOPHORS

Aluminum Ester Salen Complexes

Aluminum Schiff-base complexes have received significant attention as catalysts, noteworthy examples include ethylene polymerization and Michael addition reactions.[140] Even though the fluorescence properties for this family of complexes were reported 4 decades ago,[141] few studies have focused on their emission applications, such as their use as luminophors,[142,143] labeling sensors in biological systems,[144] the determination of Al^{3+} traces,[145] and in OLEDs.[143,146] As in the case of AlQ_3 derivatives, modification of the ligands in Al^{3+} Schiff-base complexes can be used to tune the emission wavelength. Appending an ester group to the 5-position of the salicylidene ring on a Schiff-base aluminum complex resulted in bright blue emission. This behavior is not observed for other metal ions or for Schiff-base ligands that lack an ester moiety.[147] The nature of the ester moiety had very little effect on the emission wavelength, which remained in the blue region for all complexes of this family.[77,147] However, the quantum yields varied widely. Initially, Al(ester-salophen)-a, -b, and –c, shown in Figure 3.10, were synthesized and compared with each other. The highest quantum yield observed was 20% for Al(ester-salophen)-c.[147] In order to further explore the effect of chemical modulation, Al(ester-salophen)-d, -e, and -f and Al(ester-salonaph)-c, -d, and -e were synthesized using aromatic ester moieties and varying the extent of the π-system of the ligand backbone.[77] The electron-withdrawing aromatic ester groups increased the quantum efficiency to the greatest extent, reaching 44% for Al(ester-salophen)-f. Extending the π-system of the ligand backbone only served to lower the quantum efficiency. The HOMO-LUMO band gap variation exhibited a narrow band gap range from 2.92-3.16 eV without affecting the emission wavelength. The calculated LUMO levels are nearly constant while those of the HOMO levels are more susceptible to

chemical modification. Increasing the π-system of the ester tends to destabilize the HOMO while increasing the electron-withdrawing nature of the ester R group stabilized the HOMO. However, experimental data derived from redox potentials show that the LUMO is more affected by chemical alteration than the HOMO. The LUMO is stabilized by increasing the electron-withdrawing nature of the esters and by increasing the aromaticity of the ligand backbone. Photoluminescence parameters are displayed in Table 3.16.

Table 3.16: Photoluminescence for aluminum ester salen complexes.

	λ_{PL} (nm)	ϕ_{PL}[c] (%)	HOMO[d] (eV)	LUMO[d] (eV)	E_G[d] (eV)
Al(ester-salophen)-a	478[a]	14	nr	nr	nr
Al(ester-salophen)-b	478[a]	12	nr	nr	nr
Al(ester-salophen)-c	478[a]	20	nr	nr	nr
Al(ester-salophen)-d	484[b]	31	-6.19	-3.08	3.11
Al(ester-salophen)-e	480[b]	40	-6.31	-3.25	3.06
Al(ester-salophen)-f	482[b]	44	nr	nr	nr
Al(ester-salonaph)-c	485[b]	23	-6.20	-3.25	2.95
Al(ester-salonaph)-d	486[b]	22	-6.18	-3.20	2.98
Al(ester-salonaph)-e	482[b]	29	-6.22	-3.30	2.92

[a]measured in DMSO. [b]measured in methanol. [c]determined using quinine sulfate as a standard. nr = not reported.

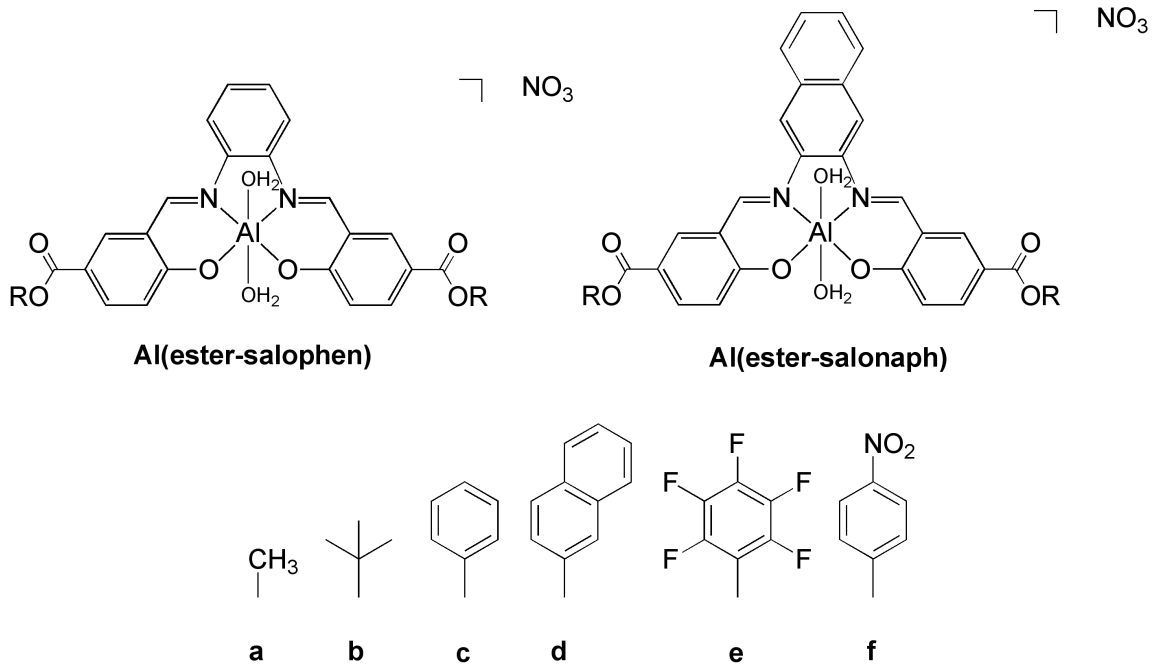

Figure 3.10: Aluminum ester salen complexes.

Aluminum Complexes of the Di-2-Pyridylamine Ligand

The di-2-pyridylamine ligand (dpaH) produces weak emission in the purple-blue region at 420 nm.[71] The formation of dpaH aluminum complexes**,** $Al(CH_3)_2(dpa)$, $Al_2(CH_3)_5(dpa)$, and $Al_4(CH_3)_6(O)_2(dpa)_2$, results in an emission shift to longer wavelengths in the blue region and a significant enhancement of emission efficiency. These complexes produce blue luminescence in solution and the solid state in the range of 445-475 nm with a quantum yield of 37% for $Al_4(CH_3)_6(O)_2(dpa)_2$. The complexes are displayed in Figure 3.11 and the photoluminescent parameters are summarized in Table 3.17. Molecular orbital calculations reveal that the dpaH anion (dpa^-) has a smaller band gap than that of dpaH due to destabilization of the HOMO by the negative charge. This causes dpa^- to emit in the blue region at longer wavelengths than dpaH. The HOMO-LUMO band gaps for dpa^- and $Al(CH_3)_2(dpa)$ are similar. However, the molecular orbitals of $Al(CH_3)_2(dpa)$ are lower in energy than those of dpa^-. It appears that the

aluminum ion stabilizes dpa^- by accepting lone pairs of electrons. In addition to enhanced emission efficiency caused by this stabilization, the bonding to aluminum may also increase the rigidity of dpa^-, reducing energy loss to radiationless thermal vibrations.[148]

The complexes $Al(CH_3)_2(dpa)$ and $Al_2(CH_3)_5(dpa)$ are very air-sensitive, while $Al_4(CH_3)_6(O)_2(dpa)_2$ is stable for a few hours in air. However, it is not volatile and therefore devices cannot be fabricated by vacuum deposition. A fluorinated ligand in which one pyridyl ring of dpaH is replaced by a pentafluorophenyl group (pfapH) was synthesized in an attempt to improve the stability of these complexes. The electron-withdrawing nature of the pentafluorophenyl group may decrease the electron density on the amido nitrogen, thus stabilizing complexes made with this modified ligand. An aluminum complex made with pfapH, $Al(pfap)_3$, is relatively stable. However, the emission energy of $Al(pfap)_3$ is shifted to the UV region at 409 nm.

Table 3.17: Photoluminesence parameters for aluminum complexes of di-2-pyridylamine and derivatives.

	λ_{PL}[a] (nm)	ϕ_{PL}[b] (%)
$Al(CH_3)_2(dpa)$	475	nr
$Al_2(CH_3)_5(dpa)$	445	nr
$Al_4(CH_3)_6(O)_2(dpa)_2$	450	37
$Al(pfap)_3$	409	nr

[a]measured in the solid state. [b]relative to 9,10-diphenylanthracene. nr = not reported.

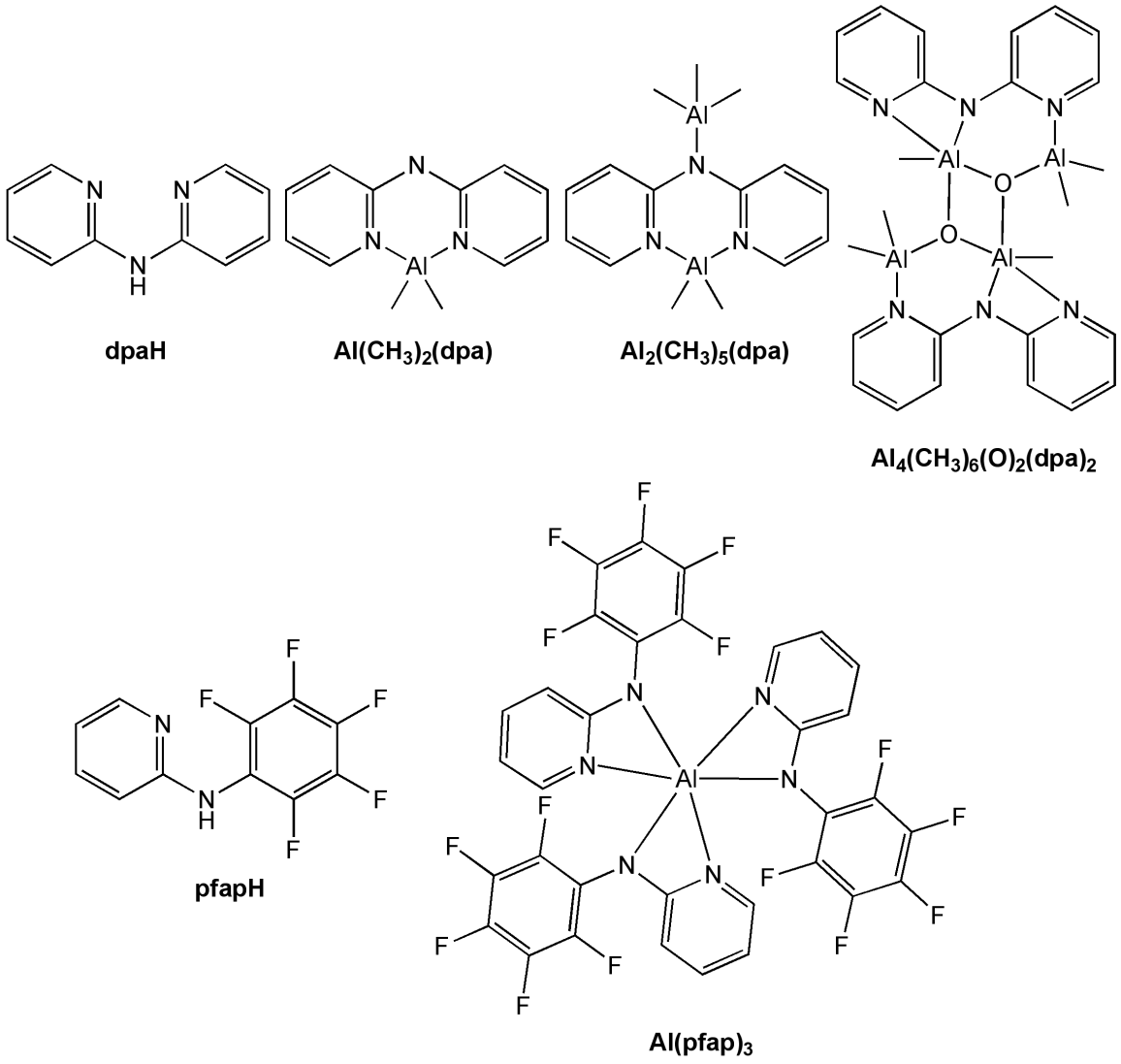

Figure 3.11: Aluminum complexes of di-2-pyridylamine and derivatives.

Aluminum Complexes of the 7-Azaindole Ligand

The reaction of $Al(CH_3)_3$ with 7-azaindole (7azaH) produces two compounds, $Al_2(CH_3)_4(7aza)_2$ and $Al_2(CH_3)_2(7aza)_4$, depending on the reaction stoichiometry.[73] The equimolar reaction produces $Al_2(CH_3)_4(7aza)_2$ while the reaction of aluminum with two equivalents of ligand produces $Al_2(CH_3)_2(7\text{-}aza)_4$. $Al_2(CH_3)_2(7aza)_4$ exhibits greater stability toward air, possibly due to the increased number of ligands on the aluminum

centers, thereby reducing the electron density on the metal and thus stabilizing the Al-methyl bond. Both compounds emit intensely in the blue region, at 430 nm and 442 nm in the cases of $Al_2(CH_3)_4(7aza)_2$ and $Al_2(CH_3)_2(7aza)_4$, respectively. The free ligand, however, has no observable emission in the solid state and emits in the UV region at 357 nm in solution. The addition of oxo and alkoxo ligands, as displayed in $Al_2(CH_3)(7aza)_2(\mu\text{-}OCH(CF_3)_2)$ $(OCH(CF_3)_2)_2$, $Al_3(CH_3)(\mu_3\text{-}O)(7aza)_4(OCH(CF_3)_2)_2$, and $Al_4(\mu_3\text{-}O)_2(7aza)_6(OCH(CF_3)_2)_2$, increase the stability of the compounds while not significantly altering the blue luminescence. The complexes are displayed in Figure 3.12 and the photoluminescent maxima are summarized in Table 3.18. Similar to the case of dpaH and the resulting aluminum complexes, the shift in emission to longer wavelength from the 7azaH ligand to the compounds may be due to ligand deprotonation. To further explore the emission of these compounds, molecular orbital calculations were conducted. Both the HOMO and LUMO of the 7azaH anion ($7aza^-$) are higher in energy than those of 7azaH. However, the increase in the HOMO energy level is greater than the increase in LUMO energy level due to increased electron repulsion. The anion is less stable and has a smaller HOMO-LUMO band gap than 7azaH. When bonded to aluminum, stabilization of both the HOMO and LUMO is observed, but the band gap is not significantly affected. This indicates that the role of aluminum is to provide increased stability to the compounds while promoting blue luminescence. The emission quantum yield for $Al_2(CH_3)_2(7aza)_4$ is 54%. Due to the poor stability of $Al_2(CH_3)_4(7aza)_2$, the emission quantum yield is not reported. The bridging 7-aza^- ligands of $Al_2(CH_3)_2(7aza)_4$ are rigid, perhaps causing increased emission efficiency by reducing energy loss to radiationless thermal vibrations.[148]

The reaction of excess 7azaH with $Al(CH_3)_3$ results in the formation of the mononuclear complexes $Al(CH_3)(7aza)_2(7azaH)$ and $Al(7aza)_3(7azaH)$, despite the

bridging tendency of the ligand.[149] When hexafluoroisopropanol is added, the mononuclear complex Al(7aza)(7azaH)OCH(CF_3)$_2$)$_2$ is obtained. The emission peaks range from 430 to 448 nm. The complexes are displayed in Figure 3.12 and the photoluminescence is summarized in Table 3.18. These maxima are in the same energy region as those of dinuclear and polynuclear aluminum 7azaH compounds. The emission efficiencies of the mononuclear complexes are similar to those of the dinuclear and polynuclear compounds, despite the fact that the high efficiencies of dinuclear and polynuclear compounds were attributed to the bridging nature of $7aza^-$. Intramolecular hydrogen bonding between $7aza^-$ and 7azaH ligands in the mononuclear complexes may have the same effect as the bridging nature of $7aza^-$ in the dinuclear and polynuclear compounds, thereby inducing rigidity that may reduce energy loss to radiationless thermal vibrations. The mononuclear complexes are more stable toward air and moisture than dinuclear and polynuclear Al 7azaH compounds.

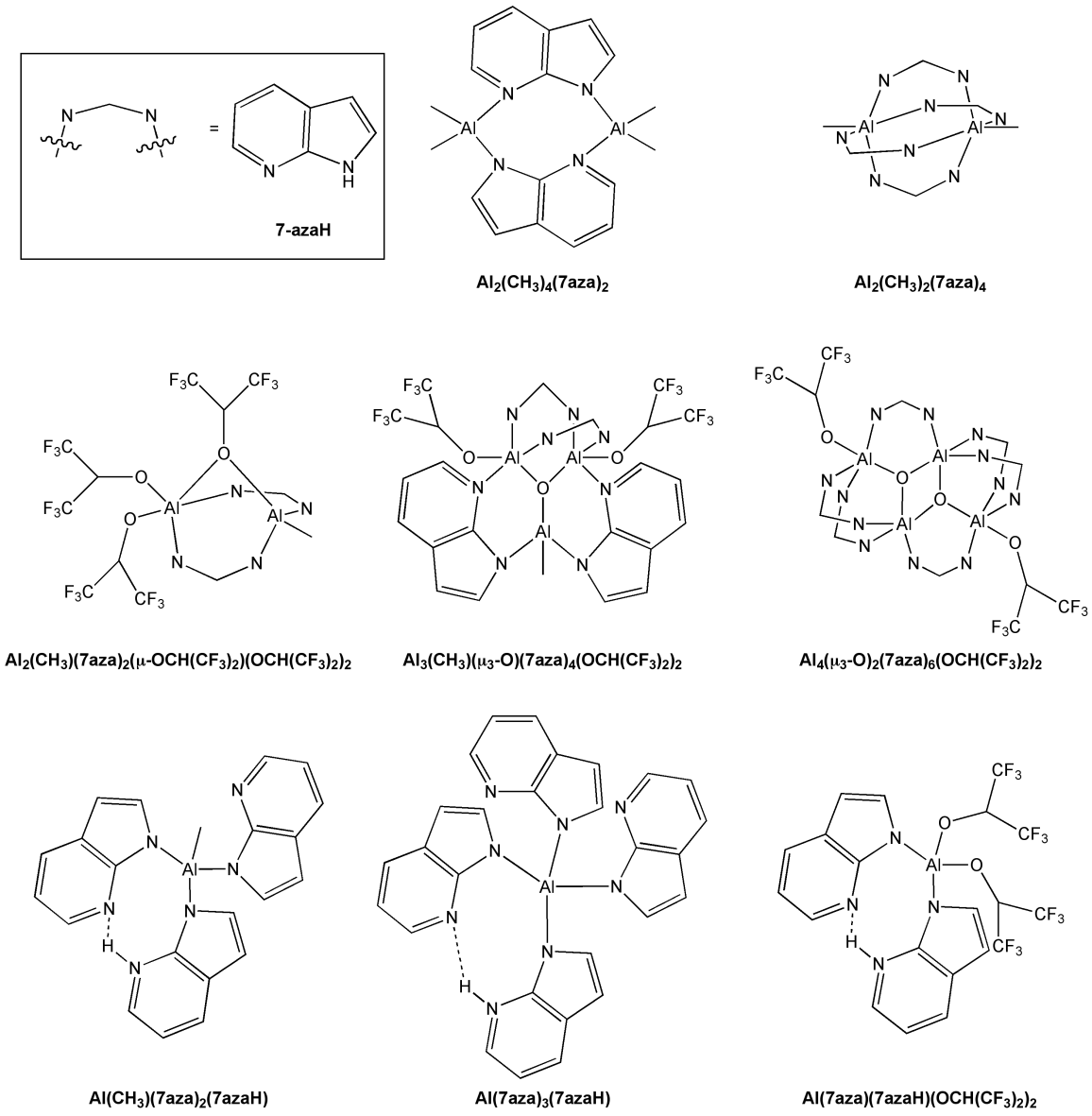

Figure 3.12: 7-azaindole aluminum complexes.

Modification of the 7-azaindole ligand at the 2-position to include an electron-donating methyl group or an electron-withdrawing phenyl group resulted in the formation of two new ligands, 2m7azaH and 2p7azaH, and three new aluminum compounds $Al(CH_3)(2p7aza)_2(2p7azaH)$, $Al_3(CH_3)_3(\mu_3\text{-}O)(2p7aza)_4$, and $Al_3(CH_3)_3(\mu_3\text{-}O)(2m7aza)_4$ when treated with $Al(CH_3)_3$.[150] These complexes are displayed in Figure 3.13. The

complex $Al_3(CH_3)_3(\mu_3\text{-}O)(2p7aza)_4$ has an emission peak at 443 nm, which is longer than the emission peak of $Al_3(CH_3)(\mu_3\text{-}O)(7aza)_4(OCH(CF_3)_2)_2$, due to the electron–accepting character of the phenyl group. The complex $Al_3(CH_3)_3(\mu_3\text{-}O)(2m7aza)_4$ has an emission peak at 431 nm, which is very similar to that of $Al_3(CH_3)(\mu_3\text{-}O)(7aza)_4(OCH(CF_3)_2)_2$, thus indicating that the methyl group had very little effect on the emission energy. The complexes $Al(CH_3)(2p7aza)_2(2p7azaH)$ and $Al_3(CH_3)_3(\mu_3\text{-}O)(2p7aza)_4$ displayed very weak emission, while $Al_3(CH_3)_3(\mu_3\text{-}O)(2m7aza)_4$ had a quantum yield of 31%, similar to that of $Al_3(CH_3)(\mu_3\text{-}O)(7aza)_4(OCH(CF_3)_2)_2$. The weak emission of $Al(CH_3)(2p7aza)_2(2p7azaH)$ and $Al_3(CH_3)_3(\mu_3\text{-}O)(2p7aza)_4$ could be due to the increased thermal vibrations caused by the phenyl group that result in radiationless loss of energy. Additionally, the π orbitals of the phenyl group may intercept electrons transitioning from the excited state, thus quenching the emission. Photoluminescence data are summarized in Table 3.18.

The 7-azaindole ligand is only capable of bridging and terminal binding to the metal center.[151] However, the use of chelating ligands such as acetylacetonato often provide increased stability and volatility to metal complexes. A 7azaH derivative including an acetylacetonato moiety, 1-*N*-7-azaindolyl-1,3-butanedione (acacazaH), has been synthesized. The ligand alone exhibits a weak and broad emission band at 420 nm in the solid state and at 429 nm in solution with an emission efficiency of 0.68%. An aluminum complex of acacazaH, $Al(CH_3)(acacaza)_2$, shown in Figure 3.13, exhibits significantly brighter emission at 460 nm in solution. However, due to poor stability, the quantum yield was not measured. The photoluminescent parameters are displayed in Table 3.18.

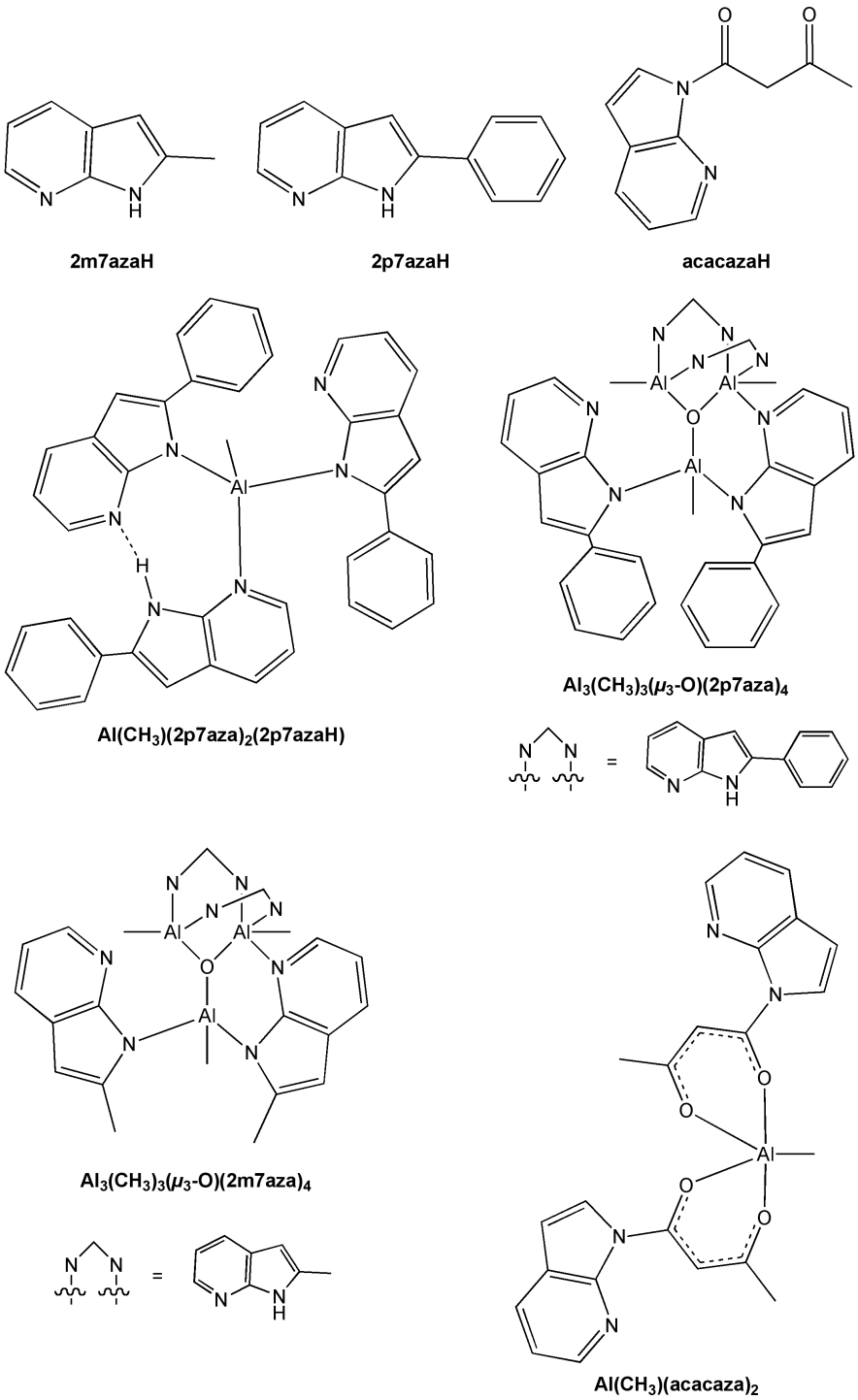

Figure 3.13: 7-azaindole derivatives and aluminum complexes.

Table 3.18: Photoluminescence of aluminum complexes of 7-azaindole and derivatives.

	λ_{PL} (nm)	ϕ_{PL}[c] (%)
$Al_2(CH_3)_4(7aza)_2$	430[a]	nr
$Al_2(CH_3)_2(7aza)_4$	442[a]	54
$Al_2(CH_3)(7aza)_2(\mu\text{-}OCH(CF_3)_2)\ (OCH(CF_3)_2)_2$	430[a]	nr
$Al_3(CH_3)(\mu_3\text{-}O)(7aza)_4(OCH(CF_3)_2)_2$	430[a]	32
$Al_4(\mu_3\text{-}O)_2(7aza)_6(OCH(CF_3)_2)_2$	420[a]	nr
$Al(CH_3)(7aza)_2(7azaH)$	445[a]	nr
$Al(7aza)_3(7azaH)$	448[a]	nr
$Al(7aza)(7azaH)OCH(CF_3)_2)_2$	430[a]	nr
$Al(CH_3)(2p7aza)_2(2p7azaH)$	450[a]	nr
$Al_3(CH_3)_3(\mu_3\text{-}O)(2p7aza)_4$	443[a]	nr
$Al_3(CH_3)_3(\mu_3\text{-}O)(2m7aza)_4$	431[a]	31
$Al(CH_3)(acacaza)_2$	460[b]	nr

[a]measured in the solid state. [b]measured in a dichloromethane solution. [c]relative to 9,10-diphenylanthracene. nr = not reported.

Other Aluminum Blue Luminophors

A CHEF effect[152] (Chelation Enhancement of Fluorescence Emission) is observed for the ligand 1,1,1,1-tetrakis[(2-salcylaldiminomethyl)]methane (H_4TSM) when coordinated to aluminum to form Al(HTSM), shown in Figure 3.14.[75] While the ligand alone has no emission, a photoluminescence maximum is observed at 433 nm in acetonitrile at room temperature for Al(HTSM). A 1:0.92 ratio of ligand and aluminum is found when a H_4TSM solution is fluormetrically titrated with an $AlCl_3$ solution until saturation occurs. This confirms the mononuclear nature of Al(HTSM). When titrated with d^{10} metal ions and first row transition metal ions (Zn^{2+}, Cd^{2+}, Hg^{2+}, Pb^{2+}, Cu^{2+}, Ni^{2+}, and Co^{2+}), Al(HTSM) acts as a zinc sensor. Titration data are summarized in Table 3.19. Zinc sensing has become an area of great interest in the last decade due to the essential role of zinc in many biological enzymes and substrates.[153] For example, zinc uptake disruption may lead to amyloid plaque formation in Alzheimer's disease.[154] Due to the heavy ion effect,[155] Cd^{2+}, Hg^{2+}, and Pb^{2+} quench emission intensity without changing the

emission wavelength. Titrations with Cu^{2+}, Ni^{2+}, and Co^{2+} also lead to emission quenching. The emission intensity of Al(HTSM) is increased 1.64 times when titrated with 0.31 equivalents of Zn^{2+}. Additionally, a 5 nm red-shift is observed. A weak coordination between three molecules of Al(HTSM) and one Zn^{2+} ion may occur, most likely interacting through the uncoordinated salicylaldimine moieties of Al(HTSM).

Table 3.19: Photoluminescence of Al(HTSM) titrated with d^{10} metal ions and first row transition metal ions.

	λ_{PL} (nm)	ϕ_{PL} (%)
Al(HTSM)	433	0.2
Al(HTSM) + Zn^{2+}	438	0.3
Al(HTSM) + Cd^{2+}	433	0.18
Al(HTSM) + Hg^{2+}	440	0.12
Al(HTSM) + Pb^{2+}	433	0.08
Al(HTSM) + Cu^{2+}	433	0.13
Al(HTSM) + Ni^{2+}	434	0.15
Al(HTSM) + Co^{2+}	432	0.19

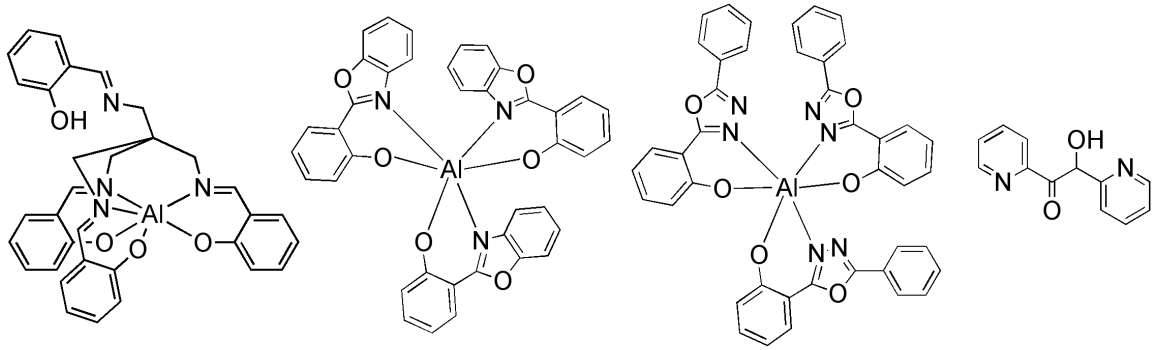

Figure 3.14: Al(HTSM), $Al(THB)_3$, $Al(ODZ)_3$, and the α-pyridoin ligand.

One cause of decreased device efficiency and lifetime is a poor balance between electron and hole currents.[69] In most organic materials, holes have higher mobility than

electrons and can travel through the hole-transporting layer to the electron-transporting layer and then to the cathode without hole-electron recombination in the emission layer.[156] A hole-blocking layer between the emission layer and electron-transporting layer can be added to improve efficiency and color purity by promoting hole-electron recombination in the emission layer. However, increasing the number of layers in a device would increase production costs. Additionally, adding a hole-blocking layer in the electron-transporting layer has been shown to significantly increase operating voltage.[157] Organic materials that function as both electron-transporters and hole-blockers exist, but are rare. Due to low glass transition temperatures, these materials have poor thermal stability and can crystallize easily, causing decreased device performance and lifetime. An electron-transporting and hole-blocking aluminum complex, tri-(2-(2-hydroxyphenyl) benzoxazole) aluminum ($Al(THB)_3$), shown in Figure 3.14, has been synthesized in good yield via a single step reaction.[69] $Al(THB)_3$ shows a deep blue emission at 412 nm in common organic solvents and at 421 nm as a film with a fluorescence quantum yield of 14% for a dichloromethane solution. The HOMO energy level is 6.2 eV, as determined by UPS. The LUMO energy level is 3.2 eV, as determined by the HOMO energy level and the optical absorption edge. In devices, $Al(THB)_3$ functions as an electron-transporting material. The HOMO energy level of $Al(THB)_3$ is close to that of known hole-blockers, so it is expected to be an efficient hole-blocking material also.

Several metal-chelate complexes exhibiting electron-transport abilities and light emission contain aromatic ligands with a phenolic oxygen and a doubly bound nitrogen chelated to the metal center.[158] The polycyclic aromatic ligand, oxadiazole (ODZ), was complexed to aluminum and displayed blue emission at 447 nm with CIE coordinates of (0.16, 0.17) and a quantum efficiency of 1.7%. The Al complex $Al(ODZ)_3$ is displayed in Figure 3.14. However, devices made using these materials as the emission layer had

short lifetimes, with electroluminescent intensity nearing zero at 10 hours. This degradation may be caused by instability of the excited state of these molecules.

The reaction of α-pyridoin and aluminum (III) chloride hexahydrate results in a blue-green emitting complex, PAl.[68] The ligand alone does not produce luminescence due to nonradiative deactivation of the excited species by torsional motion around the central carbon-carbon double bond. When complexed to aluminum, however, blue-green light emission is observed at 410 nm. The structure of this complex is estimated to be $Al_4(\alpha\text{-pyridoin})_3(H_2O)_8$ using FT-IT, UV-Vis, and XPS spectra. The ligand alone has a keto-enol tautomer structure, with the enol form favored. The enol form is converted to the keto form when complexed to aluminum. A device fabricated by vacuum deposition using PAl as the emission layer displayed blue-green emission at 480 nm. The ligand is displayed in Figure 3.14.

CONCLUSIONS

The ability to tune emission by chemical modification of luminophors is key to achieving emission that spans the visible region. While an increasingly large number of blue luminophors is known, further work is needed to achieve efficient, pure blue emission from a complex that is easily processed for device fabrication.

Chapter 4: Synthesis, Photophysical Properties, and Electropolymerization of an Ester-Functionalized Salophen Aluminum Complex Exhibiting Blue Emission

ESTER-FUNCTIONALIZED SALOPHEN ALUMINUM BLUE LUMINOPHORS

Emission Wavelength and Efficiency of Monomers

Salen ligands such as salophen (*N*,*N*'-bis(salicylidene)-phenylenediamine) are prepared easily via condensation of a diamine and two equivalents of salicylaldehyde. These ligands are capable of coordinating a variety of metal ions and the resulting complexes have several applications in the field of catalysis. However, only a few studies have focused on the emissive properties of these complexes. Recently, the series of ester-functionalized salophen aluminum complexes shown in Figure 4.1 were reported and found to exhibit bright blue emission.[77,147] Emission of this type was not observed in the case of a non-functionalized salophen aluminum complex or for ester-functionalized salophens coordinated to other metals. The wavelength maxima for these complexes were found to be independent of structural modification. The room temperature luminescence spectra for all of the complexes exhibit a large band with maxima between 478 and 486 nm, thus implying that the emissions are salophen-centered. However, there was considerable variation in the quantum yields. The use of electron-withdrawing ester R groups resulted in enhanced emission efficiencies, which reached 44% in the case of Al(ester-salophen)-f. Each Al(ester-salonaph) complex displayed a lower efficiency than that observed for the corresponding Al(ester-salophen) complex.

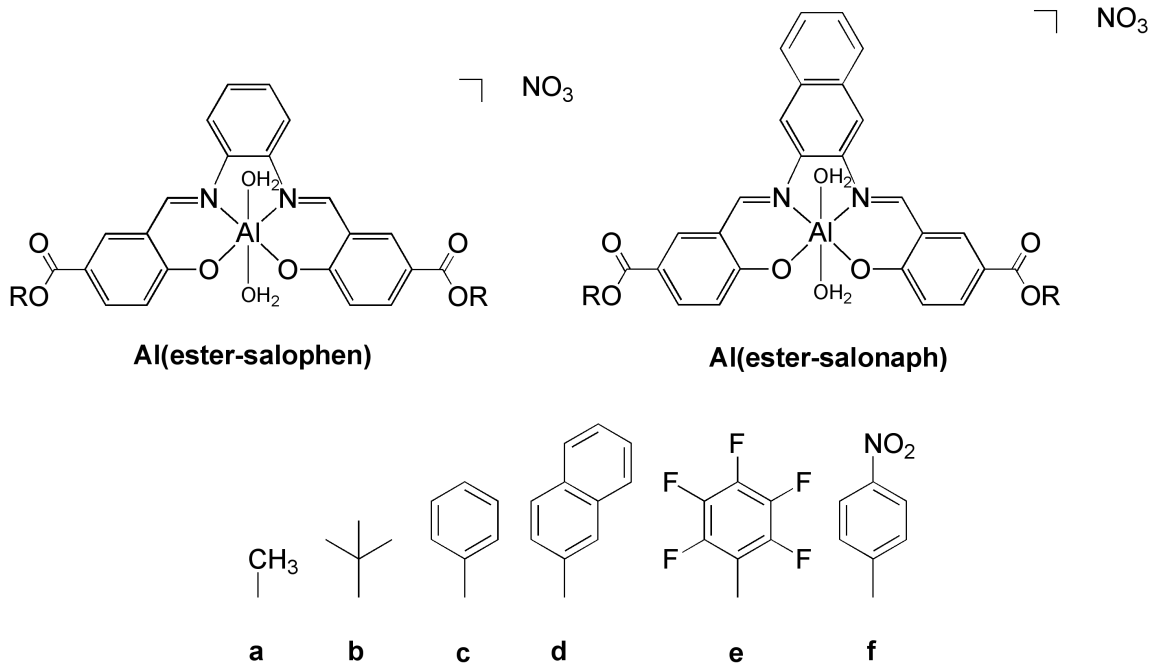

Figure 4.1: Ester-functionalized salophen aluminum complexes.

Research Objectives

The ability to maintain luminescence in the blue range while tuning the emission efficiency has been demonstrated for a series of ester-functionalized salophen aluminum complexes that feature a variety of ester R groups. However, none of these complexes were amenable to polymerization. The synthesis of a polymeric ester-functionalized salophen aluminum complex is of considerable interest due to the advantages offered by polymers of this type, such as ease of processing and uniformity of resulting films.[159] Moreover, in addition to tuning emission efficiency, chemical modification of the ester R groups may be useful for designing complexes with additional capabilities such as polymerizability. Accordingly, the ester-functionalized salophen ligand, 4-(2,2'-bithiophen-5-yl)phenyl ester salo-dihexyl-phen (**L**), was designed to incorporate a polymerizable bithiophene as the ester R group. Furthermore, two hexyl groups were appended to the phenyl backbone, overcoming anticipated solubility issues. The ligand

was treated with dimethylaluminum chloride to afford the complex 4-(2,2'-bithiophen-5-yl)phenyl ester salo-dihexyl-phen aluminum chloride (**Al L**). Both **L** and **Al L** were electropolymerized, thereby producing polymers **poly-L** and **poly-Al L**. Since **Al L** and **poly-Al L** contain an ester functionalized salophen aluminum core, they were anticipated to exhibit blue emission in concert with previously synthesized complexes in the series.

RESULTS AND DISCUSSION

Synthesis and Characterization of a Polymerizable Ester-Functionalized Salophen Aluminum Complex

The ligand 4-(2,2'-bithiophen-5-yl)phenyl ester salo-dihexyl-phen (**L**) was synthesized as described in Scheme 4.1. The esterification of 3-formyl-4-hydroxybenzoic acid with 4-bromophenol proceeded via a DCC-mediated pathway and resulted in the formation of a crude yellow solid that was purified by column chromatography, thereby producing **1** as a pure, white solid in 55% yield. Stille coupling of **1** with 1.1 equivalents of 2-(tributylstannyl)bithiophene in the presence of palladium resulted in the formation of **2** as a yellow powder, which was purified by column chromatography in 47% yield. Further purification was achieved by recrystallization from hot toluene. Crystals suitable for X-ray diffraction were grown by slow evaporation of a methylene chloride (DCM) solution. The resulting structure is displayed in Figure 4.2. Details of the data collection, structure solution and refinement are compiled in Table A4.1 and selected metrical parameters are listed in Tables A4.2 and A4.3. Condensation of **2** with half an equivalent of 1,2-diamino-4,5-dihexylbenzene resulted in the formation of **L** as a yellow powder that was isolated in 79% yield by means of filtration. The identities of **1**, **2**, and **L** were confirmed on the basis of ^{1}H and $^{13}C\{^{1}H\}$ NMR spectroscopy, mass spectrometry, melting point and elemental analysis.

Furthermore, the solid state structure of **2** was determined by single-crystal X-ray diffraction analysis and **L** was characterized by means of infrared spectroscopy.

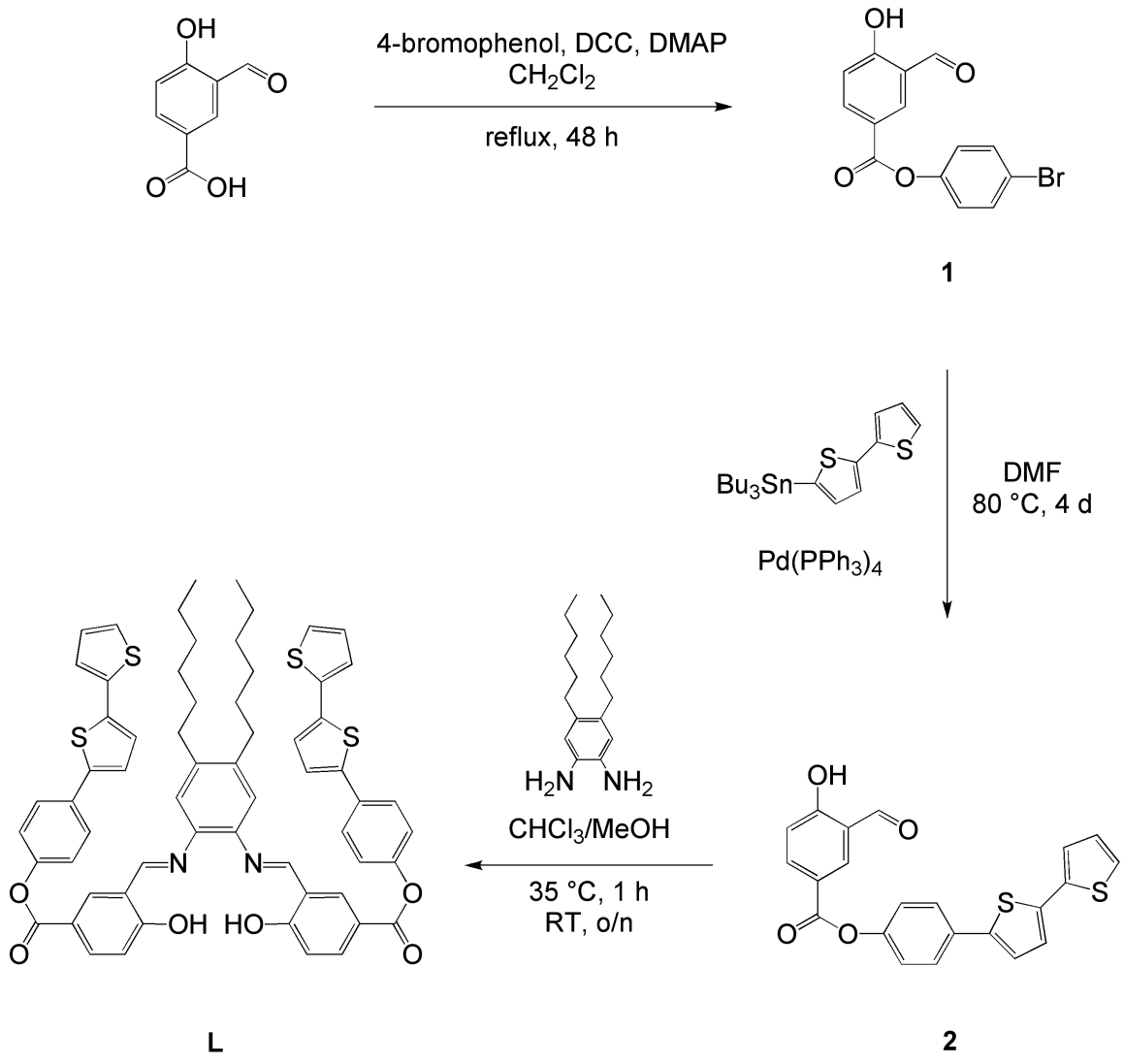

Scheme 4.1: Synthesis of 4-(2,2'-bithiophen-5-yl)phenyl ester salo-dihexyl-phen.

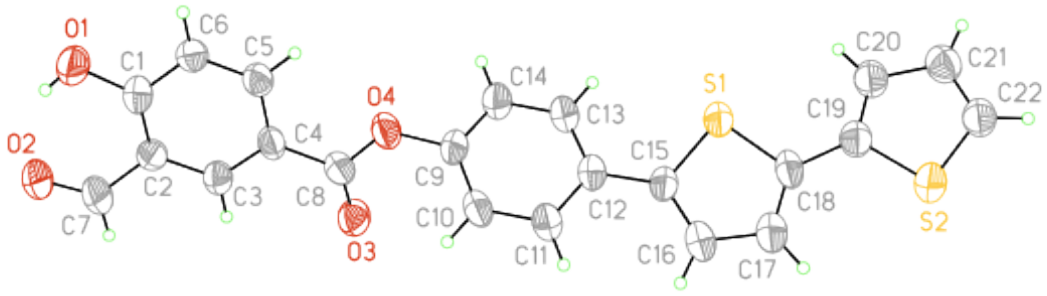

Figure 4.2: Molecular structure of 4-(2,2'-bithiophen-5-yl)phenyl ester salcylaldehyde.

The aluminum containing monomeric 4-(2,2'-bithiophen-5-yl)phenyl ester salo-dihexyl-phen aluminum chloride (**Al L**) was synthesized in 89% yield in the absence of air and moisture via the reaction of **L** with dimethylaluminum chloride in toluene solution at 65 °C (See Scheme 4.2). The product was isolated by means of filtration. The structure and composition of **Al L** were confirmed on the basis of ^{1}H and $^{13}C\{^{1}H\}$ NMR spectroscopy, mass spectrometry, melting point and infrared spectroscopy.

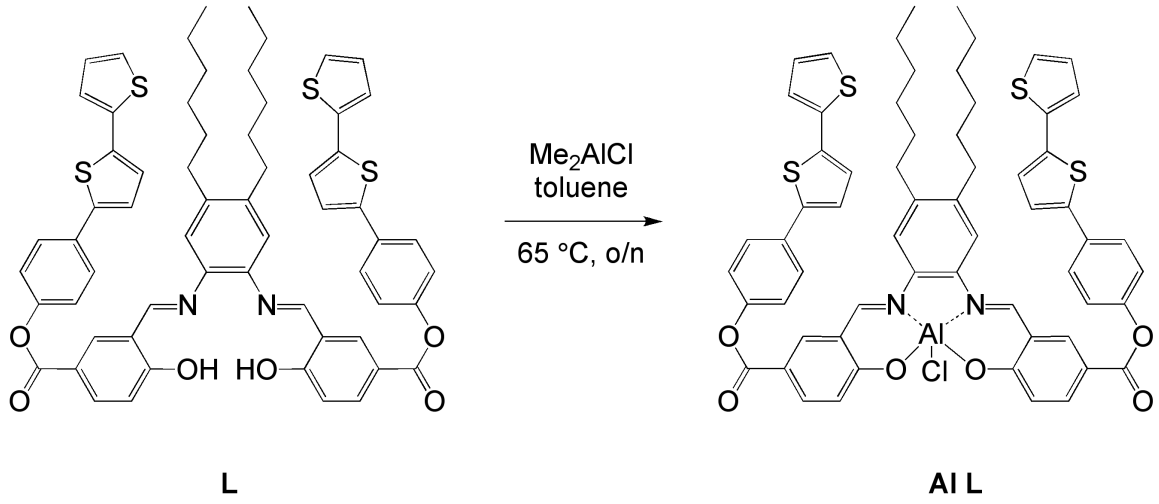

Scheme 4.2: Synthesis of 4-(2,2'-bithiophen-5-yl)phenyl ester salo-dihexyl-phen aluminum chloride.

Spectroscopic Properties of the Ligand and Aluminum Complex

The spectroscopic properties of **L** and **Al L** were studied under a variety of conditions and the data from these studies are summarized in Table 4.1. The UV-vis absorption spectra of **L** and **Al L** in DCM solution (see Figure 4.3), exhibit high-energy bands at 257 and 259 nm, respectively along with additional bands at 343 and 342 nm, respectively. These peaks are attributed to π to π* intra-ligand transitions, which are similar to those of previously reported ester-functionalized salophen aluminum complexes.[147] However, the complex displays an additional low-energy shoulder centered at 430 nm, which is attributable to singlet charge transfer involving the metal. The ambient temperature excitation spectra of **L** and **Al L** in dimethyl sulfoxide (DMSO) solution are presented in Figure 4.4. Both **L** and **Al L** exhibit broad excitation peaks similar to those of the corresponding absorption peaks.

Table 4.1: UV-vis absorption and photoluminescence data for **L** and **Al L**.

	Absorbance[a] λ_{max}, nm (ε, M^{-1} cm^{-1})	Excitation[b] λ_{max} (nm)	Emission λ_{max} (nm)	τ (μs)	ϕ[b] (%)
L	257 (89848) 343 (94844)	340	523[b] 447[b] 515[c]	7.223 ± 0.7612[b] 5.887 ± 0.4814[c]	0.532 ± 0.0125
Al L	259 (56215) 342 (77110) 430 (21335)	359	491[b] 480[c]	9.340 ± 0.9700[b] 9.892 ± 0.1546[c]	8.19 ± 0.158

[a]measured in DCM at room temperature. [b]measured in DMSO at room temperature.
[c]measured in MTHF at 77 K.

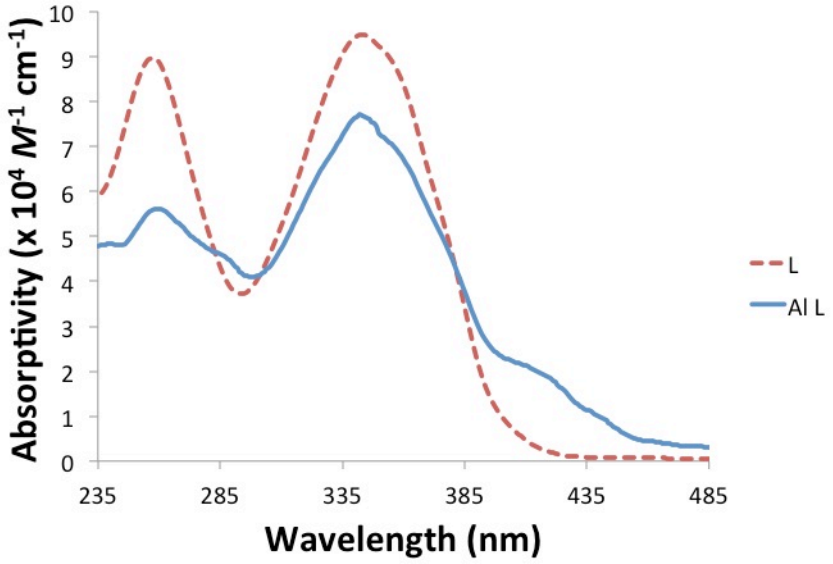

Figure 4.3: UV-vis absorption spectra for **L** and **Al L** in DCM solution at room temperature.

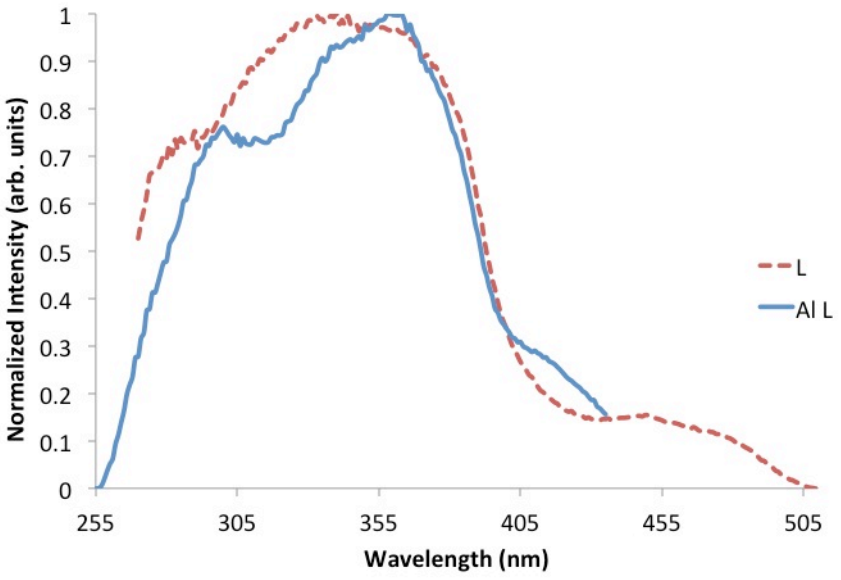

Figure 4.4: Excitation spectra for **L** and **Al L** in DMSO solution at room temperature.

The emission spectra of **L** and **Al L** excited at 345 nm were recorded in a 2-methyltetrahydrofuran (MTHF) glass and at ambient temperature in DMSO and are displayed in Figure 4.5. The emission spectra of **Al L** display a blue-shift with respect to that of **L** at both ambient and low temperature. Images of **L** and **Al L** in DCM solution excited by a long wave ultraviolet lamp are presented in Figure 4.6. The emission maxima for both **L** and **Al L** are slightly blue-shifted on changing from ambient temperature to low temperature. This observation is indicative of charge transfer, which is typically broad and featureless and relatively red-shifted. In frozen solutions, no solvent reorganization is possible to stabilize the dipole resulting from charge transfer. This inability to achieve stabilization at low temperature results in a small blue-shift in comparison with ambient temperature solutions in which the dipoles can be stabilized by solvent reorganization.

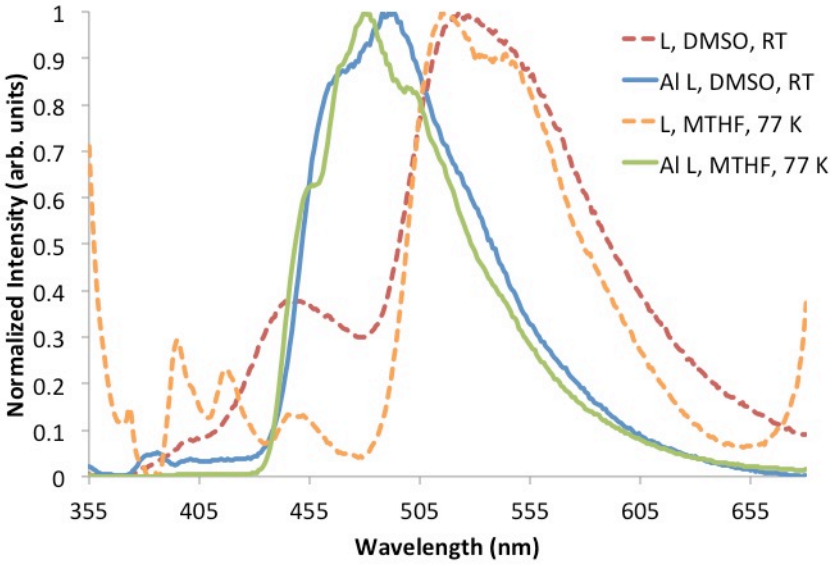

Figure 4.5: Emission spectra for **L** and **Al L** in DMSO at room temperature and in MTHF at 77 K.

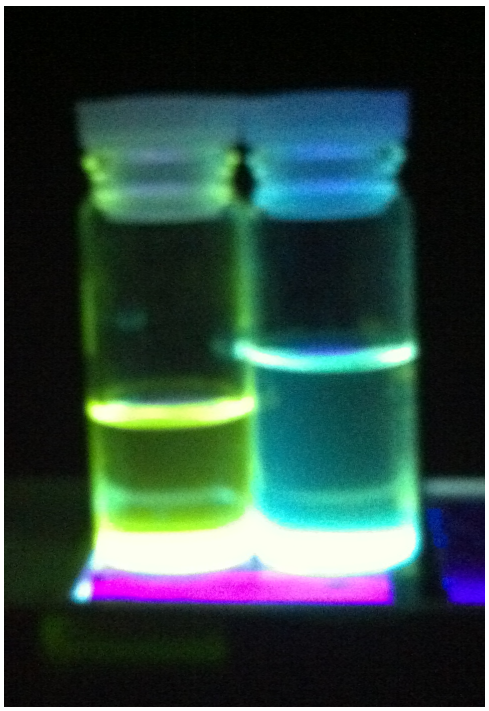

Figure 4.6: DCM solutions of **L** (left) and **Al L** (right) irradiated with long wave UV light.

Concentration and solvent dependency studies were undertaken in order to explore the nature of the emission peak of **L** at 523 nm. The emission spectra pertinent to the concentration study were recorded in DCM solution as a series of concentrations ranging from 2.8 x 10^{-6} to 1.6 x 10^{-5} *M*, as shown in Figure 4.7. Keeping the concentration approximately equal, the emission spectra were recorded in solvents with dielectric constants ranging from 2.4 to 37.5. The emission maximum remained constant as the concentrations were varied, indicating that this peak is not due to excimer formation. However, this peak was sensitive to change of solvent as shown by a 24 nm shift displayed in Figure 4.8. This observation is indicative of charge transfer. The dipole resulting from charge transfer is stabilized to varying extent as the polarity of the

solvent changes. This conclusion is in agreement with the changes observed in the room temperature and low temperature spectra that were discussed previously.

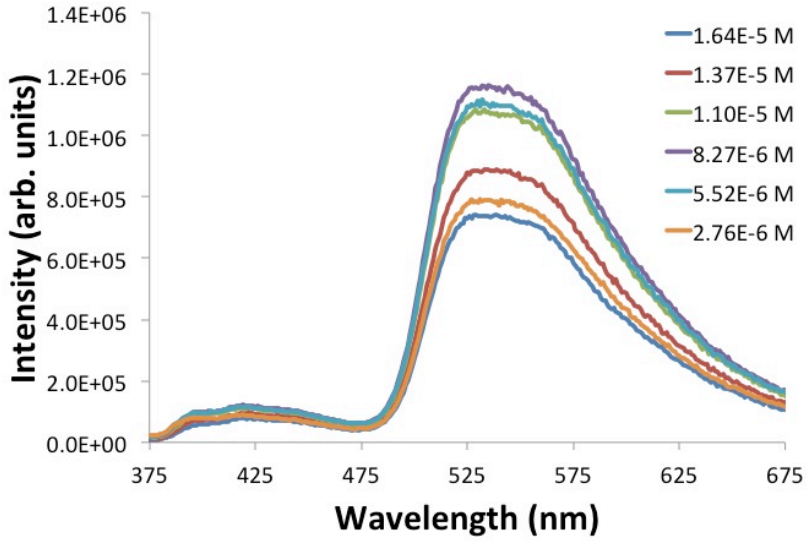

Figure 4.7: Concentration dependency of the emission of **L** in DCM solution at room temperature.

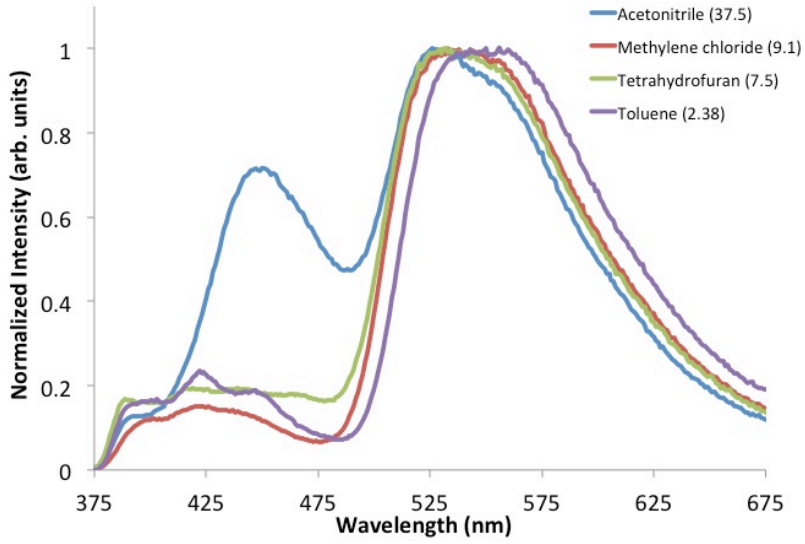

Figure 4.8: Solvent dependency of the emission of **L** at room temperature.

Figure 4.9 shows the emission spectrum of **L** excited at 365 nm and recorded at 77 K in a solution of ethyl iodide:ether:ethanol:toluene in a 2:2:1:1 ratio (EEET). This solution is known to promote population of the triplet excited state in organic molecules.[160] This effect renders phosphorescence more probable and results in the enhancement of phosphorescent peaks. The emission peak of **L** at 461 nm, which is blue-shifted with respect to the charge transfer peak, is therefore attributable to phosphorescence.

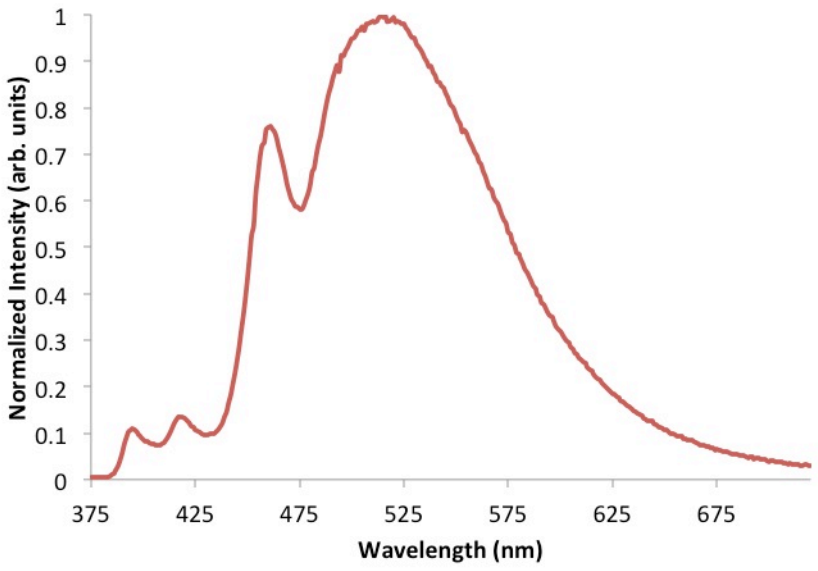

Figure 4.9: Emission spectrum of **L** in EEET at 77 K.

The quantum yield for **Al L** is 8.19%, which is significantly enhanced with respect to that of **L** (0.532%). Although the quantum yield of **Al L** is lower than that of previously reported ester-functionalized salophen aluminum complexes,[77,147] the anticipated increase in quantum yield between the ligand and the aluminum complex was observed.

Electropolymerization of the Ligand and Aluminum Complex

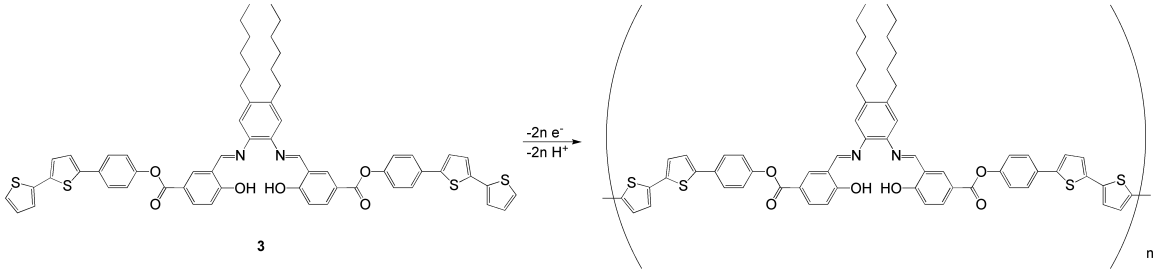

Scheme 4.3: Electropolymerization of the ligand.

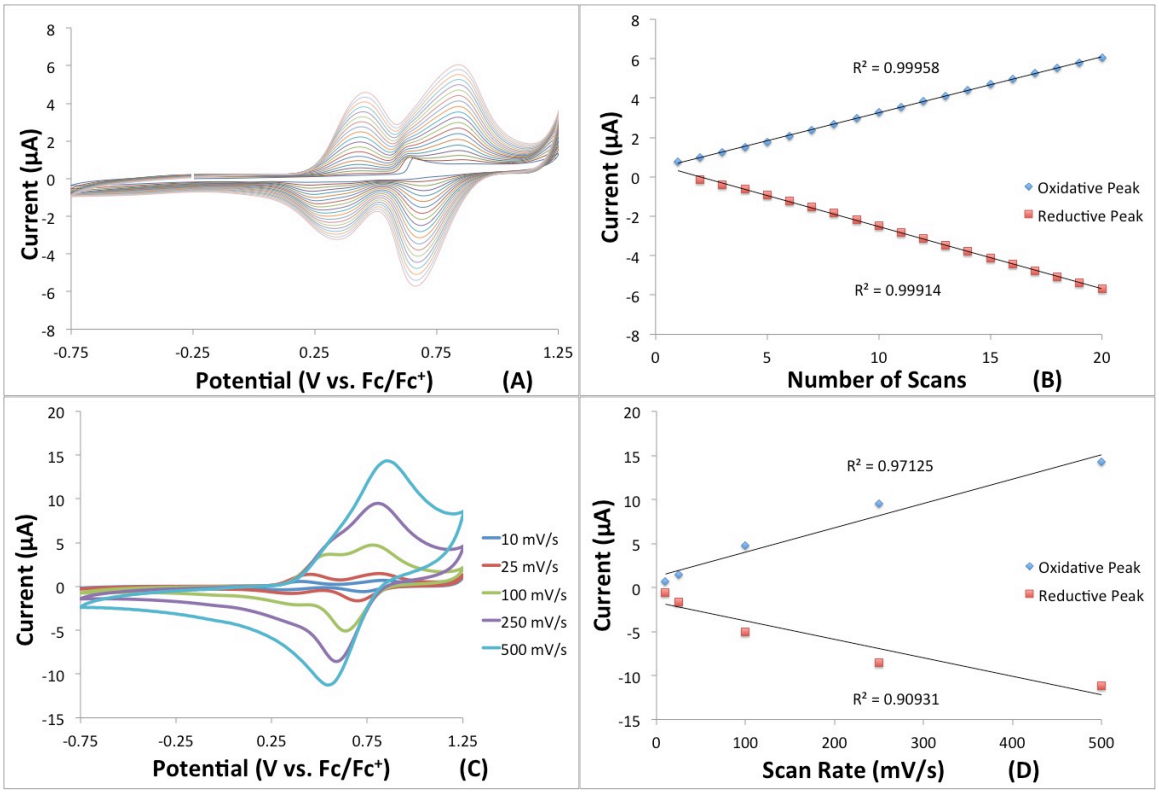

Figure 4.10: Electropolymerization of the ligand on a Pt button working electrode (1.6 mm diameter). The electrolyte was a 0.1 *M* $TBAPF_6$ DCM solution. (A) Film growth. (B) The oxidative and reductive peak currents vs. the number of scans. (C) Scan rate dependency study. (D) The oxidative and reductive peak currents vs. scan rate.

Scheme 4.3 displays the electropolymerization of **L** to form **poly-L** as an electrode-confined film on a platinum button working electrode. As shown in Figures 4.10A and 4.10B, cyclic voltammetry was performed with the potential swept from -0.75 to 1.25 V (vs. Fc/Fc^+). Polymer film growth was evident, beginning with irreversible monomer oxidation at 0.66 V in the first scan. Subsequent scans display reversible oxidation at 0.44 V and 0.84 V and correspond to the electrode-confined polymer. The relationship between current and the number of scans is linear, which is indicative of an electrically conductive polymer, which displays regular growth. A scan rate dependency study and the relationship between current and scan rate are displayed in Figures 4.10C and 4.10D. The current and scan rate are linearly related, which is indicative of the ionic conductivity of the polymer film.

The electropolymerization of **Al L** to **poly-Al L** is displayed in Scheme 4.4. The polymer film growth and the relationship between the current and the number of scans are presented in Figures 4.11A and 4.11B. An irreversible oxidation peak was observed at 0.68 V vs. Fc/Fc^+ and corresponds to the monomer. In subsequent scans, two reversible oxidation scans were evident at 0.45 and 0.72 V vs. Fc/Fc^+ and correspond to the oxidation of the polymer. The observation that the current increases linearly with respect to the number of scans indicates that the polymer is electrically conductive. A scan rate dependency study and a plot of current vs. scan rate are presented in Figures 4.11C and 4.11D, respectively. These data imply that the relationship is linear at low scan rates, but deviates from linearity at higher scan rates. This behavior is indicative of a polymer film that has limited porosity to counter ions because the ion flux is not efficient at high scan rates.

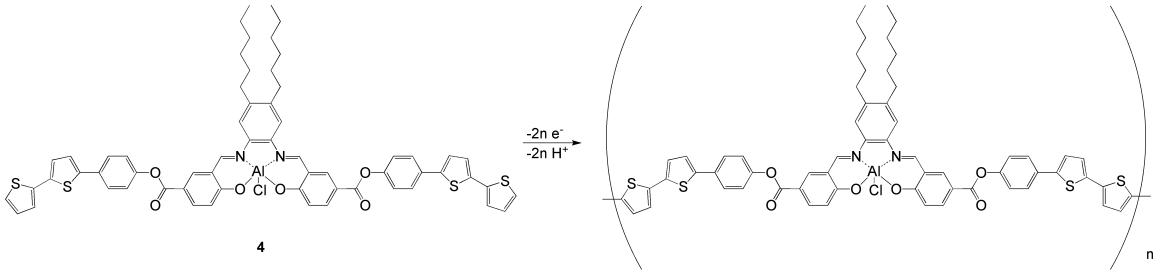

Scheme 4.4: Electropolymerization of the aluminum complex.

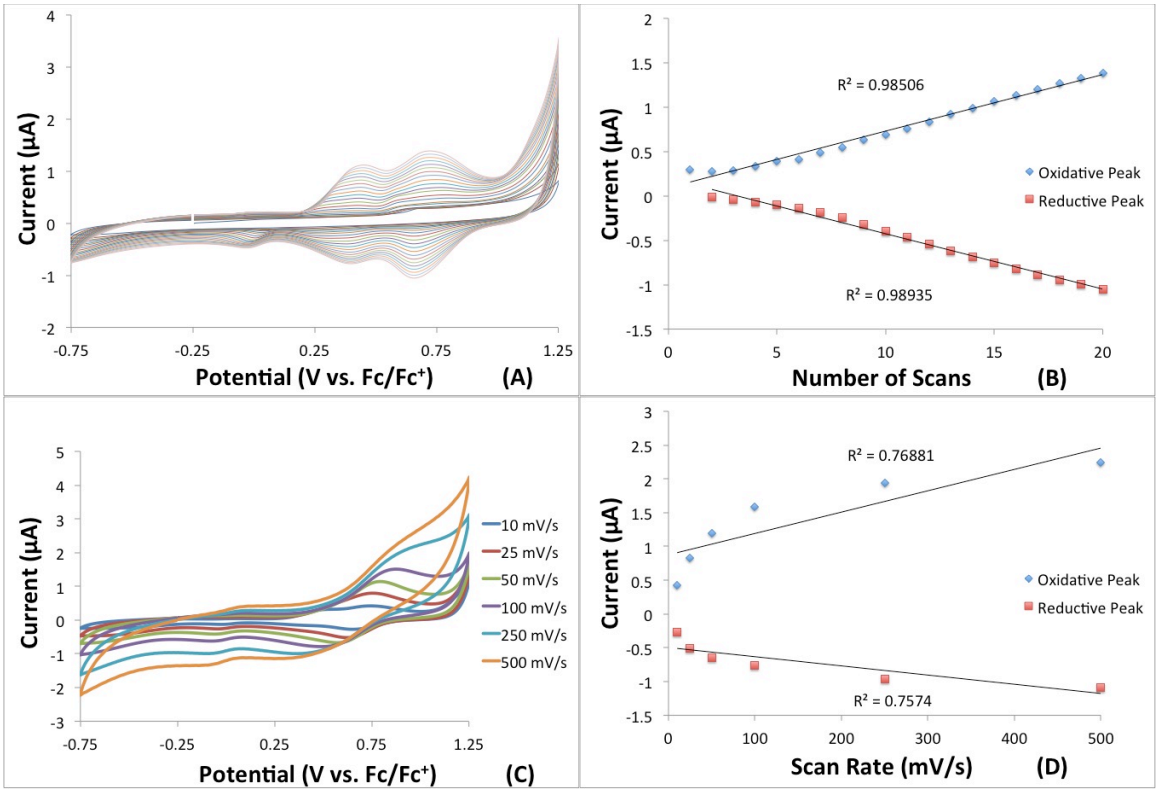

Figure 4.11: Electropolymerization of the aluminum complex on a Pt button working electrode (1.6 mm diameter). The electrolyte was a 0.1 *M* $TBAPF_6$ DCM solution. (A) Film growth. (B) The oxidative and reductive peak currents vs. number of scans. (C) Scan rate dependency study. (D) The oxidative and reductive peak currents vs. scan rate.

Spectroscopic Properties of the Polymer

The absorption spectrum of **poly-Al L** as a film on ITO-coated glass is presented in Figure 4.12 and consists of a significantly broader, red-shifted band in comparison with that of **Al L**. This is completely consistent with the formation of a polymeric structure with significantly delocalized electronic structure. The film on ITO-coated glass was subsequently sonicated in dimethylformamide (DMF) for 15 minutes. The room temperature emission spectrum of a DMF solution of the polymer was excited at 380 nm and is displayed in Figure 4.13. The emission maximum at 505 nm was red-shifted with respect to that of **Al L**. The pertinent data are summarized in Table 4.2.

Table 4.2: UV-vis absorption and photoluminescence data of **poly-Al L**.

	Absorbance λ_{max}, nm	Excitation λ_{max} (nm)	Emission λ_{max} (nm)	τ (μs)
poly-Al L	377	380	505	8.122 ± 0.8653

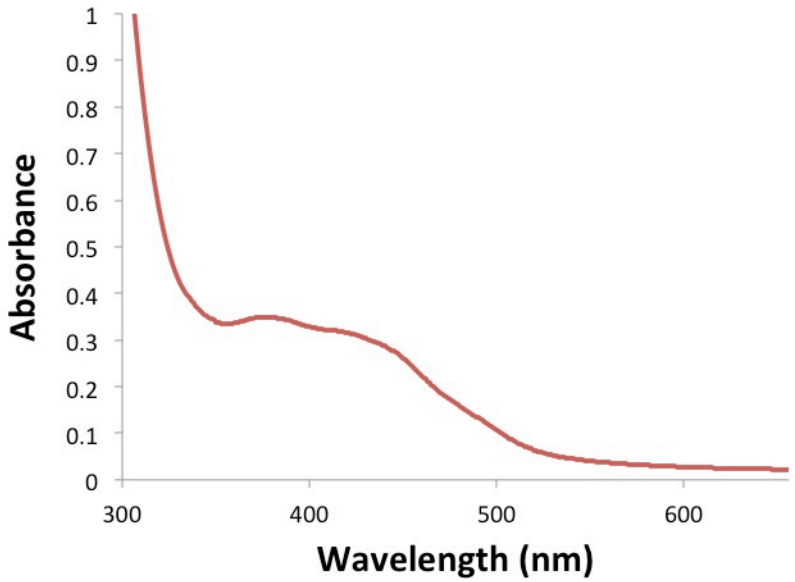

Figure 4.12: UV vis absorption spectrum of a film of **poly-Al L** deposited on ITO-coated glass at room temperature.

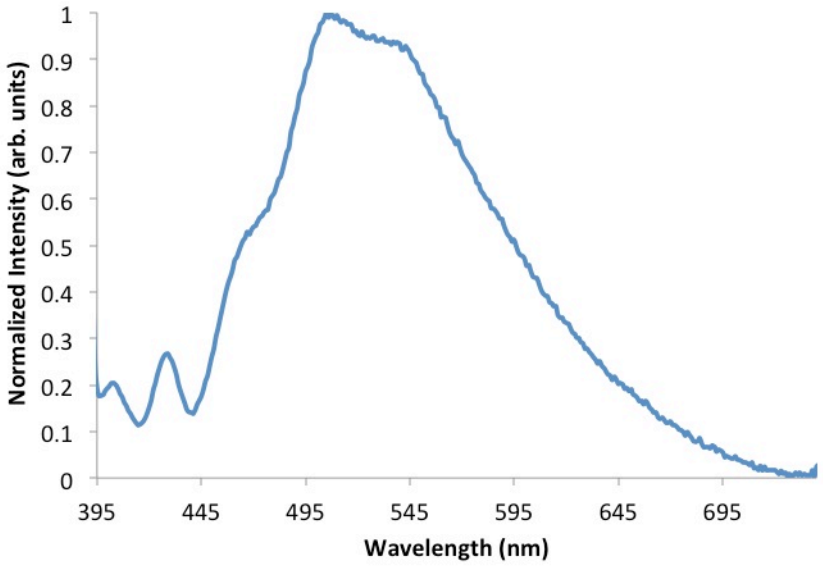

Figure 4.13: Emission spectrum of **poly-Al L** in DMF solution at room temperature.

CONCLUSIONS

The synthesis and characterization of a polymerizable ester-functionalized salophen aluminum complex has been accomplished with the objective of achieving a polymer that exhibits blue emission. The resulting complex in monomeric form was found to emit at 491 nm due to charge transfer, which falls in the blue range. This emission is slightly red-shifted with respect to other non-polymerizable ester-functionalized salophen aluminum complexes previously reported.[77,147] The quantum yield for the new complex is 8.19%, which is significantly larger than that of the ligand (0.532%). Electropolymerization of this monomer resulted in the formation of a polymer that was electrically conductive, as indicated by the linear increase in current with number of scans. However, the new polymer exhibited limited porosity with respect to counter ions, as indicated by the deviation from linearity of the relationship between current and scan rate at higher scan rates. A DMF solution of the new polymer exhibited

emission centered at 505 nm, which is slightly red-shifted with respect to the emission of the monomer.

EXPERIMENTAL DETAILS

General Methods

Air- and moisture-free reactions were performed under a dry, oxygen-free argon atmosphere or in vacuo using standard Schlenk line and dry box techniques. All glassware was dried for at least 24 h in a 120 °C oven prior to use. Toluene was distilled over sodium with a sodium benzophenone ketyl indicator and was degassed before use. DMF was degassed over molecular sieves for 30 minutes prior to use. Deuterated solvents were purchased from Cambridge Isotopes and used as received. 3-formyl-4-hydroxybenzoic acid[147] and 2-(tributylstannyl)bithiophene[161] were prepared according to literature procedures. 1,2-diamino-4,5-dihexylbenzene was prepared using a procedure adapted from literature.[162] All other chemicals were purchased from commercial suppliers and used as received. The NMR spectra were recorded on a Varian 300 Unity Plus spectrometer (300 MHz, 298 K), an Agilent MR (400 MHz, 298 K), a Varian Inova (500 MHz, 298 K), or a Varian DirectDrive 600 (600 MHz, 298 K). Chemical shifts are referenced with respect to the deuterated solvent and all coupling constants are reported in Hz. Mass spectrometric data were acquired using a Thermo Finngan TSQ 700 instrument. All elemental analyses were performed by QTI, Whitehouse, New Jersey. The infrared spectra were recorded using a Nicolet IR 200 FTIR spectrometer.

Instruments

X-ray Crystallography

The data were collected at room temperature on a Rigaku R-Axis Spider diffractometer with an image plate detector using a graphite monochromator with CuKα

radiation (λ = 1.5418Å). A total of 242 images of data were collected using ω-scans with a scan range of 5° and a counting time of 600 seconds per image. Data reduction was performed using the Rigaku Americas Corporation's Crystal Clear version 1.40. The structure was solved by direct methods using SIR97 and refined by full-matrix least-squares on F^2 with anisotropic displacement parameters for the non-H atoms using SHELXL-97. The hydrogen atoms were calculated in ideal positions with isotropic displacement parameters set to 1.2xUeq of the attached atom (1.5xUeq for methyl hydrogen atoms). The terminal thiophene ring was found to be disordered by rotation about the C-C bond connecting the disordered ring with the remainder of the molecule. This disorder was modeled by assigning the variable x to the site occupancy factor for the atoms of one component of the disorder. The variable (1-x) was assigned to the site occupancy factor for the alternate component. A common isotropic displacement parameter was refined for all ten atoms while restraining the geometry of the two rings to be equivalent. The site occupancy for the major component consisting of atoms S2, C19, C20, C21 and C22 refined to 81(2)%. The atoms of the major component were refined anisotropically while restraining their displacement parameters to be approximately isotropic. The atoms of the minor component were refined isotropically. The geometry of the rings was restrained to be equivalent throughout the refinement.

UV-Vis and Luminescent Measurements

Absorption spectra were recorded on a Varian Cary 6000i UV-Vis NIR Spectrophotometer with Starna Quartz Fluorometer Cells with a pathlength of 1 cm. Luminescent measurements were recorded on a Photon Technology International QM 4 spectrophotometer. Quantum yields were determined using an aqueous solution of quinine sulfate in 5 *M* H_2SO_4 according to the following equation:

$$\varphi_{sample} = \varphi_{std}\left(\frac{A_{std}}{A_{sample}}\right)\left(\frac{Int_{sample}}{Int_{std}}\right)\left(\frac{\eta_{sample}}{\eta_{std}}\right)^2$$

In this equation, A is the absorbance at the excitation wavelength, Int is the integral of the emission peaks, and η is the refractive index of the solvents used.

Electrochemistry

All electrochemical studies were performed in a dry-box under a nitrogen atmosphere using a GPES system from Eco. Chemie B.V. All electrochemical experiments were carried out in a three-electrode cell with a 0.01 *M* $Ag/AgNO_3$ reference electrode, a platinum working electrode, and a platinum coil counter electrode. Potentials were measured with respect to the reference electrode. Ferrocene was used as an external reference to calibrate the reference electrode prior to performing experiments and this value was used to correct the measured potentials. All experiments were performed in DCM solutions containing 0.1 *M* [*n*-Bu_4N][PF_6] ($TBAPF_6$) as the supporting electrolyte. The electrolyte was purified by recrystallization from hot ethanol three times and was subsequently dried under reduced pressure at 100-150 °C for 3 d. The polymer films were deposited on Delta Technologies ITO-coated glass for spectroscopic measurements. Electropolymerizations were performed from monomer solutions by continuous cycling between -0.5 and 1.5 V at a scan rate of 100 mV s^{-1}.

Synthesis of the Ligand and Aluminum Complex

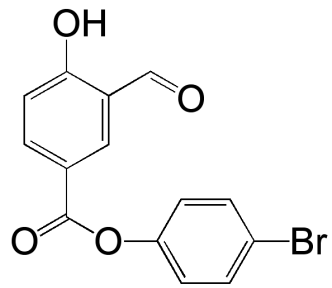

4-bromophenyl ester salcylaldehyde (1)

In a 250 mL round bottom flask, 4-bromophenol (4.5559 g, 26.33 mmol), DCC (6.1200 g, 29.66 mmol), and DMAP (0.3780 g, 3.09 mmol) were added to 3-formyl-4-hydroxybenzoic acid (4.2123 g, 25.36 mmol) dissolved in 150 mL DCM. The cloudy solution was refluxed open to air for 48 h and subsequently cooled to room temperature and filtered through celite to remove the white solid, DCU. The yellow solution was concentrated and the crude material was purified by column chromatography (SiO_2, $CHCl_3$ as eluent) to yield a white solid (4.4600 g, 13.89 mmol, 54.8% yield). ^{1}H NMR (300 MHz, $CDCl_3$) δ: 11.489 (s, 1H), 9.977 (s, 1H), 8.448 (d, J = 2.1, 1H), 8.307 (dd, J = 9.0, J = 2.1, 1H), 7.534 (dt, J = 8.7, J = 3.3, 2H), 7.092 (dt, J = 8.7, J = 3.0, 3H); ^{13}C{^{1}H} NMR (125 MHz, $CDCl_3$) δ: 196, 166, 163, 150, 138, 137, 133, 123, 121, 120, 119, 118. MS (CI): calcd for $C_{14}H_{10}O_4Br$ ($M+H^+$) 320.9762, found 320.9764. m.p.: 140 ºC. Elemental anal.: calcd for $C_{14}H_9O_4Br$, C 52.36, H 2.82, Br 24.88; found C 52.31, H 2.73, Br 25.78.

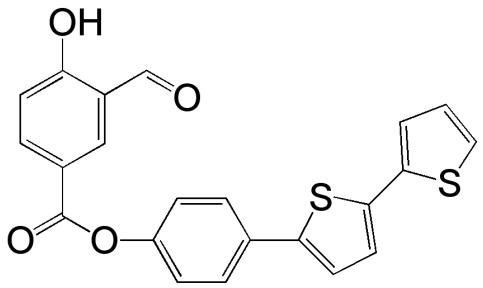

4-(2,2'-bithiophen-5-yl)phenyl ester salcylaldehyde (2)

1 (0.3950 g, 1.23 mmol), 2-(tributylstannyl)bithiophene (0.6214 g, 1.36 mmol), and $Pd(PPh_3)_4$ (0.2839 g, 0.25 mmol) were solubilized in 150 mL dry DMF and were heated to 80 °C for 4 d under argon. DMF was then removed under reduced pressure and the resulting residue was dissolved in DCM and filtered through celite. The DCM solution was washed with a saturated NH_4Cl (aq) solution and water and was dried with Na_2SO_4. The solution was concentrated and the crude product was purified by column chromatography (SiO_2, $CHCl_3$ as eluent) to yield a yellow solid (0.2369 g, 0.58 mmol, 47.4% yield). Further purification was achieved by recrystallization from hot toluene. ^1H NMR (300 MHz, CD_2Cl_2) δ: 11.516 (s, 1H), 10.018 (s, 1H), 8.519 (d, *J* = 2.7, 1H), 8.351 (dd, *J* = 8.7, *J* = 2.1, 1H), 7.686 (dt, *J* = 9.0, *J* = 2.4, 2H), 7.282-7.236 (m, 5H), 7.191 (d, *J* = 3.9, 1H), 7.126 (d, *J* = 9.0, 1H), 7.058 (dd, *J* = 3.6, *J* = 5.1, 1H); $^{13}C\{^1H\}$ NMR (100 MHz, $CDCl_3$) δ: 196, 166, 138, 137, 128, 127, 125, 125, 124, 124, 122, 118. MS (CI): calcd for $C_{22}H_{14}O_4S_2$ (M^+) 406.0334, found 406.0336. m.p.: 177 ºC. Elemental anal.: calcd for $C_{22}H_{14}O_4S_2$, C 65.01, H 3.47, S 15.78; found C 65.07, H 3.21, S 14.76.

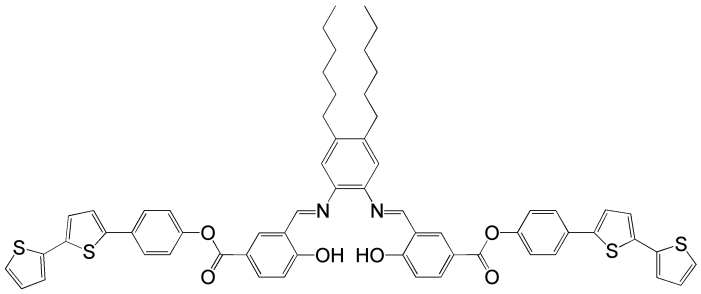

4-(2,2'-bithiophen-5-yl)phenyl ester salo-dihexyl-phen (L)

2 (0.2971 g, 0.73 mmol) was fully dissolved in 33 mL $CHCl_3$ and 23 mL hot methanol was added. 1,2-diamino-4,5-dihexylbenzene (0.0984 g, 0.36 mmol) dissolved in a minimum amount of hot methanol was added dropwise to **2** and the color of the resulting mixture deepened from yellow to golden yellow. The reaction was stirred open to air at 35 °C for 1 h, during which time a precipitate began to form. The reaction was then removed from heat and stirred overnight at room temperature. A yellow solid (0.2975 g, 0.28 mmol, 79.3% yield) was isolated by filtration and was rinsed with methanol. ^{1}H NMR (600 MHz, CD_2Cl_2) δ: 14.066 (s, 2H), 8.801 (s, 2H), 8.363 (d, *J* = 2.2, 2H), 8.216 (dd, *J* = 8.6, *J* = 2.2, 2H), 7.682 (dt, *J* = 8.7, *J* = 2.8, 4H), 7.282-7.258 (m, 8H), 7.243 (dd, *J* = 3.5, *J* = 1.1, 2H), 7.19 (d, *J* = 3.7, 2H), 7.145 (d, *J* = 8.8, 4H), 7.058 (dd, *J* = 5.0, *J* = 3.5, 2H), 2.705 (t, *J* = 8.0, 4H), 1.657 (q, *J* = 7.4, 4H), 1.447, (q, *J* = 7.2, 4H), 1.356 (m, 8H), 0.912 (t, *J* = 9.4, 6H); ^{1}H NMR (300 MHz, $(CD_3)_2SO$) δ: 9.203, 8.603, 8.139, 7.763, 7.529, 7.401-7.340, 7.240-7.116, 2.716, 2.644, 1.608, 1.324, 0.872 (^{1}H NMR $(CD_3)_2SO$ data of **L** collected for comparison with ^{1}H NMR $(CD_3)_2SO$ data of **Al L**; all peaks were featureless and undefined); $^{13}C\{^1H\}$ NMR (150 MHz, CD_2Cl_2) δ: 166, 165, 163, 151, 142, 142, 140, 138, 137, 136, 135, 132, 128, 127, 125, 125, 124, 124, 123, 121, 120, 119, 118, 33, 32, 32, 30, 23, 14. MS (ESI): calcd for $C_{62}H_{56}N_2NaO_6S_4$ ($M+Na^+$) 1075.29134, found 1075.28942. m.p.: 207 ºC. Elemental anal.: calcd for

$C_{62}H_{56}N_2O_6S_4$, C 70.69, H 5.36, N 2.66, S 12.18; found C 70.35, H 5.12, N 2.46, S 13.78. IR: $\nu_{C=O}$ 1724, $\nu_{C=N}$ 1616.

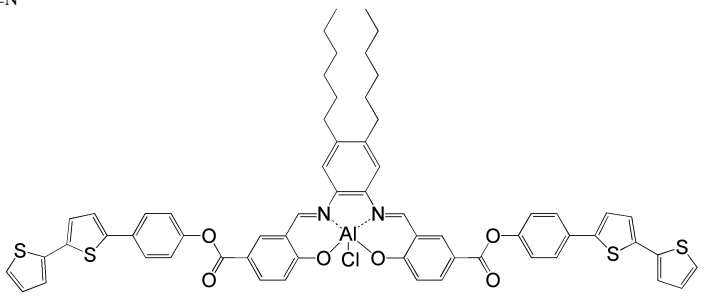

4-(2,2'-bithiophen-5-yl)phenyl ester salo-dihexyl-phen aluminum chloride (Al L)

L (0.0483 g, 0.046 mmol) was fully dissolved in 200 mL dry toluene under argon. Slight heat was necessary to achieve complete dissolution. Dimethylaluminum chloride (0.09 mL, 0.09 mmol) was added and a precipitate formed within minutes. The solution was stirred overnight at 65 °C under argon. The yellow precipitate (0.0458 g, 0.041 mmol, 89.4% yield) was isolated by filtration and was rinsed with hot toluene and pentane. ^{1}H NMR (600 MHz, $(CD_3)_2SO$) δ: 9.543 (s, 2H), 8.672 (d, J = 2.4, 2H), 8.199 (dd, J = 8.7, J = 2.4, 2H), 8.023 (s, 2H), 7.780 (d, J = 8.6, 4H), 7.545 (dd, J = 5.1, J = 1.2, 2H), 7.529 (d, J = 3.7, 2H), 7.373-7.345 (m, 8H), 7.129-7.111 (m, 4H), 2.685 (t, J = 7.9, 4H), 1.635 (q, J = 7.6, 4H), 1.414 (q, J = 7.3, 4H), 1.325 (m, 8H), 0.874 (t, J = 7.0, 6H); ^{13}C{^{1}H} NMR (150 MHz, $(CD_3)_2SO$) δ: 169, 164, 160, 150, 143, 141, 139, 137, 136, 136, 135, 131, 128, 126, 126, 125, 125, 124, 123, 122, 119, 117, 32, 31, 31, 29, 22, 14. MS (ESI): calcd for $C_{124}H_{108}Al_2N_4O_{12}S_8$ (M^{2+}) 1078.26925, found 1078.26987. m.p.: 292 ºC (decomp.). IR: $\nu_{C=O}$ 1727, $\nu_{C=N}$ 1617.

X-RAY CRYSTALLOGRAPHIC DETAILS

Table A4.1: Crystal data and structure refinement for 4-(2,2'-bithiophen-5-yl)phenyl ester salcylaldehyde.

Empirical formula	C22 H14 O4 S2	
Formula weight	406.45	
Temperature	293(2) K	
Wavelength	1.54180 Å	
Crystal system	Orthorhombic	
Space group	Pccn	
Unit cell dimensions	a = 7.353(2) Å	α = 90°.
	b = 82.712(8) Å	β = 90°.
	c = 5.9910(10) Å	γ = 90°.
Volume	3643.6(12) $Å^3$	
Z	8	
Density (calculated)	1.482 Mg/m^3	
Absorption coefficient	2.886 mm^{-1}	
F(000)	1680	
Theta range for data collection	6.59 to 69.99°.	
Index ranges	-6<=h<=8, -100<=k<=100, -7<=l<=7	
Reflections collected	34442	
Independent reflections	3427 [R(int) = 0.1179]	
Completeness to theta = 69.99°	99.0 %	
Absorption correction	Semi-empirical from equivalents	
Max. and min. transmission	1.00 and 0.636	
Refinement method	Full-matrix least-squares on F^2	
Data / restraints / parameters	3427 / 166 / 271	
Goodness-of-fit on F^2	1.200	
Final R indices [I>2sigma(I)]	R1 = 0.0998, wR2 = 0.1970	
R indices (all data)	R1 = 0.2260, wR2 = 0.2746	
Largest diff. peak and hole	0.353 and -0.484 e.$Å^{-3}$	

Table A4.2: Selected bond lengths for 4-(2,2'-bithiophen-5-yl)phenyl ester salcylaldehyde.

C1-O1	1.358(7)	C11-C12	1.403(9)
C1-C2	1.382(10)	C12-C13	1.370(9)
C1-C6	1.407(8)	C12-C15	1.445(8)
C2-C3	1.384(8)	C13-C14	1.381(8)
C2-C7	1.453(9)	C15-C16	1.363(9)
C3-C4	1.382(8)	C15-S1	1.731(7)
C4-C5	1.408(10)	C16-C17	1.417(9)
C4-C8	1.455(9)	C17-C18	1.339(9)
C5-C6	1.356(8)	C18-C19	1.447(9)
C7-O2	1.215(7)	C18-S1	1.734(7)
C8-O3	1.207(8)	C19-C20	1.326(13)
C8-O4	1.351(7)	C19-S2	1.717(11)
C9-C14	1.344(9)	C20-C21	1.460(14)
C9-C10	1.376(9)	C21-C22	1.351(10)
C9-O4	1.390(7)	C22-S2	1.663(10)
C10-C11	1.390(8)		

Table A4.3: Selected bond angles for 4-(2,2'-bithiophen-5-yl)phenyl ester salcylaldehyde.

O1-C1-C2	124.6(6)	C13-C12-C15	122.0(7)
O1-C1-C6	115.3(7)	C11-C12-C15	121.1(8)
C2-C1-C6	120.0(7)	C12-C13-C14	123.0(7)
C1-C2-C3	119.1(6)	C9-C14-C13	119.3(7)
C1-C2-C7	120.3(7)	C16-C15-C12	129.8(7)
C3-C2-C7	120.4(7)	C16-C15-S1	108.8(5)
C4-C3-C2	121.9(7)	C12-C15-S1	121.3(6)
C3-C4-C5	117.8(6)	C15-C16-C17	114.5(7)
C3-C4-C8	121.2(8)	C18-C17-C16	113.5(7)
C5-C4-C8	121.0(6)	C17-C18-C19	130.5(9)
C6-C5-C4	121.2(7)	C17-C18-S1	110.2(5)
C5-C6-C1	119.8(7)	C19-C18-S1	119.1(8)
O2-C7-C2	124.4(8)	C8-O4-C9	121.6(6)
O3-C8-O4	122.3(7)	C15-S1-C18	93.1(4)
O3-C8-C4	124.9(7)	C20-C19-C18	129.3(12)
O4-C8-C4	112.8(7)	C20-C19-S2	109.6(7)
C14-C9-C10	120.5(6)	C18-C19-S2	121.1(9)
C14-C9-O4	119.1(7)	C19-C20-C21	115.3(11)
C10-C9-O4	120.1(7)	C22-C21-C20	107.9(10)
C9-C10-C11	120.3(7)	C21-C22-S2	114.6(9)
C10-C11-C12	120.0(7)	C22-S2-C19	92.6(5)
C13-C12-C11	116.9(6)		

REFERENCES

1. Malik, M. A.; Afzaal, M.; O'Brien, P. *Chem. Rev.* **2010,** *110,* 4417-4446.
2. Hart, G. L. W.; Zunger, A. *Phys. Rev. B: Condens. Matter Mater. Phys.* **2000,** *62,* 13522-13537.
3. Boudjemline, A.; Islam, M. M.; Louial, L.; Diawara, B. *Physica B* **2011,** *406,* 4272-4277.
4. Phillips, J. C. *Bonds and Bands in Semiconductors;* Academic Press: New York, 1973.
5. Van Vechten, J. A.; Phillips, J. C. *Phys. Rev. B: Solid State* **1970,** *2,* 2160-2167.
6. Wentzcovitch, R. M.; Cohen, M. L.; Lam, P. K. *Phys. Rev. B: Condens. Matter Mater. Phys.* **1987,** *36,* 6058-6068.
7. Zaoui, A.; El Haj Hassan, F. *J. Phys.: Condens. Matter* **2001,** *13,* 253-262.
8. Cui, S.; Feng, W.; Hu, H.; Feng, Z.; Wang, Y. *Computational Materials Science* **2009,** *44,* 1386-1389. Wentzcovitch, R. M.; Cohen, M. L. *Journal of Physics C: Solid State Physics* **1986,** *19,* 6791-6797. Merabet, M.; Rached, D.; Khenata, R.; Benalia, S.; Abidri, B.; Bettahar, N.; Bin Omran, S. *Physica B* **2011,** *406,* 3247-3255. Ahmed, R.; Javad Hashemifar, S.; Akbarzadeh, H.; Ahmed, M.; Aleem, F. *Computational Materials Science* **2007,** *39,* 580-586. Surh, M. P.; Louie, S. G.; Cohen, M. L. *Phys. Rev. B: Condens. Matter Mater. Phys.* **1991,** *43,* 9126-9132. Meradji, H.; Drablia, S.; Ghemid, S.; Belkhir, H.; Bouhafs, B.; Tadjer, A. *Phys. Status Solidi B* **2004,** *241,* 2881-2885. Bouhafs, B.; Aourag, H.; Certier, M. *J. Phys.: Condens. Matter* **2000,** *12,* 5655-5668.
9. Kuech, T. F.; Veuhoff, E. *J. Cryst. Growth* **1984,** *68,* 148-156.
10. Bradley, D. C.; Faktor, M. M.; Scott, M.; White, E. A. D. *J. Cryst. Growth* **1986,** *75*, 101-106.
11. Stringfellow, G. B. *J. Cryst. Growth* **1990,** *105,* 260-270.
12. Cowley, A. H.; Jones, R. A. *Polyhedron* **1994,** *13,* 1149-1157.
13. Cowley, A. H.; Jones, R. A. *Angew. Chem., Int. Ed.* **1989,** *28,* 1208-1215.
14. Miller, J. E.; Mardones, M. A.; Nail, J. W.; Cowley, A. H.; Jones, R. A.; Ekerdt, J. G. *Chem. Mater.* **1992,** *4,* 447-452.
15. Cowley, A. H.; Benac, B. L.; Ekerdt, J. G.; Jones, R. A.; Kidd, K. B.; Lee, J. Y.; Miller, J. E. *J. Am. Chem. Soc.* **1988,** *110,* 6248-6249.
16. Coates, G. E.; Graham, J. *J. Chem. Soc.* **1963,** 233- 237.

17. Beachley, O. T.; Coates, G. E. *J. Chem. Soc.* **1965,** 3241-3247.

18. Cowley, A. H.; Jones, R. A.; Mardones, M. A.; Nunn, C. M. *Organometallics* **1991,** *10,* 1635-1637.

19. Cowley, A. H.; Harris, P. R.; Jones, R. A.; Nunn, C. M. *Organometallics* **1991,** *10,* 652-656.

20. Arif, A. M.; Benac, B. L.; Cowley, A. H.; Geerts, R.; Jones, R. A.; Kidd, K. B.; Power, J. M.; Schwab, S.T. *J. Chem. Soc., Chem. Commun.* **1986,** 1543-1545.

21. Cullen, W. R. *Adv. Organomet. Chem.* **1966,** *4,* 145-242.

22. Wells, R. L.; Shafieezad, S.; McPhail, A. T.; Pitt, C. G. *J. Chem. Soc., Chem. Commun.* **1987,** 1823-1824.

23. Miller, J. E.; Kidd, K. B.; Cowley, A. H.; Jones, R. A.; Ekerdt, J. G.; Gysling, H, J.; Wernberg, A. A.; Blanton, T. N. *Chem. Mater.* **1990,** *2,* 589-593.

24. Ekerdt, J. G.; Sun, Y. M.; Jackson, M. S.; Lakhotia, V.; Pacheco, K. A.; Koschmieder, S. U.; Cowley, A. H.; Jones, R. A. *J. Cryst. Growth* **1992,** *124,* 158-164.

25. Lakohtia, V.; Heitzinger, J. M.; Cowley, A. H.; Jones, R. A.; Ekerdt, J. G. *Chem. Mater.* **1994,** *6,* 871-874.

26. Groshens, T. J.; Higa, K. T.; Nissan, R.; Butcher, R. J.; Freyer, A. J. *Organometallics* **1993,** *12,* 2904-2910.

27. Groshens, T. J.; Johnson, C. E. *J. Organomet. Chem.* **1994,** *480,* 11-14.

28. Halaoui, L. I.; Kher, S. S.; Lube, M. S.; Aubuchon, A. R.; Hagan, C. R. S.; Wells, R. L.; Coury, L. A., Jr. *ACS Symp. Ser.* **1996,** *622,* 178-194.

29. Wells, R. L.; Pitt, C. G.; McPhail, A. T.; Purdy, A. P.; Shafieezad, S.; Hallock, R. B. *Chem. Mater.* **1989,** *1,* 4-6.

30. Olshavsky, M. A.; Goldstein, A. N.; Alivisatos, A. P.; *J. Am. Chem. Soc.* **1990,** *112,* 9438-9439.

31. Wells, R. L.; Self, M. F.; McPhail, A. T.; Aubuchon, S. R. *Organometallics* **1993,** *12,* 2832-2834.

32. Aubuchon S. R.; McPhail, A. T.; Wells, R. L. *Chem. Mater.* **1994,** *6,* 82-86.

33. Healy, M. D.; Laibinis, P. E.; Stupik, P. D.; Barron, A. R. *J. Chem. Soc., Chem. Commun.* **1989,** *6,* 359-360.

34. Klug, H. P.; Alexander, L. E. *X-ray Diffraction Procedures;* John Wiley & Sons: New York, 1954; Chapter 9.

35. Wells, R. L.; Hallock, R. B.; McPhail, A. T.; Pitt, C. G.; Johansen, J. D. *Chem. Mater.* **1991,** 381-382.

36. Wells, R. L.; Aubuchon, S. R.; Kher, S. S.; Lube, M. S. *Chem. Mater.* **1995,** *7,* 793-800.

37. Janik, J. F.; Baldwin, R. A.; Wells, R. L. *Organometallics* **1996,** *15,* 5385-5390.

38. Bryne, E. K.; Parkanyi, L.; Theopold, K. H. *Science* **1988,** *241,* 332-334.

39. Douglas, T.; Theopold, K. H. *Inorg. Chem.* **1991,** *30,* 594-596.

40. Cowley, A. H.; Jones, R. A.; Nunn, C. M.; Westmoreland, D. L. *Chem. Mater.* **1990,** *2,* 221-222.

41. Green, M.; O'Brien, P. *Chem. Commun.* **1998,** *22,* 2459-2460.

42. Green, M.; O'Brien, P. *J. Mater. Chem.* **2004,** *14,* 629-636.

43. Malik, M. A.; O'Brien, P.; Helliwell, M. *J. Mater. Chem.* **2005,** *15,* 1463-1467.

44. Malik, M. A.; Afzaal, M.; O'Brien, P.; Bangert, U.; Hamilton, B. *Mater. Sci. Technol.* **2004,** *20,* 959-963.

45. Coates, G. E.; Livingstone, J. G. *J. Chem. Soc.* **1961,** 1000-1008.

46. Goetze, R.; Noeth, H. *Zeitschrift fuer Naturforsching* **1975,** *30B,* 875-882.

47. Mardones, M. A.; Cowley, A. H.; Contreras, L.; Jones, R. A.; Carrano, C. J. *J. Organomet. Chem.* **1993,** *455,* C1-C2.

48. Lube, M. S.; Wells, R. L.; White, P. S. *Main Group Metal Chemistry* **1996,** *19,* 733-741.

49. Lube, M. S.; Jouet, R. J.; Wells, R. L.; White, P. S. *Main Group Chemistry* **1997,** *2,* 89-96.

50. Gu, Y.; Zheng, H.; Guo, F.; Qian, Y.; Yang, Z. *Chem. Lett.* **2002,** ***7,*** 724-725. Gu, Y.; Chen, L.; Qian, Y.; Zhang, W. *Bull. Chem. Soc. Jpn.* **2003,** *76,* 1469-1470. Chen, L.; Gu, Y.; Shi, L.; Ma, J.; Yang, Z.; Qian, Y. *Chem. Lett.* **2003,** *32,* 1188-1189. Feng, X.; Shi, L-Y.; Hang, J-Z.; Zhang, J-P.; Fang, J-H.; Zhong, Q-D. *Mater. Lett.* **2005,** *59,* 865-867.

51. Wells, R. L.; Self, M. F.; Johansen, J. D.; Laske, J. A.; Aubuchon, S. R.; Jones, L. J., III. *Inorganic Syntheses* **1997,** *31,* 150-158.

52. Jutzi, P.; Krato, B.; Hursthouse, M.; Howes, A. J. *Chem. Ber.* **1987,** *120,* 565-574.

53. Carmalt, C. J.; Morrison, D. E.; Parkin, I. P. *Polyhedron* **2000,** *19,* 829-833.

54. Perri, J. A.; La Placa, S.; Post, B. *Acta Crystallogr.* **1958,** *11,* 310.

55. Williams, F. V.; Ruehrwein, R. A. *J. Am. Chem. Soc.* **1960,** *82,* 1330-1332.

56. Osugi, J.; Shimizu, K.; Tanaka, Y. *Proceedings of the Japan Academy* **1966,** *42,* 48-53.

57. Osugi, J.; Shimizu, K.; Tanaka, Y.; Kadono, K. *Review of Physical Chemistry of Japan* **1966,** *36,* 54-57.

58. Ku, S. M. *J. Electrochem. Soc.* **1966,** *113,* 813-816.

59. Armington, A. F. *J. Cryst. Growth* **1967,** *1,* 47-48.

60. Chu, T. L.; Hyslop, A. E. *J. Appl. Phys.* **1972,** *43,* 276-279.

61. Chu, T. L.; Hyslop, A. E. *J. Electrochem. Soc.* **1974,** *121,* 412-415.

62. Wang, S.; Swingle, S. F.; Ye, H.; Fan, F-R. F.; Cowley, A. H.; Bard, A. J. *J. Am. Chem. Soc.* **2012,** *134,* 11056-11059.

63. Moulder, J. F.; Stickle, W. F.; Sobol, P. E.; Bomben, K. *Handbook of X-ray Photoelectron Spectroscopy,* 2nd ed.; Chastain, J., Ed.; Perkin-Elmer Corporation: Eden Prairie, MN, 1992.

64. Naritsuka, S.; Mori, M.; Takeuchi, Y.; Monno, Y.; Maruyama, T. *Phys. Status Solidi C* **2011,** *8,* 291-293.

65. Butler, M. A. *J. Appl. Phys.* **1977,** *48,* 1914-1920.

66. Johnson, E. J. In *Semiconductors and Semimetals;* Willardson, R. K., Beer, A. C., Eds.; Academic Press: New York, 1967; Vol. 3, Chapter 6.

67. Antonietti, M. *Angew. Chem. Int. Ed.* **2013,** *52,* 1086-1087.

68. Kim, W. S.; Lim, J. H.; Lee, B-J.; Oh, Y.; Kwon, Y-S. *Journal of Nonlinear Optical Physics and Materials* **2005,** *14,* 505-512.

69. Tao, S.; Lai, S. L.; Yu, J.; Jiang, Y.; Zhou, Y.; Lee, C-S.; Zhang, X.; Lee, S-T. *J. Phys. Chem. C* **2009,** *113,* 16792-16795.

70. Nayak, P. K.; Agarwal, N.; Ali, F.; Patankar, M. P.; Narasimhan, K. L.; Periasamy, N. *Journal of Chemical Sciences* **2010,** *122,* 847-855.

71. Ashenhurst, J.; Brancaleon, L.; Gao, S.; Liu, W.; Schmider, H.; Wang, S.; Wu, G.; Wu, Q. G. *Organometallics* **1998,** *17,* 5334-5341.

72. Hamada, Y.; *IEEE Trans. on Electron Devices* **1997,** *44,* 1208-1217.

73. Ashenhurst, J. Brancaleon, L.; Hassan, A.; Liu, W.; Schmider, H.; Wang, S.; Wu, Q. *Organometallics* **1998,** *17,* 3186-3195.

74. Cotton, F. A.; Wilkinson, G. *Advanced Inorganic Chemistry,* 5th ed.; John Wiley & Sons: New York, 1988. Greenwood, N. N.; Earnshaw, A. *Chemistry of The Elements;* Pergamon Press: Oxford, 1984.

75. Dutta, S.; Biswas, P. *Polyhedron* **2012,** *40,* 72-80.

76. Wang, S. *Coordination Chemistry Reviews* **2001,** *215,* 79-98.

77. Bereau, V.; Duhayon, C.; Sournia-Saquet, A.; Sutter, J-P. *Inorg. Chem.* **2012,** *51,* 1309-1318.

78. Gao, H-Z.; Su, Z-M.; Qin, C-S.; Mo, R-G.; Kan, Y-H. *Int. J. Quantum Chem.* **2004,** *97,*992-1001.

79. Tang, C. W.; VanSlyke, S. A. *Appl. Phys. Lett.* **1987,** *51,* 913-915.

80. Higginson, K. A.; Thomsen, D. L., III. Yang, B.; Papadimitrakopoulos, F. In *Organic Light-Emitting Devices: A Survey;* Shinar, J., Ed.; Springer-Verlag: New York, 2004; p 71.

81. Brinkmann, M.; Gadret, G.; Muccini, M.; Taliani, C.; Masciocchi, N.; Sironi, A. *J. Am. Chem. Soc.* **2000,** *122,* 5147-5157.

82. Chen, C. H.; Shi, J. *Coordination Chemisty Reviews* **1998,** *171,* 161-174.

83. Ding, H. Z.; Xing, X. S.; Zhu, H. S. *J. Phys. D: Appl. Phys.* **1994,** *27,* 591-595.

84. Liao, S-H.; Shiu, J-R.; Liu, S-W.; Yeh, S-J.; Chen, Y-H.; Chen, C-T.; Chow, T. J.; Wu, C-I. *J. Am. Chem. Soc.* **2009,** *131,* 763-777.

85. Song, Q. L.; Li, F. Y.; Yang, H.; Wu, H. R.; Wang, X. Z.; Zhou, W.; Zhao, J. M.; Ding, X. M.; Huang, C. H.; Hou, X. Y. *Chem. Phys. Lett.* **2005,** *416,* 42-46. Song, Q. L.; Li, C. M.; Wang, M. L.; Sun, X. Y.; Hou, X. Y. *Appl. Phys. Lett.* **2007,** *90,* 071109/1-071109/3. Vivo, P.; Jukola, J.; Ojala, M.; Chekharev, V.; Lemmetyinen, H. *Sol. Energy Mater. Sol. Cells* **2008,** *92,* 1416-1420.

86. Kao, P-C.; Chu, S-Y.; Huang, H-H.; Tseng, Z-L.; Chen, Y-C. *Thin Solid Films* **2009,** *517,* 5301-5304.

87. Curioni, A.; Boero, M.; Andreoni, W. *Chem. Phys. Lett.* **1998,** *294,* 263-271.

88. Sugimoto, M.; Sakaki, S.; Sakanoue, K.; Newton, M. D. *J. Appl. Phys.* **2001,** *90,* 6092-6097. Halls, M. D.; Schlegel, H. B. *Chem. Mater.* **2001,** *13,* 2632-2640. Lin, B. C.; Cheng, C. P.; You, Z-Q.; Hsu, C-P. *J. Am. Chem. Soc.* **2005,** *127,* 66-67. Vogler, A.; Kunkely, H. In *Topics in Current Chemistry;* Yersin, H., Ed.; Springer-Verlag: Berlin, 2001; Vol. 213.

89. Perez-Bolivar, C.; Montes, V. A.; Anzenbacher, P., Jr. *Inorg. Chem.* **2006,** *45,* 9610-9612.

90. Albright, T. A.; Burdett, J. K.; Whangbo, M-H. *Orbital Interactions in Chemistry;* Wiley: New York, 1985. Coulson, C. A.; Streitwieser, A., Jr. *Dictionary of pi-Electron Calculations;* Freeman: San Francisco, 1965.

91. Burrows, P. E.; Shen, Z.; Bulovic, V.; McCarty, D. M.; Forrest, S. R.; Cronin, J. A.; Thompson, M. E. *J. Appl. Phys.* **1996,** *79,* 7991-8006.

92. Matsumura, M.; Akai, T. *Jpn. J. Appl. Phys., Part 1* **1996,** *35,* 5357-5360.

93. Kelly, S. M. In *Flat Panel Displays: Advanced Organic Materials,* Connor, J. A., Ed.; The Royal Society of Chemistry: Cambridge, 2000. VanSlyke, S. A. U. S. Patent 5,151,629, 1992. Sapochak, L. S.; Burrows, P. E.; Garbuzov, D.; Ho, D. M.; Forrest, S. R.; Thompson, M. E. *J. Phys. Chem.* **1996,** *100,* 17766-17771.

94. Bryan, P. S.; Lovecchio, F. V.; VanSlyke, S. A. U. S. Patent 5,141,671, 1992.

95. Montes, V. A.; Pohl, R.; Shinar, J. Anzenbacher, P., Jr. *Chem.- Eur. J.* **2006,** *12,* 4523-4535.

96. Chen, Z.; Yu, J.; Sone, M.; Miyata, S.; Lu, Y.; Watanabe, T. *Journal of Physics D: Applied Physics* **2001,** *34,* 2679-2682.

97. Omar, W. A. E.; Haverinen, H.; Hormi, O. E. O. *Tetrahedron* **2009,** *65,* 9707-9712.

98. Pohl, R.; Montes, V. A.; Shinar, J.; Anzenbacher, P., Jr. *J. Org. Chem.,* **2004,** *69,* 1723-1725.

99. Hopkins, T. A.; Meerholz, K.; Shaheen, S,; Anderson, M. L.; Schmidt, A.; Kippelen, B.; Padias, A. B.; Hall, H. K., Jr.; Peyghambarian, N.; Armstrong, N. R. *Chem. Mater.* **1996,** *8,* 344-351.

100. Song, S. Y.; Jang, M. S.; Sim, H. K.; Hwang, D. H.; Zyung, T. *Macromolecules* **1999,** *32,* 1482-1487. Jin, S. H.; Park, H. J.; Kim, J. Y.; Lee, K.; Lee, S. P.; Moon, D. K.; Lee, H. J.; Gal, Y. S. *Macromolecules* **2002,** *35,* 7532-7534. Jin, S. H.; Kang, S. Y.; Kim, M. Y.; Yoon, U. C.; Kim, J. Y.; Lee, K. H.; Gal, Y. S. *Macromolecules* **2003,** *36,* 3841-3847.

101. Feng, L.; Wang, X.; Chen, Z. *Spectrochim. Acta, Part A.* **2008,** *71A,* 312-316.

102. Shi, Y-W.; Shi, M-M.; Huang, J. C.; Chen, H-Z.; Wang, M.; Liu, X. D.; Ma, Y. G.; Xu, H.; Yang, B. *Chem. Commun.* **2006,** *18,* 1941-1943.

103. Shi, M-M.; Lin, J-J.; Shi, Y-W.; Ouyang, M.; Wang, M.; Chen, H-Z. *Mater. Chem. Phys.* **2009,** *115,* 841-845.

104. Irfan, A.; Zhang, J. *Theoretical Chemistry Accounts* **2009,** *124,* 339-344.

105. Heiskanen, J. P.; Tolkki, A. E.; Lemmetyinen, H. J.; Hormi, O. E. O. *J. Mater. Chem.* **2011,** *21, I 14766-14775.*

106. *Molecular Fluorescence- Principles and Applications,* 1st ed.; Valeur, B., Ed.; Wiley-VCH: Weinhein, 2002; pp 46-67.

107. Misra, A.; Kumar, P.; Dhawan, S. K.; Kamalasanan, M. N.; Chandra, S. *Indian Journal of Pure and Applied Physics* **2005,** *43,* 522-526.

108. Ravi Kishore, V. V. N.; Narasimhan, K. L.; Periasamy, N. *Phys. Chem. Chem. Phys.* **2003,** *5,* 1386-1391.

109. Heiskanen, J. P.; Hormi, O. E. O. *Tetrahedron* **2009,** *65,* 8244-8249.

110. Kido, J.; Iizumi, Y. *Chem. Lett.* **1997,** *10,* 963-964. Kido, J.; Iizumi, Y. *Appl. Phys. Lett.* **1998,** *73,* 2721-2723. Mattoussi, H.; Murata, H.; Merritt, C. D.; Iizumi, Y.; Kido, J. *J. Appl. Phys.* **1999,** *86,* 2642-2650. Sapochak, L. S.; Padmaperuma, A.; Washton, N.; Endrino, F.; Schmett, G. T.; Marshall, J.; Fogarty, D.; Burrows, P. E.; Forrest, S. R. *J. Am. Chem. Soc.* **2001,** *123,* 6300-6307.

111. Chai, S. Y.; Zhou, R.; An, Z. W.; Kimura, A.; Fukuno, K.; Matsumura, M. *Thin Solid Films* **2005,** *479,* 282-287.

112. Jang, H.; Do, L-M.; Kim, Y.; Zyung, T.; Do, Y. *Synth. Met.* **2001,** *121,* 1667-1668. Sato, Y.; Ogata, T.; Ichinosawa, S.; Murata, Y. *Synth. Met.* **1997,** *91,* 103-107.

113. Qiu, Y.; Shao, Y.; Zhang, D.; Hong, X. *Jpn. J. Appl. Phys., Part 1* **2000,** *39,* 1151-1153.

114. La Deda, M.; Aiello, I.; Grisolia, A.; Ghedini, M.; Amati, M.; Lelj, F. *Dalton Trans.* **2006,** 330-339.

115. Ma, D.; Wang, G.; Hu, Y.; Zhang, T.; Wang, L.; Jing, X.; Wang, F. Lee, C. S.; Lee, S. T. *Appl. Phys. Lett.* **2003,** *82,* 1296-1298.

116. Chai, S. Y.; Zhou, R.; An, Z. W.; Kimura, A.; Fukuno, K.; Matsumura, M. *Thin Solid Films* **2005,** *479,* 282-287.

117. Lim, J. T.; Jeong, C. H.; Lee, J. H.; Yeom, G. Y.; Jeong, H. K.; Chai, S. Y.; Lee, I. M.; Lee, W. I. *J. Organomet. Chem.* **2006,** *691,* 2701-2707.

118. Mi, B. X.; Gao, Z. Q.; Lee, C. S.; Lee, S. T.; Kwong, H. L.; Wong, N. B. *Appl. Phys. Lett.* **1999,** *75,* 4055-4057.

119. Dawson, W. R.; Windsor, M. W. *J. Phys. Chem.* **1968,** *72,* 3251-3260.

120. Chen, C. H.; Shi, J.; Tang, C. W. *Macromol. Symp.* **1997,** *125,* 1-48

121. Kalman, B.; Clarke, N.; Johansson, L. B-A. *J. Phys. Chem.* **1989,** *93,* 4608-4615.

122. Minsky, A.; Meyer, Y.; Rabnivitz, M. *J. Am. Chem. Soc.* **1982,** *104,* 2475-2482.

123. Tong, C. C.; Hwang, K. C. *J. Phys. Chem. C* **2007,** *111,* 3490-3494.

124. Legnani, C.; Reyes, R.; Cremona, M.; Bagatin, I. A.; Toma, H. E. *Appl. Phys. Lett.* **2004,** *85,* 10-12.

125. Yu, J.; Chen, Z.; Miyata, S. *Chemical Vapor Deposition* **2001,** *7,* 66-68. Kim, S. H.; Cui, J. Z.; Park, J. Y. *Dyes Pigm.* **2002,** *55,* 91-97. Xie, J. Fan, L.; Su, J.;

Tian, H. *Dyes Pigm.* **2003,** *59,* 153-162. Zhong, C.; Guo, R.; Wu, Q.; Zhang, H. *Reactive and Functional Polymers* **2007,** *67,* 408-415.

126. Huang, H.; Zhong, X.; Zhou, Y. *Eur. Polym. J.* **2008,** *44,* 2944-2950.

127. Meyers, A.; Weck, M. *Macromolecules* **2003,** *36,* 1766-1768.

128. Meyers, A.; Weck, M. *Macromolecules* **2004,** *16,* 1183-1188.

129. Amati, M. Lelj, F. *Chem. Phys. Lett.* **2002,** *358,* 144-150.

130. Coelle, M.; Dinnebier, R. E.; Bruetting, W. *Chem. Commun.* **2002,** *23,* 2908-2909.

131. Masuda, H.; Satoh, M. *Jpn. J. Appl. Phys., Part 2* **1996,** *35,* 126-129. Hornyak, G. L.; Patrissi, C. J.; Martin, C. R. *J. Phys. Chem. B* **1997,** *101,* 1548-1555. Hulteen, J. C.; Patrissi, C. J.; Miner, D. L.; Crosthwait, E. R.; Oberhauser, E. B.; Martin, C. R. *J. Phys. Chem. B* **1997,** *101,* 7727-7731. Masuda, H. Fukuda, K. *Science* **1995,** *268,* 1466-1468. Routkevitch, D.; Bigioni, T.; Moskovits, M. Xu, J. M. *J. Phys. Chem.* **1996,** *100,* 14037-14047.

132. Xu, C.; Xue, Q.; Zhong, Y.; Cui, Y.; Ba, L.; Zhao, B.; Gu, N. *Nanotechnology* **2002,** *13,* 47-50.

133. Huang, G. S.; Wu, X. L.; Xie, Y.; Kong, F.; Zhang, Z. Y.; Siu, G. G.; Chu, P. K. *Appl. Phys. Lett.* **2005,** *87,* 151910/1-151910/3.

134. Förster, T. In *Modern Quantum Chemistry, Part 2;* Sinanoglu, O., Ed.; McGraw-Hill: New York, 1965.

135. Levichkova, M. M.; Assa, J. J.; Frob, H.; Leo, K. *Appl. Phys. Lett.* **2006,** *88,* 201912/1-201912/3.

136. Braun, M.; Gmeiner, J.; Tzolov, M.; Coelle, M.; Meyer, F. D.; Milius, W.; Hillebrecht, H.; Wendland, O.; von Schütz, J. U.; Brütting, W. *J. Chem. Phys.* **2001,** *114,* 9625-9632.

137. Zhang, X.; Shi, S.; Liu, Q.; Zhou, J.; Ye, J.; Yu, C. *Chem. Commun.* **2011,** *47,* 6359-6361.

138. Li, S.; Lu, J.; Min, W.; Evans, D. G.; Duan, X. *Advanced Functional Materials* **2010,** *20,* 2848-2856.

139. Wang, Z-L.; Kang, Z-H.; Wang, E-B.; Su, Z-M.; Xu, L. *Inorg. Chem.* **2006,** *45,* 4364-4371. Yan, D.; Lu, J.; Wei, M.; Evans, D. G.; Duan, X. *J. Phys. Chem. B* **2009,** *113,* 1381-1388. Shi, W.; Wei, M.; Lu, J.; Evans, D. G.; Duan, X. *J. Phys. Chem.* **2009,** *113,* 12888-12896.

140. Cozzi, P. G. *Chemical Society Reviews* **2004,** *33,* 410-421.

141. Morisige, K. *Anal. Chim. Acta* **1974,** *72,* 295-305. Morisige, K. *J. Inorganic and Nuclear Chemistry* **1978,** *40,* 843-851. Morisige, K. *Anal. Chim. Acta* **1980,** *121,* 301-308.

142. Cozzi, P. G.; Dolci, L. S.; Garelli, A.; Montalti, M.; Prodi, L.; Zacheroni, N. *New J. Chem.* **2003,** *27,* 692-697.

143. Hwang, K. Y.; Kim, H.; Lee, Y. S.; Lee, M. H.; Do, Y. *Chem.-Eur. J.* **2009,** *15,* 6478-6487.

144. Briggs, M. S. J.; Fossey, J. S.; Richards, C. J.; Scott, B.; Whateley, J. *Tetrahedron Lett.* **2002,** *43,* 5169-5171. Kashanian, S.; Gholivand, M. B.; Ahmadi, F.; Taravati, A.; Hosseinzadeh C. A. *Spectrochim. Acta, Part A* **2007,** *67,* 472-478.

145. Gündüz, S. B.; Küçükkolbasy, S.; Atakol, O.; Kylyç, E. *Spectrochim. Acta, Part A* **2005,** *61,* 913-921.

146. Huh, J. O.; Lee, M. H.; Jang, H.; Hwang, K. Y.; Lee, J. S.; Kim, S. H.; Do, Y. *Inorg. Chem.* **2008,** *47,* 6566-6568. Hwang, K. Y.; Lee, M. H.; Jang, H.; Sung, Y.; Lee, J. S.; Kim, S. H.; Do, Y. *Dalton Trans.* **2008,** 1818-1820.

147. Bereau, V.; Jubera, V.; Arnaud, P.; Kaiba, A.; Guionneau, P.; Sutter, J-P. *Dalton Trans.* **2010,** *39,* 2070-2077.

148. *Fluorescence and Phosphorescence;* Rendell, D., Ed.; John Wiley and Sons: New York, 1987. *Photochemistry and Photophysics of Coordination Compounds;* Yersin H.; Vogler, A., Eds.; Springer-Verlag: Berlin, 1987. *Concepts of Inorganic Photochemistry;* Adamson, A. W.; Fleischauer, P. D., Eds.; John Wiley and Sons: New York, 1975.

149. Ashenhurst, J.; Wu, G.; Wang, S. *J. Am. Chem. Soc.* **2000,** *122,* 2541-2547.

150. Gao, S.; Wu, Q.; Wu, G.; Wang, S. *Organometallics* **1998,** *17,* 4666-4674.

151. Song, D.; Liu, S-F.; Wang, R-Y.; Wang, S. *J. Organomet. Chem.* **2001** *631,* 175-180.

152. Arduini, M.; Felluga, F.; Mancin, F.; Rossi, P.; Tecilla, P.; Tonellato, U.; Valentinuzzi, N. *Chem. Commun.* **2003,** *13,* 1606-1607. Alves, S.; Pina, F.; Albelda, M. T.; García-España, E.; Soriano, C.; Luis S. V. *Eur. J. Inorg. Chem.* **2001,** *2,* 405-412.

153. Berg, J. M. *Accounts of Chemical Research* **1995,** *28.* 14-19.

154. Curtain, C. C.; Ali, F.; Volitakis, I.; Cherny, R. A.; Norton, R. S.; Beyreuther, K.; Barrow, C. J.; Masters, C. L.; Bush, A. I.; Barnham, K. J. *J. Biol. Chem.* **2001,** *276,* 20466-20473. Suh, S. W.; Jensen, K. B.; Jensen, M. S.; Silva, D. S.; Kesslak, P. J.; Sanscher, G.; Fredrickson, C. J. *Brain Res.* **2000,** *852,* 274-278.

155. Rurack, K. *Spectrochim. Acta, Part A* **2001,** *57,* 2161-2195.

156. Aziz, H.; Popovic, Z. D.; Hu, N. X.; Hor, A. M.; Xu, G. *Science* **1999,** *283,* 1900-1902.

157. Khalifa, M. B.; Vaufrey, D.; Tardy, J. *Organic Electronics* **2004,** *5,* 187-198.

158. Tokito, S.; Noda, K.; Tanaka, H.; Taga, Y.; Tsutsui, T. *Synth. Met.* ***2000,*** *111-112,* 393-396.

159. Forrest, S. R. *Nature* **2004,** *428,* 911-918.

160. Holliday, B. J.; Swager, T. M. *Chem. Commun.* **2005,** *1,* 23-36.

161. Gómez-Romero, P.; Sanchez, C. In *Functional Hybrid Materials;* Wiley-VCH: Weinheim, 2004.

162. Zhang, F.; Bai, S.; Yap, G. P. A.; Tarwade, V.; Fox, J. M. *J. Am. Chem. Soc.* **2005,** *127,* 10590-10599.